THESIS FOR THE DEGREE OF LICENTIATE IN ENGINEERING

Computational Techniques for Jet Noise Predictions

MATTIAS BILLSON

Department of Thermo and Fluid Dynamics

CHALMERS UNIVERSITY OF TECHNOLOGY

Göteborg, Sweden, 2002

Computational Techniques for Jet Noise Predictions
MATTIAS BILLSON

© MATTIAS BILLSON, 2002

ISSN 1101-9972
ISRN CTH-TFD-PB-02/02

Institutionen för termo- och fluiddynamik
Chalmers tekniska högskola
SE-412 96 Göteborg, Sweden
Phone +46-(0)31-7721400
Fax: +46-(0)31-180976

Printed at Chalmers Reproservice
Göteborg, Sweden 2002

Computational Techniques for Jet Noise Predictions

by

Mattias Billson

Department of Thermo and Fluid Dynamics
Chalmers University of Technology
SE-412 96 Göteborg, Sweden

Abstract

Larger aircraft with new high performance engines in combination with cities growing closer to urban airports increase noise pollution in inhabited areas. This results in higher fees for landing for large aircrafts and stronger legislations to decrease the emitted sound at take-off and landing. At take-off, the strongest sources of sound on an aircraft are the jets delivering the thrust.

The object of the present work is to develop a method for jet noise predictions and to increase the understanding of sound generation and emission.

The linearized Euler equations on conservative form are used as wave operator and new source terms are derived from the full Euler equations. The source terms have been validated using a direct numerical simulation of a forced 2D mixing layer.

In the jet noise modeling, sources based on stochastic Fourier modes provide the generation of sound and the linearized Euler equations govern the propagation.

Numerical issues in solving the linearized Euler equations are addressed. These include numerical accuracy and stability analysis of higher order numerical schemes.

An initial three-dimensional jet noise prediction has been performed with the present method. The results are not yet in agreement with reference data but further investigations will hopefully give new insight in the reasons for the discrepancies.

Keywords: jet noise, aeroacoustics, SNGR, source terms, linearized euler, CAA, stability, artificial dissipation, absorbing boundary conditions

Preface

Chapter 8 corresponds to the AIAA paper:

- M. Billson, L.-E. Eriksson and L. Davidson, ”Acoustic Source Terms for the Linear Euler Equations on Conservative Form.”, The 8th AIAA/CEAS Aeroacoustics Conference, AIAA 2002-2582 Breckenridge, Colorado, 2002.

Acknowledgments

This work was carried out at the Department of Thermo- and Fluid Dynamics at Chalmers University of Technology. The project was funded by NFFP (the National Flight Research Program). It is part of a cooperative project between Chalmers University of Technology, the Royal Institute of Technology, Volvo Aero Corporation and A2 Acoustics.

I would like to thank Prof. Lars-Erik Eriksson for being a constant source of new ideas and for explaining things so that even I understand. It is inspiring to work with you.

Many thanks also to Prof. Lars Davidson for all the discussions that have resulted in new insights. I have very much appreciated the encouraging and needed talks at times when I was less brave.

Contents

Abstract iii

Preface iv

Acknowledgments vi

1 Introduction 1

2 Stochastic Noise Generation and Radiation Method 5
- 2.1 Overview 5
- 2.2 RANS for Jet Computations 6
- 2.3 Linearized Euler Equations with Source Terms 6
- 2.4 Stochastic Modeling 7
- 2.5 Correlations of Generated Turbulence 13
- 2.6 Source Region 13

3 Linearized Euler Equation Solver 15
- 3.1 Finite Volume Method 15
- 3.2 Convective Fluxes and Artificial Dissipation 17
- 3.3 Time Marching 18

4 Absorbing Boundary Conditions 21
- 4.1 Characteristic Variable Based Absorbing Boundary Conditions (Cvba) 22
- 4.2 Modified Characteristic Variable Based Absorbing Boundary Conditions (Cvba) 23
- 4.3 Boundary Conditions Based on Asymptotic Analysis of The Euler Equations 24
- 4.4 Buffer Layer 26
- 4.5 Test of Absorbing Boundary Conditions 27

5 Kirchhoff-Helmholtz Method **35**

6 Modified Linearized Euler Equations **39**

7 Acoustic Scattering of Cylinder - Benchmark Test Case **43**
7.1 Introduction 43
7.2 Problem Description 43
7.3 Analytical Solution 45
7.4 Numerical Method 46
7.5 Numerical Issues 47
7.6 Boundary Conditions 47
7.7 Computational grid 48
7.8 Results 50

8 Acoustic Source Terms for The Linear Euler Equations on Conservative Form **59**
8.1 Introduction 59
8.2 Theory 60
8.3 Approximations of Source Terms 65
8.4 Numerical Simulation and Validation of Theory 67
8.4.1 Numerical Scheme 67
8.4.2 Boundary Conditions 67
8.4.3 Forcing 70
8.4.4 Computational Setup 71
8.4.5 Direct Simulation 71
8.4.6 Linear Euler Simulation 72
8.5 Acoustic Solution 72
8.6 Results 73
8.7 Conclusions 75

9 3D Jet case - Stromberg Jet **79**
9.1 Jet Characteristics 80
9.2 Comparison of RANS to DNS and Experiments 80
9.3 SNGR Generation 83
9.4 Linearized Euler Computation 83
9.5 Near-Field Data 85
9.6 Far-field Data 86

10 Conclusions **89**

11 Appendix **91**
11.1 The Linearized Euler Equations 91

11.2 Stability Analysis of Hyperbolic Equations 93
11.2.1 Semi-Discretization 94
11.2.2 Artificial Numerical Dissipation 98
11.2.3 Full Discretization 100
11.2.4 Introducing Source Terms 102
11.3 Transformation of Solution to Characteristic Variables . 105
11.4 Numerical Coefficients for
FVM vs FDM 106
11.5 Definitions of Correlations 109
11.6 Time Filtering 109

Bibliography **111**

Chapter 1

Introduction

The research area of aeroacoustics started in the era of the first jet aircraft engines. It was realized that with the new types of engines, the jet engines, there was a potential noise hazard. The first turbo-jet engines were produced for military airplanes. In that application the noise was not really of such a large concern. The main goal was to deliver thrust and the jet engines did that better than any other engine. When jet engines were to be used for civil aircraft however the noise issue became an important factor. With improved technology giving larger and more powerful power plants for commercial aircraft the noise levels increased rapidly. The noise emitted at takeoff from a commercial aircraft in the 60's was more than the combined shouting power of the earths population.

The first research in the area of jet noise began in the late forties and it was in 1952 that the real breakthrough came, when Sir James Lighthill published the first of his two-part paper on aerodynamic sound. The second followed in 1954 [1, 2]. The approach of Lighthill was to try to find the sources of sound in turbulent flow. This was achieved by an acoustic analogy. The basic idea was to rewrite the compressible equations for fluid motion in such a way that the left-hand side consisted of the second-order wave equation governing sound propagation. All other terms were moved to the right-hand side and considered as sources. The resulting wave equation with source term is

$$\frac{\partial^2 \rho}{\partial t^2} + c_0^2 \frac{\partial^2 \rho}{\partial x_j \partial x_j} = \frac{\partial^2 T_{ij}}{\partial x_i \partial x_j} \tag{1.1}$$

where ρ is the density, c_0 is the ambient speed of sound and $T_{ij} = \rho v_i v_j + (p - \rho c_0^2)\delta_{ij} - \tau_{ij}$ is the Lighthill stress tensor containing all non-

linearities, v_i, p, τ_{ij} and δ_{ij} are the velocity, pressure, viscous stress tensor and Kronecker delta. The right-hand side in equation 1.1 involves second spatial derivatives and is identified as a quadrupole.

One of the major assumptions in the acoustic analogy is that acoustic propagation is assumed to take place in an infinite homogeneous medium at rest. This means that there can be no solid bodies present and that refraction of sound due to shear is not taken into account. Since the medium is assumed to be at rest the sound is assumed to propagate uniformly in all directions.

Lighthill managed to find a formal integral solution to the wave equation 1.1 using a Green's function. The most important result from this theory was that the emitted sound power varied as the eighth power of the jet exit velocity. This result was obtained through dimensional analysis.

Extensions of Lighthill's acoustic analogy to incorporate the effect of solid surfaces in the flow was published by Curle [3] in 1955 and later also by Ffowcs Williams and Hawkins [4] among others. The interaction of the turbulence with the surfaces introduces sources which have a dipole character.

The sound radiated from quadrupoles was observed to be amplified in the flow direction. This effect is small for low speeds but large for high speed. In the case of a subsonic jet at high Mach number or a supersonic jet the effect is an important factor of the sound field surrounding the jet. In 1963 Ffowcs Williams [5] published an extended theory including the effect of convection on the directivity of the radiated sound. The theory predicts that there is an amplification of the emitted sound from the convected quadrupoles in a jet in the axial direction.

Another important effect of the convection is the refraction of the generated sound. When the sound is propagating out of the jet to the far-field the local speed of a wavefront will be a function of both the thermodynamic speed of sound and the local convection velocity. The wavefront will tend to bend out from the jet as shown in figure 1.1. The local speed of the wave at location B is higher than that in A. This makes the sound refract out from the jet and cause a cone of silence in the axial direction. This effect will be amplified if the jet is heated compared to the surrounding. To include the effect of refraction in an acoustic analogy Lilley [6] developed an analogy in which the refractional effects were included.

The general understanding of turbulence at that time was that it consisted of small eddies which were more or less randomly distribu-

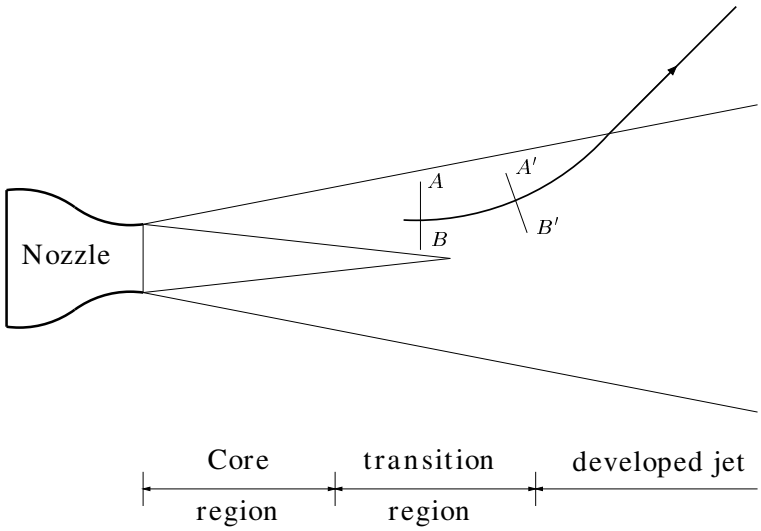

Figure 1.1: Refraction of sound wave.

ted. The source of noise in turbulence was of course believed to be the same eddies. At the beginning of the seventies the discovery of large turbulence structures in jets and free shear flows changed the focus in the aeroacoustic community. The large turbulence structures dominate the overall dynamics and mixing of free shear flows and it was shown that they are a strong source of sound in supersonic jets [7]. However, these large structures are not as important in subsonic jets. For further reading on the importance of large turbulence structures, see Tam [8].

If a supersonic jet is imperfectly expanded shock cells will form close to the jet exit. There are two additional sources of sound in jets that can be identified in the presence of shock cells. These are screech tones and broadband shock associated noise. Since these sources are associated with supersonic jets they are not within the focus of this work.

Until the nineties, all estimation of jet noise was restricted to analogies with solutions based on dimensional arguments and statistical information. Rapid increase in the available computer power opened for the possibility to directly solve the compressible Navier-Stokes equations using Direct Numerical Simulations (DNS) or Large Eddy Simulations (LES). Well performed DNS and LES simulations are very valuable tools for understanding of jet noise generation and propagation. They capture flow-acoustic interaction, refraction, diffraction, presence of solid objects, convectional and other effects which may affect the flow and sound field. It is not feasible yet though, to use these methods in

industrial applications, even if LES might be used in a near future given that the computer development continues as it has in recent years.

But until then it is worth while to continue to develop methods for jet noise estimations which are less computationally intensive. A novel method called SNGR or Stochastic Noise Generation and Radiation method has been developed by Bechara *et al.* [9] and Bailly and Juvé [10]. This method is chosen for the present work and will be explained in detail in Chapter 2. The methods used in solving the linearized Euler equations are described in Chapter 3 and the boundary conditions used are described and tested in Chapter 4. The Kirchhoff-Helmholtz integral method for extending an acoustic solution to the far-field is briefly presented in Chapter 5. In Chapter 6 modified linearized Euler equations are derived and compared to the original linearized Euler equations. A test of the numerical accuracy and stability of the utilized methods is presented in Chapter 7. In Chapter 8 source terms for the linearized Euler equations on conservative form are derived and validated in a forced 2D mixing layer. The methods presented in Chapters 2-8 are used in Chapter 9 to predict the sound generated in a high Mach number subsonic jet. The conclusions from the present work is presented in Chapter 10. Some of the more extensive derivations are left to the Appendix and are referred to in the text.

Chapter 2

Stochastic Noise Generation and Radiation Method

2.1 Overview

An aeroacoustic problem can be divided into generation of sound and propagation of the generated sound. Solving the full compressible Navier-Stokes equations using LES or DNS captures both. The computational cost however of the two methods is so great that it is virtually impossible to apply any of them to an industrial application. There has recently been some progress in a new modeling approach called SNGR [9, 10] (Stochastic Noise Generation and Radiation) model. It is based on the idea that the linearized Euler equations are an exact wave operator for acoustic perturbations. Introducing suitable sources to the linearized Euler equations result in accurate predictions of the propagation of acoustic perturbations.

In the case of jet noise predictions a RANS solution provides time averaged information about the flow field. The challenge in SNGR is then to use the information given from the RANS solution to generate an instationary turbulent field with the same local statistical properties as the RANS solution. This generated turbulent field is used to evaluate source terms in the linearized Euler equations. Solving the linearized Euler equations with the source terms provide the propagation of sound from the source region to the far-field.

The SNGR model is performed using three steps. These are:

step 1. A Reynolds-Averaged Navier-Stokes solution of a compressible turbulent jet is calculated, using for example, a $k - \varepsilon$ turbulence model.

step 2. An instationary turbulent velocity field with the same local turbulence kinetic energy, time scale and length scale as the RANS solution is generated using random Fourier modes.

step 3. The linearized Euler equations are solved using the mean flow field computed in step (1) as reference solution. Source terms derived in a similar way as for Lighthill's wave equation are evaluated using the turbulent field generated in step (2). This step (3) gives the propagation of sound from the turbulent field to the surrounding far-field.

2.2 RANS for Jet Computations

The Reynolds-Averaged Navier-Stokes solution (RANS) of the flow field is computed using a standard $k-\varepsilon$ turbulence model. The purpose of the RANS solution is to provide a reference solution for the following linearized Euler computation. The RANS solution is also used in the stochastic modeling of the turbulent field. The SNGR model needs input parameters in the form of turbulence kinetic energy, length scale and time scale. The turbulence kinetic energy is one of the solution variables from the RANS computation and the turbulence length scale and time scale are computed from the turbulence kinetic energy and the turbulence dissipation rate.

2.3 Linearized Euler Equations with Source Terms

A formal derivation of the source terms for the linearized Euler equations is given in Chapter 8. Given here is only the final set of equations.

$$
\begin{aligned}
\frac{\partial \rho'}{\partial t} + \frac{\partial (\rho u_j)'}{\partial x_j} &= 0 \\
\frac{\partial (\rho u_i)'}{\partial t} + \frac{\partial}{\partial x_j}(\widetilde{u}_j(\rho u_i)' + \widetilde{u}_i(\rho u_j)' - \rho'\widetilde{u}_i\widetilde{u}_j + p'\delta_{ij}) &= \\
-\frac{\partial}{\partial x_j}(\rho u_i'' u_j'' - \overline{\rho u_i'' u_j''}) & \qquad (2.1) \\
\frac{\partial (\rho e_0)'}{\partial t} + \frac{\partial}{\partial x_j}(\widetilde{h}_0(\rho u_j)' + \widetilde{u}_j(\rho h_0)' - \rho'\widetilde{h}_0\widetilde{u}_j) &= \\
-\frac{\partial}{\partial x_j}(\rho h_0'' u_j'' - \overline{\rho h_0'' u_j''}) &
\end{aligned}
$$

The left-hand side of equations 2.1 is the linearized Euler equations. The right-hand side contains all non-linearities that emerged when the Euler equations were rewritten into the linearized Euler equations. Thus, equations 2.1 are still the full non-linear Euler equations. If the right-hand side of the equations is treated as a source and is in some way known, then the left-hand side is a wave operator responding to the source. The right-hand side could be given from the solution of a Direct Numerical Simulation (DNS), or a Large Eddy Simulation (LES). This is done in the case of a 2D mixing layer in Chapter 8 as a validation of the source terms. The source terms are shown to be working well and given that they are evaluated from a physical solution, the response from the linearized Euler equations is in good agreement with the direct numerical simulation used to evaluate the source terms.

2.4 Stochastic Modeling

This section treats the generation of an instationary turbulent velocity field, i.e. Step (2) in the SNGR method. A large portion of this section follows the texts of Bailly and Juvé *et al.* [10] and Bechara *et al.* [9].

A time-space turbulent velocity field can be simulated using random Fourier modes. This was proposed by Kraichnan [11] and Karweit *et al.* [12] and further developed by Bechara *et al.* [9] and Bailly and Juvé [10]. The velocity field is given by

$$
\mathbf{u}_t(\mathbf{x}) = 2\sum_{n=1}^{N} \hat{u}_n \cos(\mathbf{k}_n \mathbf{x} + \psi_n)\sigma_n \qquad (2.2)
$$

where $\hat{u}_n$, ψ_n and σ_n are amplitude, phase and direction of the $n:th$ Fourier mode. Figure 2.1 shows the geometry of the $n:th$ mode in wave number space.

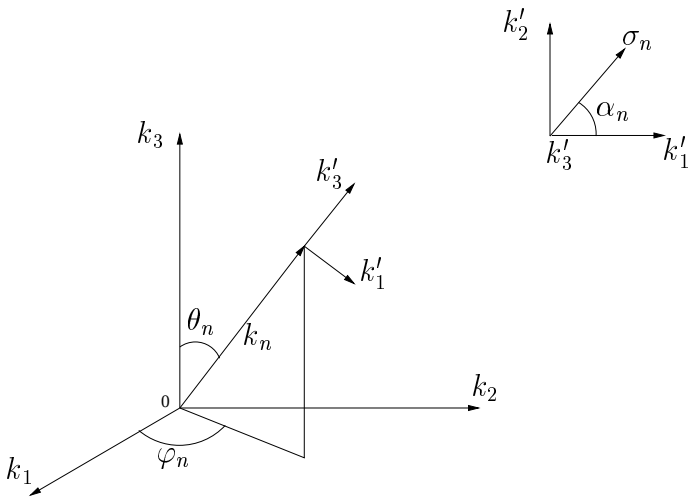

Figure 2.1: Geometry for the $n:th$ mode.

The vector $\mathbf{k}_n$ is chosen randomly on a sphere with radius k_n. This to ensure isotropy of the generated velocity field. By the assumption of incompressibility the continuity equation gives the following relation

$$\mathbf{k}_n \cdot \sigma_n \equiv 0 \qquad \text{for all} \qquad n \tag{2.3}$$

The wave number vector $\mathbf{k}_n$ and the spatial direction σ_n of the $n:th$ mode are thus perpendicular. The angle α_n is a free parameter chosen randomly, see figure 2.1. The phase of each mode ψ_n is chosen with uniform probability between $0 \leq \psi_n \leq 2\pi$. The probability functions of all the random functions φ_n, ψ_n, θ_n and α_n are given in table 2.1.

$p(\varphi_n) = 1/(2\pi)$	$0 \leq \varphi_n \leq 2\pi$
$p(\psi_n) = 1/(2\pi)$	$0 \leq \psi_n \leq 2\pi$
$p(\theta_n) = 1/(2)\sin(\theta)$	$0 \leq \theta_n \leq \pi$
$p(\alpha_n) = 1/(2\pi)$	$0 \leq \alpha_n \leq 2\pi$

Table 2.1: Probability distributions of random variables.

The probability function of θ, $p(\theta_n) = 1/2\sin(\theta)$ is chosen so that the distribution of the direction of $\mathbf{k}_n$ is uniform on the surface of a sphere, see figure 2.2, i.e. the probability of a randomly selected direction is the same for all surface elements $\mathrm{d}A$.

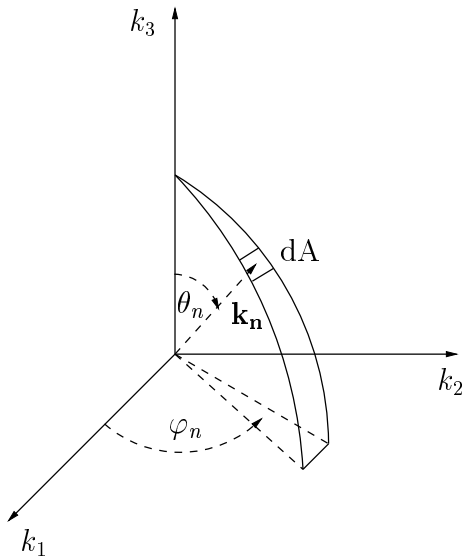

Figure 2.2: The probability of a randomly selected direction of a wave in wave-space is the same for all dA on the shell of a sphere.

The amplitude $\hat{u}_n$ of each mode is computed so that the turbulence kinetic energy $E(k_n)$ correspond to the energy spectrum for isotropic turbulence. This gives

$$\hat{u}_n = \sqrt{E(k_n)\Delta k_n} \tag{2.4}$$

where Δk_n is a small interval in the spectrum located at k_n, see figure 2.3. A model spectrum is used to simulate the shape of an energy spectrum for isotropic turbulence. In this way the sum of the squares of $\hat{u}_n$ over all n is equal to the total turbulence kinetic energy

$$\overline{k} = \sum_{n=1}^{N} \hat{u}_n^2 \tag{2.5}$$

The subdivision of the spectrum into different modes is chosen logarithmically as

$$k_n = e^{(\ln k_1 + (n-1)dk_l)} \qquad \text{for} \qquad n = 1, 2, \ldots, N \tag{2.6}$$

where

$$dk_l = \frac{\ln(k_N) - \ln(k_1)}{N-1} \tag{2.7}$$

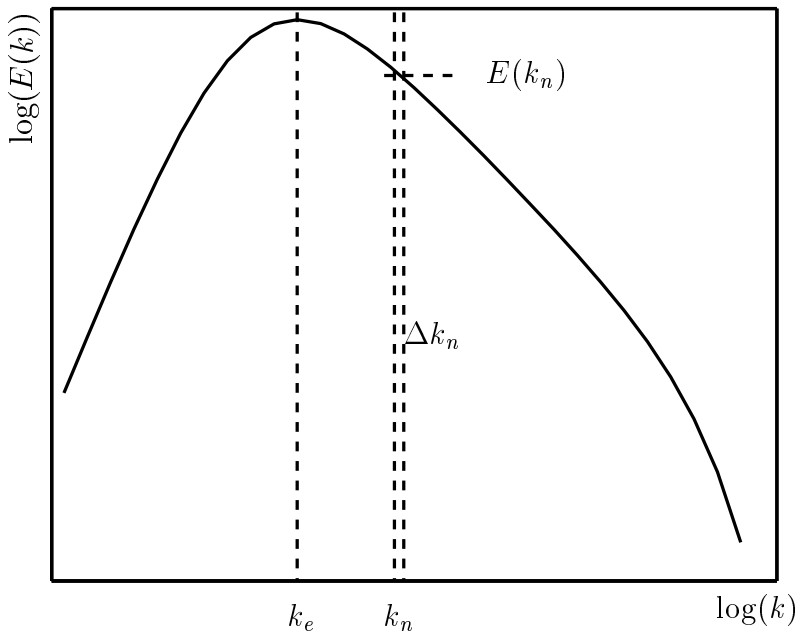

Figure 2.3: von Kármán-Pao spectrum

This distribution of the generated modes gives a better resolution of the spectrum for low wave numbers corresponding to the most energy containing eddies compared to a linear distribution.

The energy spectrum for isotropic turbulence is simulated by a von Kármán-Pao spectrum

$$E(k) = \alpha \frac{u'^2}{k_e} \frac{(k/k_e)^4}{[1 + (k/k_e)^2]^{17/6}} e^{[-2(k/k_\eta)^2]} \tag{2.8}$$

where k is the wave number, $k_\eta = \varepsilon^{1/4}\nu^{-3/4}$ is the Kolmogorov wave number, ν is the molecular viscosity and ε is the dissipation rate. u'^2 is the r.m.s. value of the velocity fluctuations corresponding to the turbulent kinetic energy, $u'^2 = 2\overline{k}/3$. There are two free parameters in equation 2.8. The numerical constant α which determines the kinetic energy of the spectrum and the wave number k_e corresponding to the most energy containing eddies at the peak in the spectrum. The available information from the RANS solution is the turbulence kinetic energy $\overline{k}$ or, equivalently $3u'^2/2$, and the dissipation rate ε. These must be used in order to determine α and k_e and thereby the shape of the spectrum and thus the distribution of energy over different wave numbers. The numerical constant α can be determined by the requi-

rement that the integral of the energy spectrum, equation 2.8, over all wave numbers should be equal to the total turbulent kinetic energy

$$\overline{k} = \int_0^\infty E(k)dk \tag{2.9}$$

Since equation 2.8 is derived for infinite Reynolds number α can be found independently of k_e by integrating equation 2.9 to get

$$\alpha = \frac{4}{\sqrt{\pi}} \frac{\Gamma(17/6)}{\Gamma(1/3)} \simeq 1.45276 \tag{2.10}$$

The turbulence length scale from the RANS solution is defined as $\Lambda = c_\mu^{0.75} \overline{k}^{3/2} / \varepsilon$. Assuming that the length scale from the RANS solution is the same as the integral length scale for isotropic turbulence gives the following relation

$$\Lambda = \frac{\pi}{2u'^2} \int_0^\infty \frac{E(k)}{k} dk \tag{2.11}$$

which is used to determine the wave number k_e corresponding to the most energetic length scales. The relation of k_e to Λ and α is

$$k_e = \frac{9\pi}{55} \frac{\alpha}{\Lambda} \tag{2.12}$$

where α is given in equation 2.10 and Λ is given from the RANS solution.

In earlier studies, two methods have been developed to introduce time dependence in the synthesized velocity field [9, 10]. The first method [9] is based on independent generation of every time step in the same manner as described above. The independent solutions are then filtered in time in every point to give a desired time correlation. The second method [10] is based on introduction of time dependence in the actual generation by adding a time dependent term in the Fourier modes. The generated time dependent turbulent velocity $\mathbf{u}_t(\mathbf{x}, t)$ is then given by

$$\mathbf{u}_t(\mathbf{x}, t) = 2 \sum_{n=1}^{N} \hat{u}_n \cos(\mathbf{k}_n(\mathbf{x} - t\mathbf{u}_c) + \psi_n + \omega_n t)\sigma_n \tag{2.13}$$

In this expression $\mathbf{u}_c$ is the local convection velocity computed in the RANS solution, and ω_n is the angular frequency of the $n:th$ generated mode. The angular frequency ω_n is a random function given by a Gaussian probability function

$$p(\omega_n) = \frac{1}{\overline{\omega}_n\sqrt{2\pi}} e^{(-\frac{(\omega_n-\overline{\omega}_n)^2}{2\overline{\omega}_n^2})} \tag{2.14}$$

where $\overline{\omega}_n$ is the mean angular frequency of the $n:th$ mode determined by $\overline{\omega}_n = u'k_n$, see [10].

The second method to introduce time dependence is more attractive from computational point of view due to the difference in required computational effort and storage. In the first method a number of Fourier modes have to be generated in each time step. The resulting velocity fields need to be filtered a posteriori to get suitable statistical properties. This data need to be stored before it is used in the source terms in the linearized Euler computation, step (3). In the second method the velocity field can be generated for each time step independently and does not need to be filtered. It is then possible to include the generation of the turbulent velocity field in the solver. The only data that need to be stored in order to repeat a computation in this case are the random functions given in table 2.1. The first method [9] is however more attractive in the way that the autocorrelation can be chosen to follow a specified behavior. This is done through the filtering of the independent samples. This type of control is not possible in the second method.

A way to retain the control of the autocorrelation and at the same time keep the required computational effort at a reasonable level is to introduce the time filter directly as the velocity field is generated. To include convectional effects a convection equation is solved for the filtered velocity field. The proposed method to introduce time dependence and convection is as follows. First define a realization of the generated turbulent velocity field as $\mathbf{u}_t^m(\mathbf{x})$ where superscript m denotes time step m. Each generated field $\mathbf{u}_t^m(\mathbf{x})$ for all $1 < m < N$ is independent of the others and have a zero statistical mean. In other words the generated velocity field is locally white noise. A new turbulent velocity field can then be computed via the equation

$$\mathbf{v}_t^m(\mathbf{x}) = a\mathbf{v}_t^{m-1}(\mathbf{x}) + b\mathbf{u}_t^m(\mathbf{x}) \tag{2.15}$$

where $a = \exp(-\Delta t/\tau)$ and $b = \sqrt{(1-a^2)}$. τ is referred to as the time scale and defines the time separation for which the autocorrelation fun-

ction is reduced to $\exp(-1)$. The expression for b ensures that the RMS of the outgoing signal $\mathbf{v}_t^m(\mathbf{x})$ is the same as the in-going signal $\mathbf{u}_t^m(\mathbf{x})$. For more details, see Appendix 11.6. The time scale is computed from the RANS solution as $\tau = \overline{k}/\varepsilon$. To account for convection of the generated turbulent field $\mathbf{v}_t^m(\mathbf{x})$ a simple convection equation is solved for $\mathbf{v}_t^{m-1}(\mathbf{x})$

$$\frac{\partial(\overline{\rho}\mathbf{v}_{ti}^{m-1})}{\partial t} + \frac{\partial(\overline{\rho u_j}\mathbf{v}_{ti}^{m-1})}{\partial x_j} = 0 \tag{2.16}$$

before it is used in equation 2.15. Absorbing boundary conditions based on characteristic variables are used when solving equation 2.16.

2.5 Correlations of Generated Turbulence

To see if the generated turbulent velocity field has the specified time and length scales, the autocorrelation and two-point correlations are computed from the generated velocity field.

Using a first-order filter as in equation 2.15, the specified autocorrelation is an exponentially decaying function which in a discrete time separation is

$$\frac{\overline{\mathbf{v}_t^m \mathbf{v}_t^{m-p}}}{\overline{(\mathbf{v}_t^m)^2}} = a^p \tag{2.17}$$

where p is the number of time steps separating $\mathbf{v}_t^m$ and $\mathbf{v}_t^{m-p}$ and the overline denotes an average over many realizations m. The specified and the computed autocorrelations are shown in figure 2.4.

The longitudinal two-point correlation $\overline{uu}(r,0,0)/\overline{uu}(0,0,0)$ is compared to the f-function for isotropic turbulence [13] and the transversal $\overline{vv}(r,0,0)/\overline{vv}(0,0,0)$ is compared to the g-function. Definitions of the f- and g-functions are given in Appendix 11.5. The results are shown in figure 2.5. The correlations in time and space clearly follow the specified correlations.

2.6 Source Region

The region in which the SNGR is applied is restricted to the region where the largest sources are expected. This region is a cylinder that

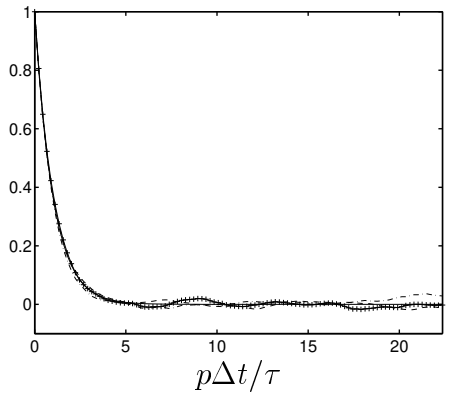

Figure 2.4: Autocorrelation $\overline{\mathbf{v}_t^m \mathbf{v}_t^{m-p}}/\overline{(\mathbf{v}_t^m)^2}$ for generated turbulence as a function of normalized time separation $p\Delta t/\tau$. First-order filter in time. Solid line: analytical expression, 2.17; others: x_1, x_2, x_3 velocity autocorrelation.

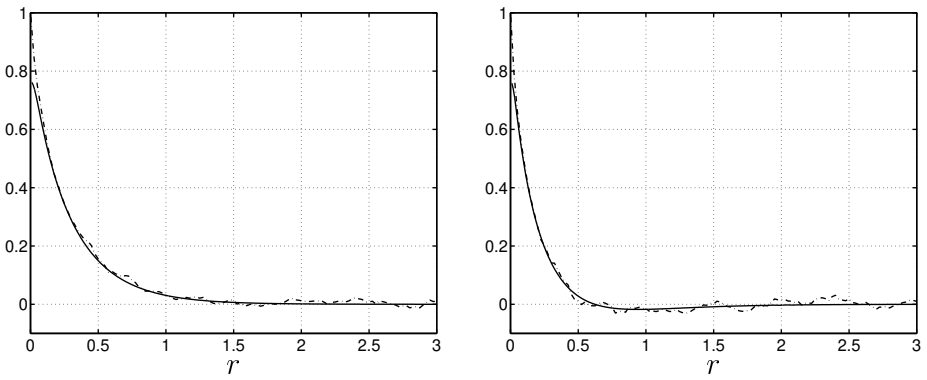

(a) $\overline{uu}(r,0,0)/\overline{uu}(0,0,0)$ (b) $\overline{vv}(r,0,0)/\overline{vv}(0,0,0)$

Figure 2.5: Spatial two-point correlations. (a) longitudinal two-point correlation, (b) transversal two-point correlation. Solid lines: analytical expressions; dashed lines: from generated turbulent velocity fields.

starts from the nozzle and continues in the axial direction down to the end of the transition region. Within this cylinder the source region is the set of cells where $\nu_t/\nu \geq 0.7$. This limit is chosen for numerical reasons to ensure that the Kolmogorov wave number is larger than the peak wave number k_e in the model von Kármán-Pao energy spectrum.

Chapter 3

Linearized Euler Equation Solver

3.1 Finite Volume Method

The solver for the linearized Euler equations is based on the G3D [14] series of codes developed by Lars-Erik Eriksson at Volvo Aero Corporation. These codes solve compressible flow equations on conservative form on a general structured boundary-fitted, curve-linear non-orthogonal multi-block mesh. The solver in the present work is an extended version of a code for solving the Linearized Euler equations in CFD applications. The developments in the present thesis consist of increased numerical accuracy required for Computational AeroAcoustics (CAA). In the present state the code uses an explicit four stage Runge-Kutta time marching technique. The convective fluxes are evaluated using a six point finite volume stencil. Upwinding of the convective fluxes based on characteristic variables is used to ensure numerical stability. The Finite Volume Method (FVM) used in this work is described below.

The governing equations can be written on a compact conservative form as

$$\frac{\partial Q}{\partial t} + \frac{\partial F_j}{\partial x_j} = 0 \tag{3.1}$$

where

$$Q = \begin{pmatrix} \rho' \\ (\rho u_i)' \\ (\rho e_0)' \end{pmatrix} \qquad F_j = \begin{pmatrix} (\rho u_j)' \\ \widetilde{u}_j(\rho u_i)' + \widetilde{u}_i(\rho u_j)' - \rho'\widetilde{u}_i\widetilde{u}_j + p'\delta_{ij} \\ \widetilde{h}_0(\rho u_j)' + \widetilde{u}_j(\rho h_0)' - \rho'\widetilde{h}_0\widetilde{u}_j \end{pmatrix} \tag{3.2}$$

Equations 3.1 are discretized on a structured, non-orthogonal multi-block boundary fitted mesh. This is done by integrating 3.1 over an arbitrary control volume Ω

$$\int_\Omega \frac{\partial Q}{\partial t}\mathrm{dV} + \int_\Omega \frac{\partial F_j}{\partial x_j}\mathrm{dV} = 0 \tag{3.3}$$

Introducing a volume average $\overline{Q}$ of Q over Ω and using Gauss theorem on the second term we can write

$$V\frac{\partial \overline{Q}}{\partial t} + \int_{\partial\Omega} F_j \cdot \mathrm{dS_j} = 0 \tag{3.4}$$

where $dS_j = n_j dS$ is a surface normal element on $\partial\Omega$. In words equation 3.4 says that the rate of change of the volume average of the state vector Q is equal to the integral of the flux through the boundary of volume Ω. If Ω is the volume defining a cell in a computational mesh the flux term can be rewritten as the sum of the fluxes through the cell faces of control volume Ω

$$\int_{\partial\Omega} F_j \cdot \mathrm{dS_j} = \sum_{all\,faces} \int_{face} F_j \cdot \mathrm{dS_j} \tag{3.5}$$

Assuming that F_j is constant over each face, equation 3.5 can be written as

$$\int_{\partial\Omega} F_j \cdot \mathrm{dS_j} = \sum_{all\,faces} F_j^{face} \cdot S_j^{face} \tag{3.6}$$

where S_j^{face} is the surface normal vector times the surface area of the face. The governing equations discretized on a structured mesh can now be written as

$$V\frac{\partial \overline{Q}}{\partial t} + \sum_{all faces} F_j^{face} \cdot S_j^{face} = 0 \tag{3.7}$$

Solving equation 3.7 is done by estimating the values of F_j on the faces and then use a time marching technique to advance the solution in time. The procedure is then repeated using the new solution from the last time step.

3.2 Convective Fluxes and Artificial Dissipation

The convective fluxes are computed using an approach based on characteristic variables. The reason for this is to be able to add a small amount of artificial numerical dissipation. The artificial numerical dissipation is added through upwinding of the convective scheme. The characteristic variables are used to decide in which direction to perform the upwinding. The methodology is as follows.

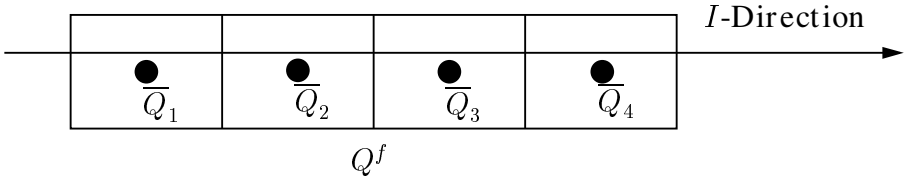

Figure 3.1: Estimation of face value Q^f is based on cell averages $\overline{Q}_1$ to $\overline{Q}_4$.

The solution vector Q is computed on the face in a right-hand side upwinded version and a left-hand side upwinded version. The upwinding is based on adding a dissipative term to the system of equations. This term is multiplied by a small number ε to add a small amount of dissipation, see Appendix 11.2. This is illustrated here using a four point stencil.

$$\begin{aligned} Q_L^f &= C_1\overline{Q}_1 + C_2\overline{Q}_2 + C_3\overline{Q}_3 + C_4\overline{Q}_4 \\ Q_R^f &= C_4\overline{Q}_1 + C_3\overline{Q}_2 + C_2\overline{Q}_3 + C_1\overline{Q}_4 \end{aligned} \tag{3.8}$$

where Q_L^f is the left side upwinded and Q_R^f is the right side upwinded estimates on the face. The coefficients C_1, C_2, C_3, C_4 specify the numerical scheme and amount of upwinding. An average of the two neighboring cells is also computed

$$Q_a = 0.5(\overline{Q}_2 + \overline{Q}_3) \tag{3.9}$$

The left and right-hand side upwinded solution vectors Q_f^L and Q_f^R are transformed in the I-direction into vectors for the characteristic variables, $W_L^{(n)}$ and $W_R^{(n)}$, see Appendix 11.3 and the eigenvalue associated to each characteristic variable, $\lambda^{(n)}$, is computed using the average solution Q_a. In three dimensions there are five characteristic variables corresponding to entropy, vorticity and acoustic waves. There are one entropy, two vorticity and two acoustic waves. The eigenvalue associated to each characteristic variable represents the velocity of each wave.

The solution is transformed back from characteristic variables to physical variables using information about the eigenvalues. If the eigenvalue $\lambda^{(n)}$ associated to the characteristic variable $W^{(n)}$ is positive, the left-hand side upwinded version is used in the transformation back to physical variables and if the eigenvalue $\lambda^{(n)}$ is negative, the right-hand side upwinded version is used. This corresponds to an upwinding of each characteristic variable depending on the direction in which the wave is traveling through the face. Finally the flux through the face, equation 3.7, is computed using the solution estimated on the face.

The numerical scheme used in the present work is the six cell finite volume version of the fourth-order Dispersion Relation Preserving (DRP) scheme proposed by Tam [15]. The coefficients are given in Appendix 11.4. A sixth-order derivative of the solution vector is used in the upwinding of the numerical scheme. The resulting dispersion relation and dissipation relation are shown in Appendix 11.2.

3.3 Time Marching

When the spatial fluxes are computed as in the section above, equation 3.7 can be written on the form

$$\frac{\partial \overline{Q}}{\partial t} = \mathcal{F} \tag{3.10}$$

where $\mathcal{F}$ is an approximation of the sum of the spatial fluxes. The time integration is performed using a four stage 4:th order Runge-Kutta time marching technique

$$
\begin{aligned}
\overline{Q}^{*} &= \overline{Q}_j^n + \frac{1}{4}\Delta t \mathcal{F} \mid_{\overline{Q}^n} \\
\overline{Q}^{**} &= \overline{Q}_j^n + \frac{1}{3}\Delta t \mathcal{F} \mid_{\overline{Q}^*} \\
\overline{Q}^{***} &= \overline{Q}_j^n + \frac{1}{2}\Delta t \mathcal{F} \mid_{\overline{Q}^{**}} \\
\overline{Q}^{n+1} &= \overline{Q}_j^n + \Delta t \mathcal{F} \mid_{\overline{Q}^{***}}
\end{aligned}
\tag{3.11}
$$

where $\overline{Q}^n$ is the solution at time step n and $\overline{Q}^{n+1}$ is the computed solution at time step $n+1$.

The time step Δt is chosen such that the highest CFL-number in the computational domain is below a specified value. The time step is given by $\Delta t = \mathrm{CFL}/\mathrm{SR}$ where SR is the convective spectral radius [16]. The numerical scheme is stable up to CFL about unity. The maximum CFL-number is however chosen to 0.5 in most computations. Above this CFL-number the amplitude error caused by the artificial numerical dissipation starts to become important for low wave numbers. See Appendix 11.2 for a stability analysis of the fully discretized equations using the above specified scheme.

Chapter 4

Absorbing Boundary Conditions

The boundary conditions must give information to the equations about what the conditions are at the boundaries, i.e. the boundary conditions must specify the state of the fluid at all boundaries, whether is is an inflow, wall, periodic, outflow or any other boundary. At free boundaries however, the boundary conditions must simulate that there is no boundary present at all. Information reaching the boundary must be let out without causing reflection of information back into the computational domain.

There are two major types of local non-reflective or absorbing boundary conditions. The first type is based on a local analysis of the governing equations in terms of characteristic variables. Most of the work on this method is done by Thompson [17, 18] and Poinsot and Lele [19]. The major assumption made in deriving these types of boundary conditions is that the outgoing disturbances are plane waves with zero incidence angle to the boundary. For such waves these boundary conditions are in fact exact and result in zero reflection. For waves with non-zero incidence angle to the boundary there will however be reflections.

The other type is based on an asymptotic analysis of the Euler equations at very large distances from the source. This method was originally suggested by Bayliss and Turkel [20]. Tam and Webb [15] developed 2D boundary conditions based on this idea and Tam and Dong [21] extended the boundary conditions to include a non-uniform mean flow. Bogey and Bailly [22] have developed using the same methods a generalization of these boundary conditions in spherical coordinates for a 3-D geometry.

Generally the methods based on asymptotic analysis of the Euler

equations have been shown to be more efficient in absorbing disturbances than the methods based on characteristic variables. This is shown in Hixon *et al.* [23]. The reason for this is the assumption that the disturbances approach the boundary at zero incidence angle in the boundary conditions based on characteristic variables. One drawback with the boundary conditions based on asymptotic analysis of Euler equations is that the location of the source of the disturbances has to be specified. Formally this is a big disadvantage, but the region with the strongest sources in a flow is often known which makes it possible to specify an approximate source location.

4.1 Characteristic Variable Based Absorbing Boundary Conditions (Cvba)

The boundary conditions presented here are similar to the ones presented by Thompson [17, 18] but the details are not the same. The formulation of the boundary conditions presented here is derived by Eriksson [24]. The boundary conditions are based on characteristic variable based representation of the governing equations in the direction of the outward facing normal vector $\mathbf{n}$. This transformation is presented in Appendix 11.3 and only the outline is given in this section. The governing equations can be transformed into a set of decoupled equations in one direction. The transformed equations govern propagation of planar waves in the direction of the analysis. The degrees of freedom are five variables called characteristic variables, $W^{(i)}$, each governed by an equation

$$\frac{\partial W^{(i)}}{\partial t} + \lambda^{(i)} \frac{\partial W^{(i)}}{\partial \xi} = 0 \tag{4.1}$$

where $\lambda^{(i)}$ is the characteristic speed associated with the characteristic variable and ξ is the spatial independent variable in the $\mathbf{n}$-direction.

The sign of the characteristic speeds λ^i at the boundary gives information about the direction the characteristic variable $W^{(i)}$is traveling. This information is used to set up the boundary conditions. The boundary condition is set up as

$$\begin{array}{lll} \text{Specify } W^{(i)} \text{ at boundary} & \text{if} & \lambda^{(i)} \leq 0 \\ \text{Extrapolate } W^{(i)} \text{ from interior domain} & \text{if} & \lambda^{(i)} \geq 0 \end{array} \tag{4.2}$$

The expressions above state that if information of $W^{(i)}$ is transported into the domain, the value of $W^{(i)}$ has to be given as a boundary condition. If the information of $W^{(i)}$ is transported from the inside of the domain, towards the boundary, the value of $W^{(i)}$ does not need to be specified and $W^{(i)}$ is extrapolated from the solution. When the appropriate action has been made on each characteristic variable, the solution is transformed back into the state variables again using equation 11.48.

This boundary condition gives complete absorption of waves propagating normally towards the boundary. For waves with oblique incidence to the boundary there will only be a partial absorption, see figure 4.1.

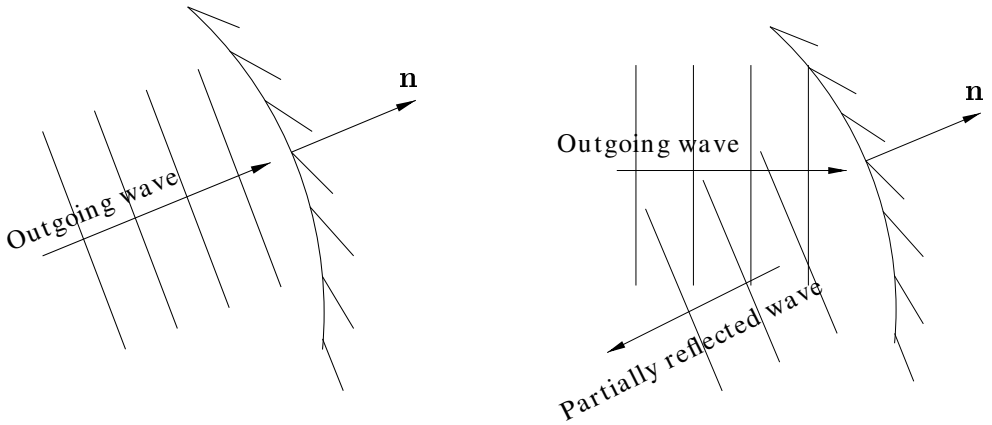

Figure 4.1: Absorbed wave v.s. partially reflected wave.

4.2 Modified Characteristic Variable Based Absorbing Boundary Conditions (Cvba)

The modified boundary conditions based on characteristic variables are equal to the original boundary conditions based on characteristic variables except for one detail. The original boundary conditions are completely absorbing for waves traveling with normal incidence to the boundary. This is a result of choosing the boundary normal vector $\mathbf{n}$ as direction for the local analysis describes above. The idea with the modified version of the original boundary conditions is that if the direction of the waves propagating towards the boundary is known, the local

analysis of the governing equations is made in that direction. This leads to complete absorption in this direction, see figure 4.2. The problem is then to choose the direction in which performing the analysis. Waves can however come from several different directions at the same time, so is can be hard to choose the direction in which to apply the boundary condition.

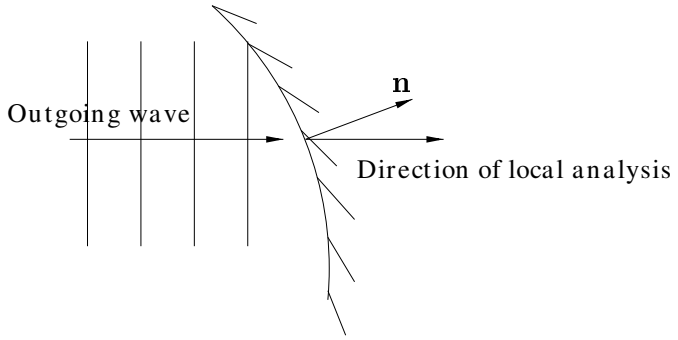

4.3 Boundary Conditions Based on Asymptotic Analysis of The Euler Equations

Boundary conditions for far-field radiation have been proposed by Bayliss and Turkel [20]. Similarly, Tam and Webb [15] developed non-reflecting boundary conditions using an asymptotic analysis of the Euler equations in two dimensions. These boundary conditions were further developed by Tam and Dong [21] to include non-uniform mean flow. These boundary conditions were in polar coordinates for a 2-D geometry. Bogey and Bailly [22] developed a generalization of these boundary conditions in spherical coordinates for a 3-D geometry. These boundary conditions have not been used in the present work but they are compared with in boundary condition test cases below.

To formulate the boundary conditions the flow is written as the sum of acoustic, vorticity and entropy waves. These are assumed to be independent which is only true for a uniform mean flow. Flow perturbations can then be written as

$$\begin{pmatrix} \rho' \\ \mathbf{u}' \\ p' \end{pmatrix} = \begin{pmatrix} \rho_a \\ \mathbf{u}_a \\ p_a \end{pmatrix} + \begin{pmatrix} 0 \\ \psi \\ 0 \end{pmatrix} + \begin{pmatrix} \chi \\ 0 \\ 0 \end{pmatrix} \tag{4.3}$$

where entropy and vorticity waves are convected by the mean flow, i.e. $\psi = \psi(\mathbf{x}-\overline{\mathbf{u}}t)$ and $\chi = \chi(\mathbf{x}-\overline{\mathbf{u}}t)$. Disturbances reaching the far-field consist of acoustic waves only, $(\rho_a, \mathbf{u}_a, p_a)$. Assuming that these are isentropic they can be written in the following form in spherical coordinates

$$\begin{pmatrix} \rho_a \\ \mathbf{u}_a \\ p_a \end{pmatrix} \sim \frac{F(r/v_g - t)}{r} \begin{pmatrix} 1/\bar{c}^2 \\ 1/(\bar{\rho}\bar{c})\mathbf{e}_r \\ 1 \end{pmatrix} \tag{4.4}$$

where the speed of sound wave propagation is defined as

$$v_g = (\overline{\mathbf{u}} + \overline{c}) \cdot \mathbf{e}_r \tag{4.5}$$

Radiation Boundary Conditions

Since only acoustic disturbances reach the radiation boundary, the solution is given by equation 4.3 with $\psi = 0$ and $\chi = 0$ and the appropriate boundary conditions are given by the differential equation satisfying equation 4.4.

$$\frac{\partial}{\partial t} \begin{pmatrix} \rho' \\ \mathbf{u}' \\ p' \end{pmatrix} + v_g \left(\frac{\partial}{\partial r} + \frac{1}{r} \right) \begin{pmatrix} \rho' \\ \mathbf{u}' \\ p' \end{pmatrix} = 0 \tag{4.6}$$

Equation 4.6 is used to set up boundary conditions at all radiation boundaries.

Outflow Boundary Conditions

In the outflow region both vorticity and entropy waves reach the boundary as well as acoustic waves. Therefore, the full expression of equation 4.3 has to be considered. The pressure fluctuations are assumed to be associated with the acoustic wave alone as shown in equation 4.3. Thus, the differential equation for the radiation boundary can be retained for the pressure at the outflow boundary.

$$\frac{\partial p'}{\partial t} + v_g \left(\frac{\partial}{\partial r} + \frac{1}{r} \right) p' = 0 \tag{4.7}$$

Taking the material derivative of density and velocity in equation 4.3 yields

$$\begin{aligned} \frac{\partial \rho'}{\partial t} + \overline{\mathbf{u}} \cdot \nabla \rho' &= \frac{\partial \rho_a}{\partial t} + \overline{\mathbf{u}} \cdot \nabla \rho_a \\ \frac{\partial \mathbf{u}'}{\partial t} + \overline{\mathbf{u}} \cdot \nabla \mathbf{u}' &= \frac{\partial \mathbf{u}_a}{\partial t} + \overline{\mathbf{u}} \cdot \nabla \mathbf{u}_a \end{aligned} \tag{4.8}$$

The isentropic relation between acoustic pressure and density disturbances allows us to rewrite the density outflow condition, equation 4.8 as

$$\frac{\partial \rho'}{\partial t} + \overline{\mathbf{u}} \cdot \nabla \rho' = \frac{1}{\bar{c}^2} \left(\frac{\partial p_a}{\partial t} + \overline{\mathbf{u}} \cdot \nabla p_a \right) \tag{4.9}$$

Since the acoustic perturbations satisfy the linearized inviscid momentum equation, the velocity outflow boundary condition, equation 4.8, can be written as

$$\frac{\partial \mathbf{u}'}{\partial t} + \overline{\mathbf{u}} \cdot \nabla \mathbf{u}' = -\frac{1}{\overline{\rho}} \nabla p_a \tag{4.10}$$

Since the pressure disturbances are assumed to be acoustic disturbances alone, the system of equation to be solved in the outflow region is

$$\begin{aligned} \frac{\partial \rho'}{\partial t} + \overline{\mathbf{u}} \cdot \nabla \rho' &= \frac{1}{\bar{c}^2} \left(\frac{\partial p'}{\partial t} + \overline{\mathbf{u}} \cdot \nabla p' \right) \\ \frac{\partial \mathbf{u}'}{\partial t} + \overline{\mathbf{u}} \cdot \nabla \mathbf{u}' &= -\frac{1}{\overline{\rho}} \nabla p' \\ \frac{\partial p'}{\partial t} + v_g \left(\frac{\partial}{\partial r} + \frac{1}{r} \right) p' &= 0 \end{aligned} \tag{4.11}$$

These outflow boundary conditions, equation 4.11 and radiation boundary conditions, equation 4.6 are typically applied by solving these equations in the cells closest to the boundary instead of the full linearized Euler equations. The spatial fluxes are taken with non-centered schemes [21, 22].

4.4 Buffer Layer

At the far-field and inflow boundary the only disturbances reaching the boundary are acoustic waves. The energy content in sound waves is usually very small and even if there is a small fraction of the

disturbance which is reflected back into the computational domain the amplitude of the reflected wave will be very small.

At the outflow however there are vorticity and entropy disturbances convected with the flow reaching the boundary as well as acoustic disturbances. The energy content in vorticity and entropy waves is very large at the outflow compared to acoustic waves. So if the boundary condition at the outflow does not completely absorb all energy from the vorticity and entropy disturbances very large acoustic disturbances will reflect back into the computational domain. These waves will be an artifact of poor boundary conditions and not part of the correct solution. This contamination of the solution must be avoided. To ensure that there are no reflections from the outflow region a buffer layer is often applied. The buffer region is an extension of the computational domain in the downstream direction in which extra terms are added to the equations. The way this is done was first proposed by Colonius *et al.* [25]. Assuming that the buffer layer is in the x-direction, the terms added to the governing equations are

$$\frac{\partial Q'}{\partial t} = \cdots - \frac{c\sigma(x,y)}{(x_{max} - x_0)}(Q') \tag{4.12}$$

where

$$\sigma(x,y) = \sigma_{max}\left(\frac{x - x_0}{x_{max} - x_0}\right)^2 \tag{4.13}$$

The strength of the buffer layer, σ_{max}, is chosen to achieve a certain amount of damping and x_0 and x_{max} define the beginning and end of the buffer region. The parabolic shape of $\sigma(x,y)$ reduces the risk that the damping term will cause reflections into the computational domain.

4.5 Test of Absorbing Boundary Conditions

The boundary conditions by Thompson [17, 18] and Tam and Webb [15] have been tested by Hixon *et al.* [23] using a monopole in an axisymmetric flow field. In a 2D geometry Hixon *et al.* [26] also proposed test cases including both vortical and acoustic waves. Bogey and Bailly [22] have proposed two boundary condition test cases for boundary conditions formulated in three dimensions. The first case consists of a

Gaussian acoustic pulse in a uniform mean flow and the second is a axisymmetric vortex in a uniform mean flow. The boundary conditions tested in [22] were an extension to three dimensions of the boundary conditions proposed by Tam and Dong [21]. The test showed that the boundary conditions performed well as non-reflective boundary conditions for an acoustic pulse. In the vortex test case there was some reflection into the computational domain. For comparison the two test cases suggested by Bogey and Bailly are in the present thesis performed using the boundary conditions based on characteristic variables (Cvba) and the modified boundary conditions based on characteristic variables (MCvba). The computational setup and the results are presented and discussed below.

The computational mesh consists of a N^3 mesh with $N = 100$ cells. The spatial extent of the mesh is $-50 \leq x_1, x_2, x_3 \leq 50$ with a constant cell size $\Delta = 1$. The following normalization is used

length scale	:	Δ	cell size
velocity scale	:	c_0	ambient speed of sound
time scale	:	Δ/c_0	
density scale	:	ρ_0	ambient density
pressure scale	:	$\rho_0 c_0^2$	

In the test cases below the L_2-norm of the pressure disturbance is computed for each time step. This is used as a measure of the performance of the boundary conditions. The norm is defined by

$$L_2(t) = \left[\frac{1}{N^3} \sum_{i,j,k}^{N^3} p'^2_{i,j,k}(t) \right]^{1/2} \tag{4.14}$$

Gaussian Acoustic Pulse

The first test case consists of an initial Gaussian acoustic pulse in a mean flow in the x_1-direction with Mach number $M = 0.5$, mean density $\overline{\rho} = 1$ and mean pressure $\overline{p} = 1/\gamma$. The initial condition is

$$\begin{aligned} \rho' &= \epsilon \exp[-\alpha r^2] \\ u_1' &= 0 \\ u_2' &= 0 \\ u_3' &= 0 \\ p' &= \epsilon \exp[-\alpha r^2] \end{aligned} \tag{4.15}$$

where $\alpha = (\ln 2)/b^2$, $b = 3$, $\epsilon = 10^{-3}$ and r is the radius from the center of the pulse located in origo. More details on the test case can be found in [22].

The pressure disturbances $|p'|/\epsilon$ in the Ox_1x_2 plane are shown in figure 4.2. The left column represents the Cvba boundary conditions at times $t = 40$, 80 and 120. The right column represents the MCvba boundary conditions at the same times. In the test by Bogey and Bailly there were no visible reflections back into the computational domain using the same scale for the iso-contours as in figure 4.2. The results using the Cvba and MCvba show clear reflections. The outgoing wave reaches the boundary with a level of $|p'|/\epsilon \approx 0.02$. The reflected waves from the boundaries have an amplitude of $|p'|/\epsilon \approx 0.001$ or about 5% of the original wave amplitude. In the test by Bogey and Bailly the reflection was below 2% and below the scale of the iso-contours.

The time history of the L_2 norm for the acoustic pulse is shown in figure 4.3(a). The norm is normalized by the initial value of the norm at time $t = 0$. The norm decreases in steps as the pulse reaches the outflow, side and inflow boundaries. The non-zero value of $L_2 \approx 3 \times 10^{-2}$ at times $t > 150$ represents the amount of reflected waves. This correspond to about one order of magnitude lower compared to the initial value. The corresponding result of Bogey and Bailly is about two order of magnitude decrease of the L_2 norm at time $t = 150$.

The results from the modified and the original Cvba boundary conditions are similar with just slightly less reflection from the modified boundary conditions. One would expect the modified boundary conditions to perform better than the original boundary conditions. But it should be noted that the direction of the one dimensional analysis was specified as if the source was located in the center of the computational domain, $(x_0, y_0, z_0) = (0, 0, 0)$. The center of the source is however moving with the local convection speed so the estimate is actually not such a good approximation by the time the acoustic pulse reaches the boundary.

To illustrate the point the same computation was performed using the modified Cvba in which the origin of the moving source was specified as $(x_0, y_0, z_0) = (\overline{u}t, 0, 0)$. The resulting pressure iso-contours are show in the right column of figure 4.2 and the L_2 norm is the dash-dotted line in figure 4.3(a). The result is much improved up till $t = 140$. The increase in the norm after $t = 140$ is related to that the source by then is outside the computational domain and thus inverting the direction of the one dimensional analysis for the outflow boundary. The result is encouraging since the source location is often approximately

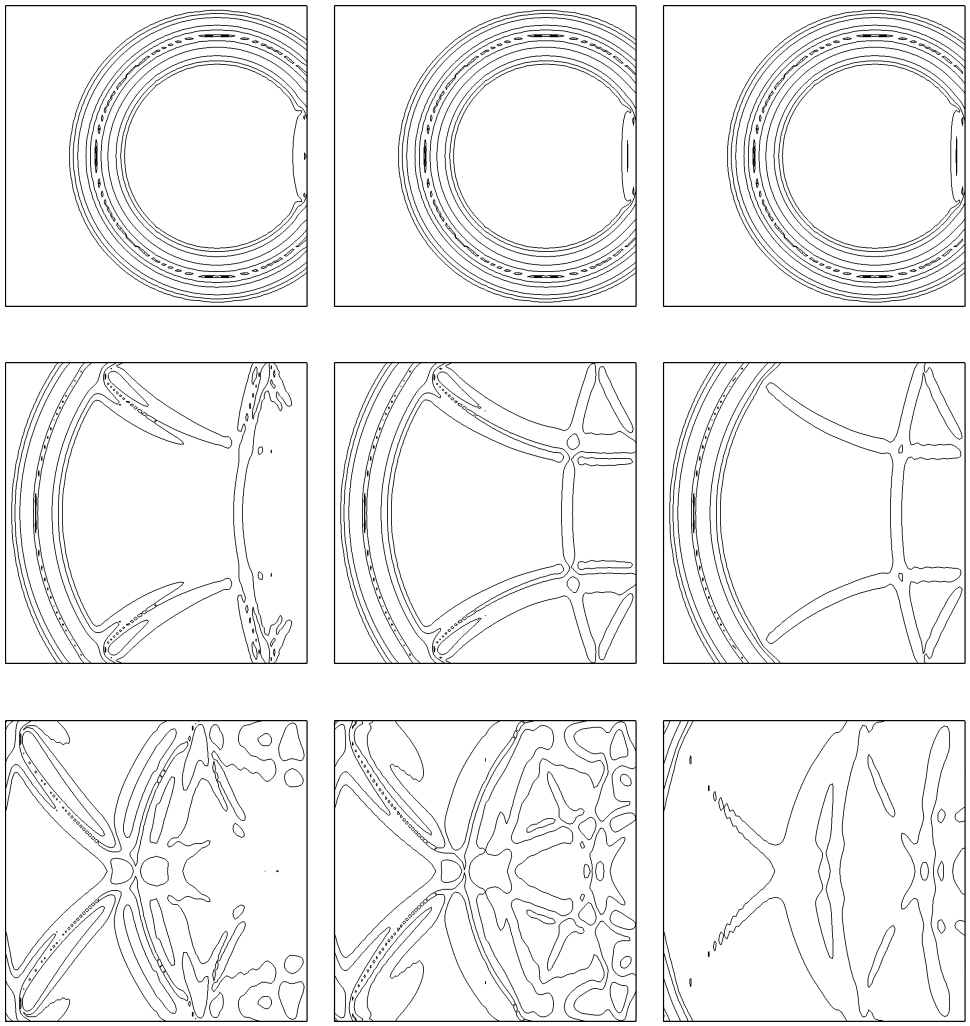

Figure 4.2: Scaled pressure disturbance $|p|/\varepsilon$. **Left column**: Characteristic variable based boundary conditions, Cvba. **Center column**: Modified Cvba. **Right column**: Modified Cvba with moving source correction. At times $t = 40$, 80 and 120. Iso-contours from 2.5×10^{-4} to 1.6×10^{-2} using 4 levels with a geometrical ratio of 4.

known and the modified boundary conditions would in that case be efficient as absorbing boundary conditions for acoustic disturbances.

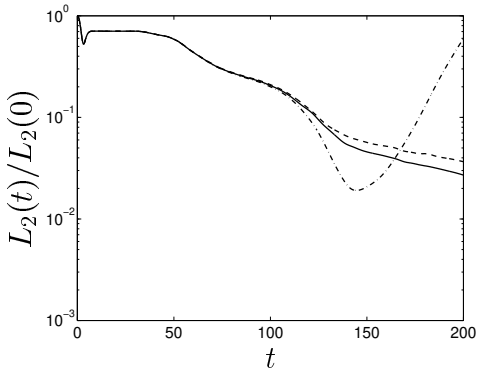

(a) Gaussian acoustic pulse in uniform mean flow. $L_2/L_2(0)$ as a function of time.

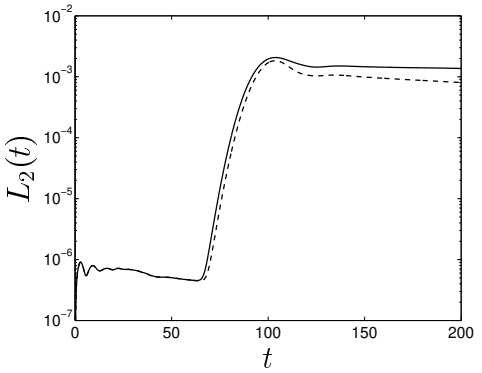

(b) Axisymmetric vortex in uniform mean flow. L_2 as a function of time.

Figure 4.3: Evaluation of boundary conditions. (a) Gaussian acoustic pulse in uniform mean flow, (b) axisymmetric vortex in uniform mean flow. Solid lines: modified Cvba boundary conditions; dashed lines: Cvba boundary conditions.; dash-dotted line in (a): modified Cvba boundary conditions with moving source specified

Convected Axisymmetric Vortex

The second test case proposed in [22] is that of a convected axisymmetric vortex. The mean flow is defined by $\overline{\rho} = 1$, $\overline{\mathbf{u}} = (M, 0, 0)$, $M = 0.5$, $\overline{p} = 1/\gamma$. The initial velocity disturbance is defined by

$$\begin{aligned} u_x &= \epsilon \frac{r_0}{r}(r - r_0)\exp\left[-\alpha\left(x_1^2 + (r - r_0)^2\right)\right] \\ u_r &= -\epsilon \frac{r_0}{r} x_1 \exp\left[-\alpha\left(x_1^2 + (r - r_0)^2\right)\right] \end{aligned} \tag{4.16}$$

where

$$x = x_1, \quad r = (x_2^2 + x_3^2)^{1/2}, \quad \theta = \arctan(x_3/x_2) \tag{4.17}$$

The vortex radius is $r_0 = 20$, $\alpha = (\ln 2)/b^2$, $b = 5$ and $\epsilon = 0.03$. The initial density and pressure disturbances are set to zero.

The vorticity magnitude $|\omega_3| = |\partial u_2'/\partial x_1 - \partial u_1'/\partial x_2|$ in the Ox_1x_2 plane is shown in the left column of figure 4.4 and the pressure disturbance in the right column. The times are $t = 50$, 100 and 150. The figures show the vortex as it is convected out of the computational domain. The pressure iso-contours are chosen so that the initial pressure disturbance in the vortex is smaller than the lowest iso-contour. When the vortex is convected through the boundary, it generates acoustic waves which propagate into the domain and contaminate the computational domain.

The time history of the L_2 norm of the pressure disturbance is shown in figure 4.3(b). An initial disturbance is generated from the sudden start of the vortex. The hydrodynamic pressure disturbance associated with the vortex is settled after $t \approx 20$ with a norm $L_2 = 6 \times 10^{-7}$. When the vortex reaches the boundary at about $t = 70$, reflection of acoustic waves cause a drastic increase in the L_2 norm with a peak of $L_2 = 2 \times 10^{-3}$ when the vortex center reaches the boundary at $t = 103$. This represent an increase in the L_2 norm of about 3.5 orders of magnitude. The corresponding result from the test by Bogey and Bailly [22] is an increase in the L_2 norm of about 2 orders of magnitude. Clearly the boundary conditions based on asymptotic analysis of the Euler equations are much more efficient as absorbing boundary conditions for vorticity than the characteristical variable based boundary conditions.

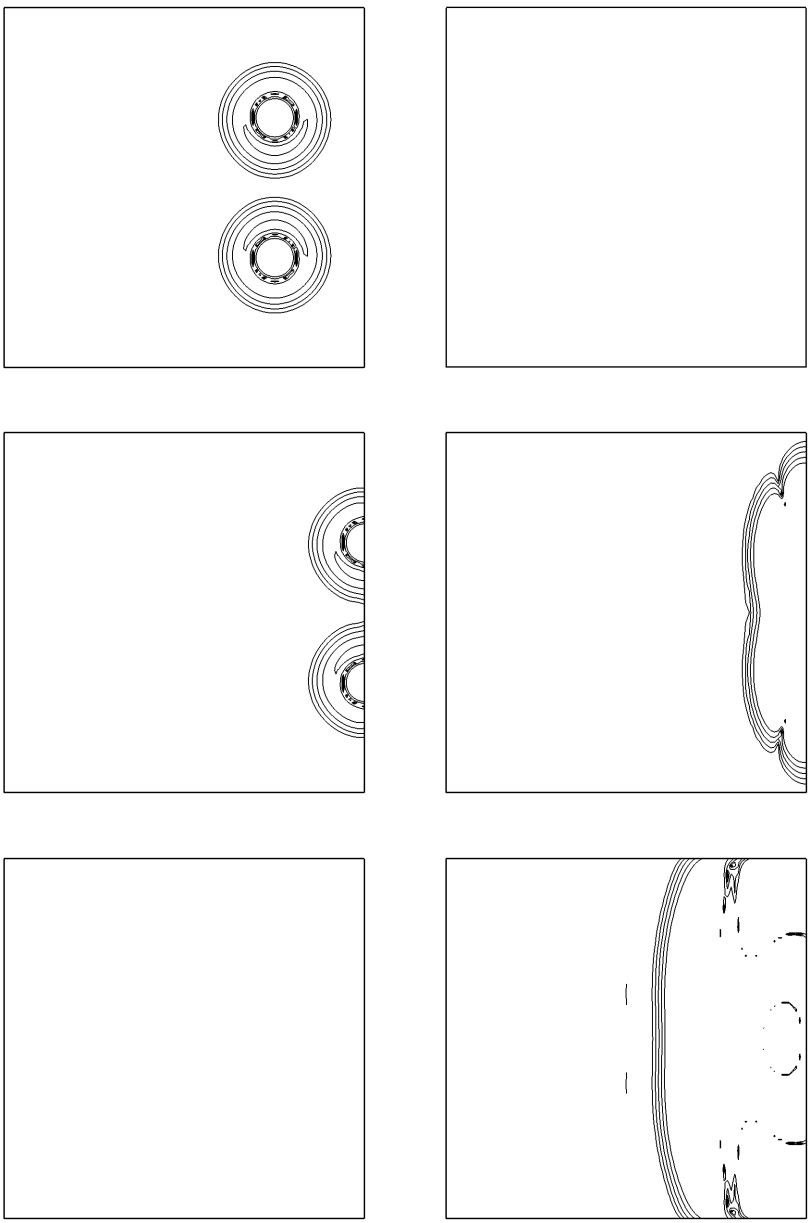

Figure 4.4: Vorticity magnitude $|\omega_3| = |\partial u_2'/\partial x_1 - \partial u_1'/\partial x_2|$ (left) and pressure amplitude $|p'|$ (right) for times $t = 50$, 100 and 150. Iso-contours: vorticity from 5×10^{-4} to 80×10^{-4} and pressure from 5×10^{-6} to 80×10^{-6} using 5 levels with a geometrical ratio of 2.

Chapter 5

Kirchhoff-Helmholtz Method

Kirchhoff-Helmholtz integration [27] is a method to predict a state variable governed by the wave equation at a point, based on information of the state variable from a closed surface enclosing all generating structures. In aeroacoustics, this is used to predict the pressure disturbances outside of the computational domain for the flow field. Given here is a short presentation of the Kirchhoff-Helmholtz method. For a more detailed analysis, see [27, 28].

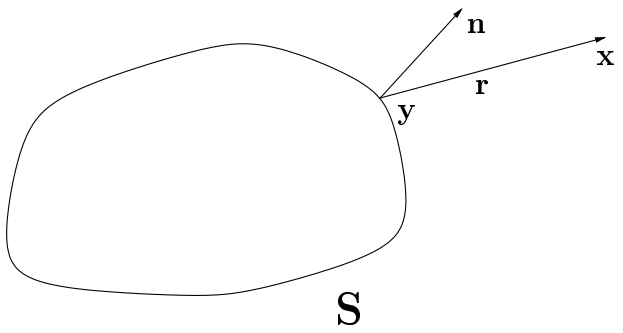

Figure 5.1: Closed Kirchhoff-Hemholtz surface, **S**, with outward pointing normal **n**. **y** point on surface **S** and observation point **x**. Surface **S** encloses all generating structures

A Kirchhoff-Helmholtz surface S is assumed to enclose all non-linear effects and sound sources. Outside this surface the field is linear and is governed by the wave equation. Let Φ be a quantity satisfying the wave equation, e.g. pressure, in the exterior of surface S.

$$\frac{1}{c_0^2}\frac{\partial^2\Phi}{\partial t^2} - \nabla^2\Phi = 0 \tag{5.1}$$

Φ and its first derivatives, $\partial\Phi/\partial t$, $\partial\Phi/\partial n$, must be continuous outside the surface S. c_0 is the speed of sound at ambient conditions. Using a Green function it is possible to derive an expression for the solution of equation 5.1 in terms of Φ and its derivatives on the boundary surface. The Green function G is a solution to the equation

$$\frac{1}{c_0^2}\frac{\partial^2 G}{\partial t^2} - \nabla^2 G = \delta(x-x', y-y', z-z') \tag{5.2}$$

where δ is the Dirac delta function. The observer position is denoted by $\mathbf{x} = (x, y, z, t)$ and the source is $\mathbf{y} = (x', y', z', \tau')$. Since the equation is hyperbolic, the Green function must satisfy the causality condition

$$G = \frac{\partial G}{\partial t} = 0 \qquad \text{for} \qquad t < \tau' \tag{5.3}$$

The solution to equation 5.2 is

$$G = \frac{\delta(\tau' + \Delta t - t)}{4\pi r} \tag{5.4}$$

where r is the distance between the source and the observer. τ' is the retarded time, i.e. emission time and Δt is the time delay between the emission time τ at $\mathbf{y}$ and the time t of detection at $\mathbf{x}$.

$$t = \tau' + \Delta t = \tau' + \frac{r}{c_0} \tag{5.5}$$

The Kirchhoff formulation for a stationary control surface S, can be written as (Pierce [29])

$$\Phi(\mathbf{x}, t) = \frac{1}{4\pi}\int_S \left[\frac{\Phi}{r^2}\frac{\partial r}{\partial n} - \frac{1}{r}\frac{\partial\Phi}{\partial n} + \frac{1}{c_0 r}\frac{\partial r}{\partial n}\frac{\partial\Phi}{\partial t}\right]_{\tau'} \mathrm{d}S \tag{5.6}$$

In the above equation $[]_{\tau'}$ stands for evaluation at the emission time. The normal derivative of the distance between the surface and the observer, $\partial r/\partial n$, is actually $\cos(\theta)$, where θ is the angle between the vector

$\mathbf{r} = \mathbf{x} - \mathbf{y}$ and the outward pointing normal vector $\mathbf{n}$. Equation 5.6 gives Φ at an arbitrary point $\mathbf{x}$ at time t outside of the control surface S as a function of the information given at $\mathbf{y}$ on the surface S at time τ'.

The method of Kirchhoff-Helmholtz integration relies formally on the use of a closed surface enclosing all sound sources on which the integration is performed. In a real jet case however, it is not feasible to extend the computational domain in the axial direction to ensure that all sound generating structures are inside a closed surface, see figure 5.2. There is always a portion of the downstream boundary through which a considerable amount of vorticity is convected. To minimize the error in the Kirchhoff-Helmholtz integration, the integration surface is left open on this boundary. This is a violation of the conditions under which the theory holds, however, Freund *et al.* [28] have shown that the major contribution to the solution at an observation point comes from a point on the surface that intersects a line between the observer and the source point, see figure 5.2. The errors involved using the open surface is smaller than what would have been the case if the surface would have crossed the outflow region.

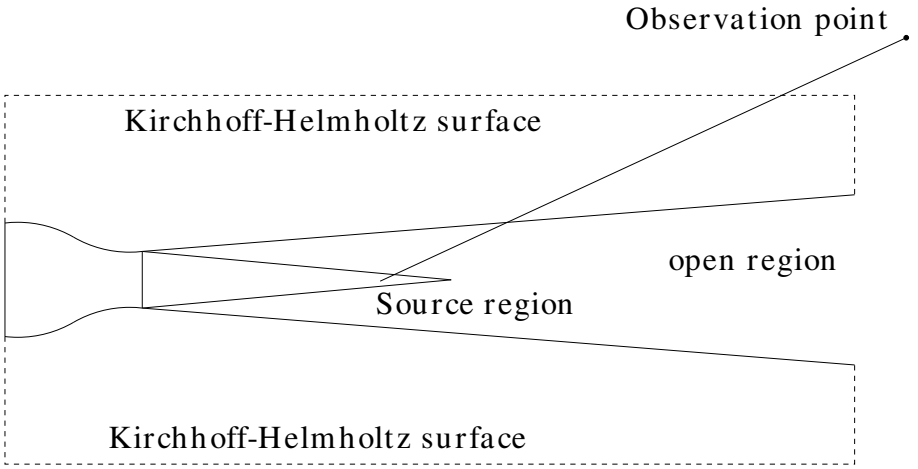

Figure 5.2: Kirchhoff-Helmholtz surface for jet case. - - - : Kirchhoff-Helmholtz surface.

The Kirchhoff-Helmholtz integral method to extend the acoustic signal outside of the computational domain has been applied to a monopole test case, see Billson [30]. Using a closed Kirchhoff surface the results were in excellent agreement with the analytical solution.

Chapter 6

Modified Linearized Euler Equations

The linearized Euler equations are known to be unstable for some flows. Free shear flows with mixing layers are typical flows when this can occur. The coupling between the different types of characteristic variables in these flows seems to be the reason for this phenomenon. The solution to the linearized Euler equations can be split into two parts. One is the particular solution given by the existence of source terms in the system of equations. The other is the homogeneous solution to the equations when there are no source terms. The equations can be unstable if the homogeneous solution have growing modes. Since the equations are linear there is no limit to the amplitude of such disturbances as long as they are still in the computational domain. In many cases the amplitude of the homogeneous solution is bounded by the fact that the solution is convected out of the computational domain. The problem is that the sought solution (the particular solution) can be masked by the homogeneous solution so that is is impossible to draw any conclusions from the computations. In extreme cases numerical problems could arise due to cancellation errors in the numerical representation in the computer. But since the equations are linear the two solutions are independent of each other and a modification of one does not affect the other.

In an attempt to resolve these problems, modified linearized Euler equations are developed. The aim is to make the resulting equations stable in free shear flows without loosing too much of the physics held in the original equations. The method used here is simply to discard the spatial derivatives of the reference solution in the linearized Euler equations. The resulting equations in compact conservative form are

$$\frac{\partial Q'}{\partial t} + A_0 \frac{\partial Q'}{\partial x} + B_0 \frac{\partial Q'}{\partial y} + C_0 \frac{\partial Q'}{\partial z} = 0 \tag{6.1}$$

where the following terms have been neglected

$$\left[\frac{\partial A_0}{\partial x} + \frac{\partial B_0}{\partial y} + \frac{\partial C_0}{\partial z} \right] Q' \tag{6.2}$$

The neglected terms in the modified equations contain the spatial gradients of the reference solution. The resulting equations are equal to the full linearized Euler equations only for a homogeneous reference solution in which the characteristic variables are decoupled. The modified equations have a much weaker coupling between different characteristic variables and are therefore more stable in shear flows than the original equations. This is shown in figure 6.1 where planar acoustic waves are generated inside the nozzle of a Mach 0.9 low Reynolds number jet. The resulting sound field is represented by the axial acoustic intensity $p'u''$.

The full linearized Euler equations are used for the result in figure 6.1(a) and the modified in figure 6.1(b). In both cases the sound waves exit the nozzle and are refracted out of the core region due to the mean flow. If there was no interaction between different types of disturbances, these would be the only disturbances in the solutions. In figure 6.1(a) however, the sound waves excite vorticity waves which in turn are amplified by the mean shear as they are convected downstream. These are seen as the disturbances in the centerline region. The strong excitation of vorticity waves in figure 6.1(a) are not present in figure 6.1(b). There are some disturbances in the centerline region which are clearly not acoustical but the level is much lower than in figure 6.1(a).

The modified equations are clearly more stable than the full linearized Euler equations as disturbances are not amplified in the presence of mean shear. There are however other differences in the solutions from the different sets of equations. The refraction of the acoustic waves is not the same in figures 6.1(b) and 6.1(a). There is a much larger intensity in the waves upstream of the nozzle using the modified equations than the full equations indicating that the modified equations do not give the correct refraction in the nozzle exit.

Figures 6.2 show the pressure disturbances caused by a monopole located in the shear layer of the same Mach 0.9 jet as before. From the solutions in figures 6.2 there is a clear difference in the directivity

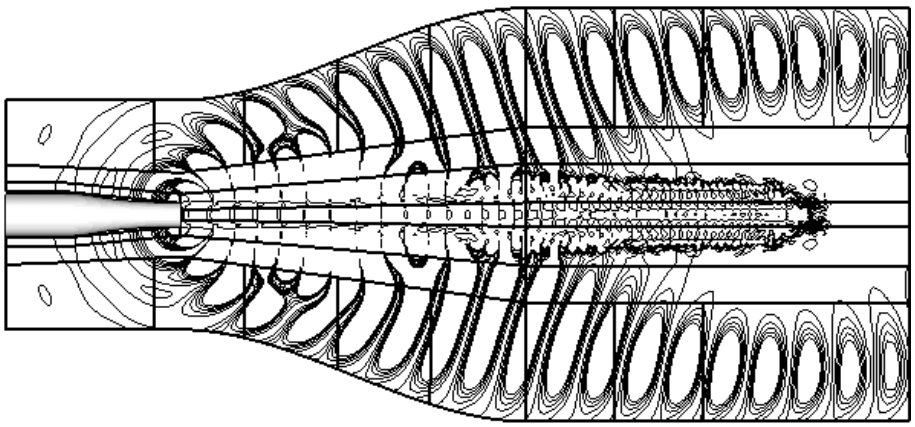

(a) Full linearized Euler equations

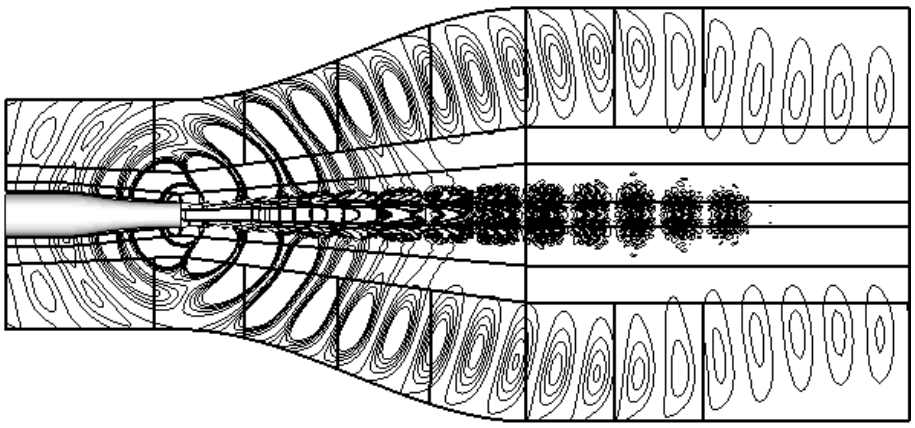

(b) Modified linearized Euler equations

Figure 6.1: Axial acoustic intensity $p'u''$ from plane acoustic waves generated in the nozzle.

of the sound field. This shows that the refraction of the sound generated from a monopole is not the same for the two sets of equations. The conclusion must be that the neglection of the mean shear terms as described above affect the sound propagation in a non-physical way. The modified equations are more stable which is positive but they seem to lack some of the directional effects.

A continued study is necessary in this area to see if there are alternative stabilizing modifications of the linearized Euler equations that can be made which have less severe effects on the solution.

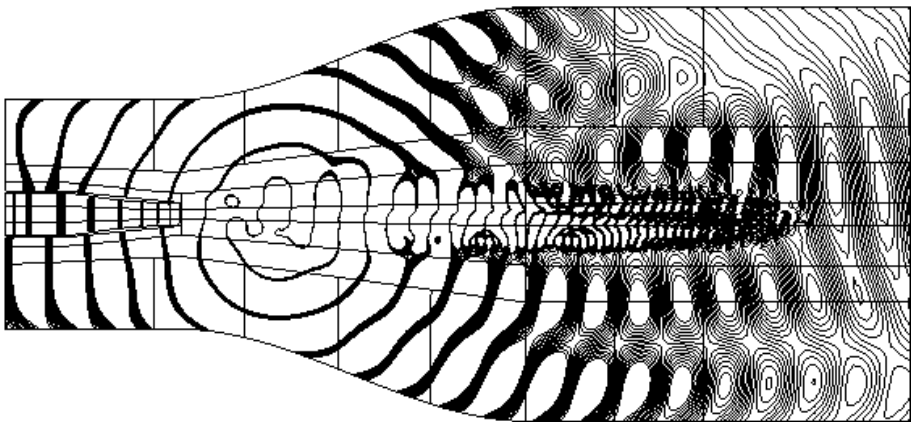

(a)

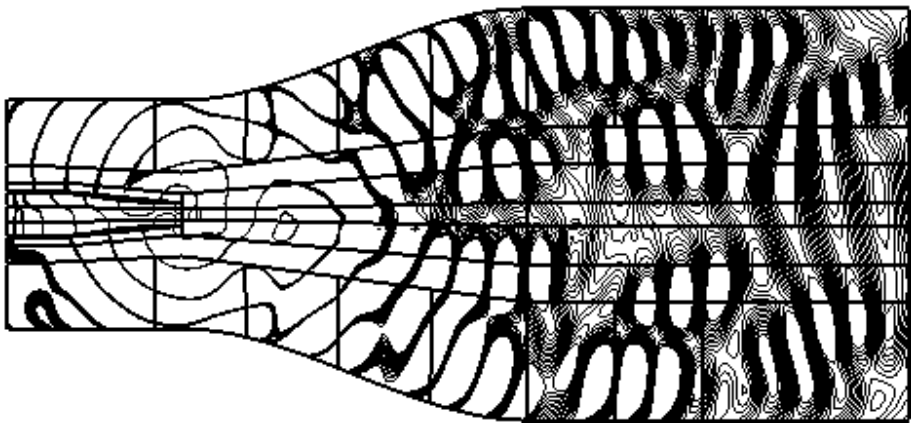

(b)

Figure 6.2: Pressure disturbances in Ox_1x_3 plane from monopole located at $(x_0, y_0, z_0) = (8r_0, 0, 1.5r_0)$

Chapter 7

Acoustic Scattering of Cylinder - Benchmark Test Case

7.1 Introduction

This chapter concerns a benchmark test case for the linearized Euler equations in two dimensions. The Benchmark problem is called *Acoustic scattering of a cylinder*. The problem was one of many in the Second Computational Aeroacoustic (CAA) Workshop on Benchmark Problems in November 1996, [31].

In this test case the effects of different numerical schemes, grid resolution, time step and artificial numerical dissipation of high wave numbers are evaluated.

7.2 Problem Description

The physical problem is to find the sound field generated by a propeller and scattered off by the fuselage of an aircraft. Computationally, this is a good problem for testing wall boundary conditions and diffraction. In this work the problem is also used to test numerical schemes, required grid resolution and time step and the effect of artificial dissipation.

The fuselage is idealized as a circular cylinder and the noise source (propeller) as a distributed line source, see figure 7.1. In this way, the problem can be solved in two dimensions. The problem is given in polar coordinates and is non-dimensionalized with the variables in table 7.1.

The equations to be solved are the linearized Euler equations. For

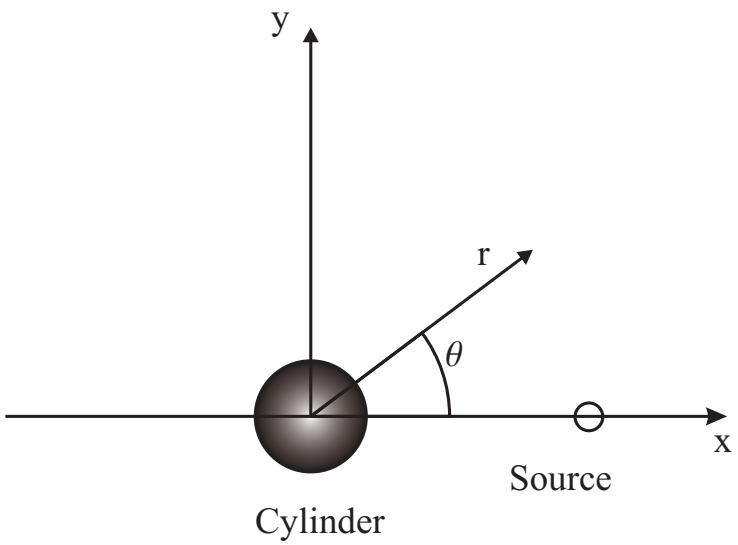

Figure 7.1:

length scale	=	diameter of circular cylinder, D
velocity scale	=	speed of sound, c
time scale	=	D/c
density scale	=	undisturbed density ρ_0
pressure scale	=	$\rho_0 c^2$

Table 7.1:

this problem, with zero convection and only isentropic acoustic disturbances, the linearized Euler equations can be written as

$$\frac{\partial p}{\partial t} + \frac{\partial u}{\partial x} + \frac{\partial v}{\partial y} = S(x,y,t) \tag{7.1}$$

$$\frac{\partial u}{\partial t} + \frac{\partial p}{\partial x} = 0 \tag{7.2}$$

$$\frac{\partial v}{\partial t} + \frac{\partial p}{\partial y} = 0 \tag{7.3}$$

where $S(x,y,t)$ represents the noise source explicitly implemented as

$$S(x,y,t) = \exp\left[-\ln 2\left(\frac{(x-x_s)^2 + y^2}{w^2}\right)\right]\sin\omega t \tag{7.4}$$

where $x_s = 4$, $w = 0.2$, $\omega = 8\pi$. To evaluate the quality of the solution a property called the directivity, $D(\theta) = \lim_{r\to\infty} r\overline{p^2}$, should be computed for $\theta = 90°$ to $180°$ at $\Delta\theta = 1°$ and compared with the analytical solution, see figure 7.1. The angular frequency of the source is $\omega = 8\pi$. The grid specification and Δt was also to be stated.

7.3 Analytical Solution

Start with the linearized Euler equations, equations 7.2 - 7.4. The boundary conditions are

1. zero-normal-velocity at the surface of the cylinder

$$\mathbf{v} \cdot \mathbf{n} = 0 \quad \text{at} \quad x^2 + y^2 = (0.5)^2$$

2. radiation boundary condition for $x, y \to \infty$.

By eliminating u and v from equations 7.2 to 7.1 and separating the pressure into $p_i(x, y)$ and $p_r(x, y)$ it is possible to derive an analytical solution for the pressure at any point. Here $p_i(x, y)$ is the incident wave generated by the source and $p_r(x, y)$ is the wave reflected off the cylinder. The solution is then given in the form

$$p(x, y, t) = \mathrm{Im}(\hat{p}(x, y) \exp(-i\omega t)) \tag{7.5}$$

where

$$\hat{p}(x, y) = p_i(x, y) + p_r(x, y) \tag{7.6}$$

The solution for $p_i(x, y)$ is given by

$$p_i(r_s) = \int_0^\infty G(r_s, \xi)[-i\omega \exp(-b\xi^2)]d\xi \tag{7.7}$$

where

$$G(r_s, \xi) = \begin{cases} -\frac{\pi i}{2}\xi J_0(\omega r_s)H_0^{(1)}(\omega\xi), & 0 \le r_s \le \xi \\ -\frac{\pi i}{2}\xi J_0(\omega\xi)H_0^{(1)}(\omega r_s), & \xi \le r_s \le \infty \end{cases} \tag{7.8}$$

where J_0 and $H_0^{(1)}$ are the zeroth-order Bessel and Hankel functions respectively. r_s is the radius with origin at $x = x_s$, $y = 0$. With the solution for $p_i(r_s)$ found, the solution for $p_r(r, \theta)$ is represented by Fourier series

$$p_r(r,\theta) = \sum_{k=0}^{\infty} C_k H_k^{(1)}(r\omega)\cos(k\theta) \tag{7.9}$$

where $H_k^{(1)}$ is the Hankel function of the first kind. The radius r is computed from the center of the cylinder. The coefficients C_k in equation 7.9 are given by

$$C_k = \frac{\epsilon_k}{\pi\omega[\frac{2k}{\omega}H_k^{(1)}(\omega/2) - H_{k+1}^{(1)}(\omega/2)]}\int_0^{\pi} B(\theta)\cos(k\theta)d\theta \tag{7.10}$$

Here $\epsilon_0 = 1,\ \epsilon_k = 2,\ k = 1, 2, \ldots$, and $B(\theta)$ is given by

$$B(\theta) = -\frac{\partial p_i}{\partial n} \text{ at } x^2 + y^2 = 0.25 \tag{7.11}$$

Inserting the solutions for $p_i(r_s)$ and $p_r(r, \theta)$ from equations 7.7 to 7.11 into equations 7.6 and 7.5 gives the analytical solution for the pressure. The directivity,

$$D(\theta) = r\overline{p^2} \tag{7.12}$$

can then be computed for any value of the radius r.

7.4 Numerical Method

The numerical code is a 2D version of the code described in Chapter 3. The solver is applied on a multi-block structured Cartesian boundary-fitted grid. The numerical schemes used in this problem are the 4:th order Dispersion Relation Preserving (DRP) scheme by Tam and Webb [15] and a regular 4:th order numerical scheme. Selective artificial damping is applied through the fluxes to attenuate spurious waves arising due to the discretization of the equations. This artificial damping leaves waves with low wave numbers unaffected while high wavenumber waves are effectively attenuated. The time stepping algorithm is a 4:th order four stage Runge Kutta time marching technique.

7.5 Numerical Issues

A number of numerical issues will be addressed. These are

1. The capability of the DRP scheme to predict acoustic waves for different configurations.

2. Required grid resolution for accurate predictions.

3. Required time step for accurate predictions

4. Allowable amount of artificial selective damping.

7.6 Boundary Conditions

Two sets of boundary conditions were employed in this study. These are

1. Characteristic variable based absorbing boundary conditions

2. Perfectly Matched Layer (PML) by Hayder *et al.* [32].

The Cvba boundary conditions were used as initial test boundary conditions. They absorb most of the outgoing waves although the reflected part is unacceptable especially at high angle of incidence [30].

The PML boundary condition is a highly absorbing boundary condition which can handle many types of linearized Euler based problems and has been applied to a number of cases [32], [33]. The full description of the PML can be found in [32] but a short description can be appropriate here.

The PML is based on the idea that computational domain is surrounded by a buffer layer of about 20 extra cells. In this buffer layer the governing equations are modified with damping terms so that in every time step the solution will tend towards an ambient solution. The PML is the region outside the thick lines in figure 7.2. In this way the outgoing waves will be attenuated on their way to the outer

boundary and hopefully vanish before they reach the boundary. To improve the performance of the PML, the mesh is stretched in the PML layer. In this way the numerical scheme, due to numerical dissipation, helps to attenuate outgoing waves.

7.7 Computational grid

The grid is a boundary fitted structured grid with 520×491 cells in the x and y directions. The computational domain covers $-10 \leq x \leq 6$ in the physical domain and $-11 \leq x \leq -10$ and $6 \leq x \leq 7$ in the PML in the x direction. In the y direction the physical domain covers $0 \leq y \leq 15$ and $15 \leq y \leq 16$ is PML. This results in an almost uniform cell size with a typical cell width of $\Delta x = 0.03125$, except in the region closest to the cylinder where an O-grid is used resulting in a cell width closest to the cylinder of $\Delta x = 0.015625$. With a wave length of $\lambda = 0.25$, the resolution in the problem is 8 points per wavelength or more. The mesh is depicted in figure 7.2.

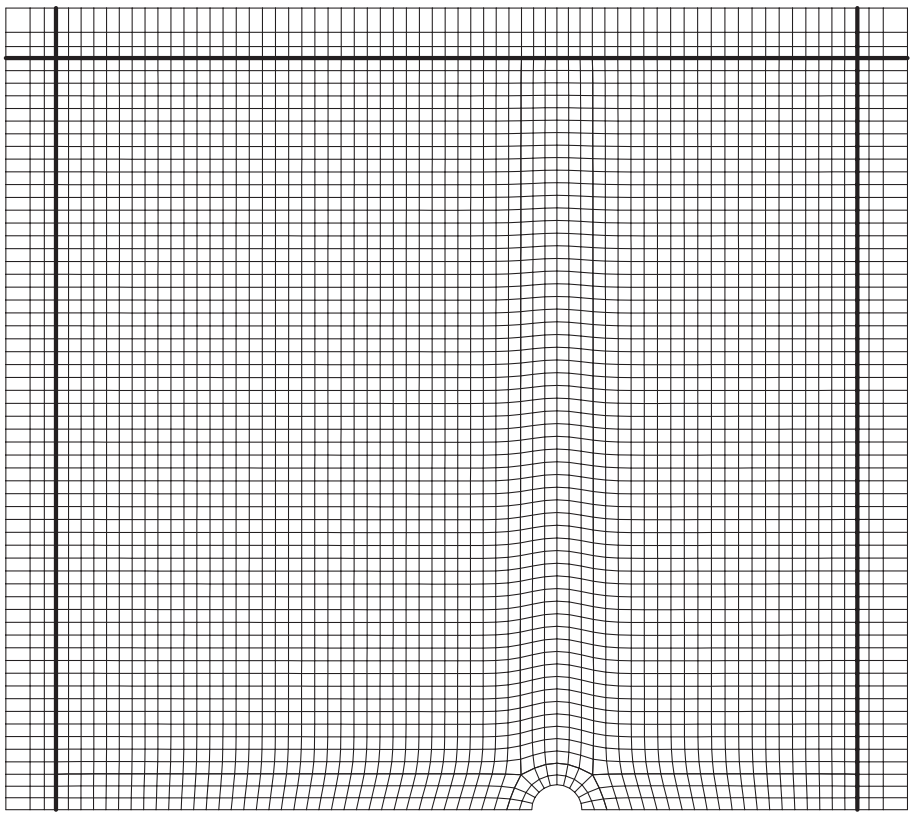

Figure 7.2: Computational mesh. Every fourth grid line is shown.

7.8 Results

The following setup resulted in quite satisfactory results.

Scheme	=	4:th order DRP scheme
Time marching	=	four stage 4:th order Runge Kutta
Boundary condition	=	PML
Grid resolution	=	0.03125 (8 points per wavelength)
Time step	=	0.00342 ($\mathrm{CFL} = 0.1$)
damping coefficient	=	0.001

Table 7.2: Case 1

The instantaneous solution of the pressure disturbance can be seen in figure 7.3. The predicted directivity $D(\theta)$ is compared to the analytical solution in figure 7.4(a). It is seen that the numerical solution is quite good. The relative phase velocity and amplitude error (see Appendix 11.2) for the case can be seen in figure 7.5(a) and 7.5(b). The vertical dashed line in the figures show the value of $k\Delta x$ of the wave emitted from the noise source. As seen in figure 7.5(a) the value of $k\Delta x$ is well within the region where the phase velocity is well predicted. In the figure showing the amplitude error however the value of $k\Delta x$ is very close to where the numerical scheme would attenuate the solution.

In the following one parameter is changed in each case. The parameters changed are spatial resolution, numerical scheme, boundary condition, time step and amount of artificial damping. The setup for each case is shown in table 7.3.

Case	Scheme	Resolution	Time step	B.C.	Damp. coeff
1	DRP	0.03125	0.00342	PML	0.001
2	DRP	**0.04166**	0.00342	PML	0.001
3	**4:th order**	0.03125	0.00342	PML	0.001
4	DRP	0.03125	0.00342	**Cvba**	0.001
5	DRP	0.03125	**0.01026**	PML	0.001
6	DRP	0.03125	**0.01708**	PML	0.001
7	DRP	0.03125	0.00342	PML	**0.002**
8	DRP	0.03125	0.00342	PML	**0.003**

Table 7.3: Cases. The **bold** text shows which parameter is changed in each case

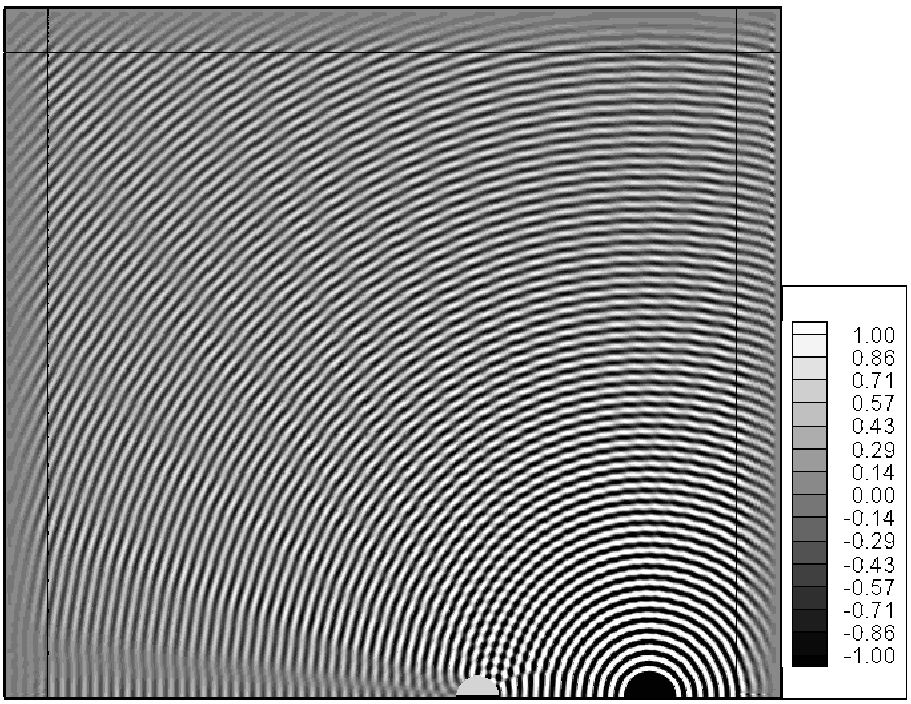

Figure 7.3: Instantaneous solution of pressure, Case 1

A resolution of 8 points per wavelength seems to give good results for the DRP numerical scheme. To see if it is possible to decrease the number of points per wavelength the same problem is computed with 6 points per wavelength (Case 2). The time step is kept at $\Delta t = 0.00342$ with a resulting $\mathrm{CFL} = 0.08$ and the other parameters are kept the same as shown in table 7.2. The result is evident in figure 7.4(b), showing the directivity for this case. There is a clear increase in damping of the directivity curve compared to the first case implying that the numerical dissipation is larger. This is confirmed by the slight amplitude error in figure 7.6(b).

A standard 4:th order numerical scheme is also tested on the same problem (Case 3). All other parameters are the same as in the first case, see table 7.2. The effect of this is drastic. The directivity suffers from numerical dispersion. This is seen as a shift in the peaks in figure 7.4(c). More evidence of this can be seen in figure 7.7(a) showing the relative phase velocity (dispersion relation) of the full discretization of this case. At 8 points per wavelength there is a small error in the dispersion relation for the standard 4:th order numerical scheme.

As mentioned above, the characteristic variable based absorbing boun-

dary condition (Cvba) was initially used in this benchmark problem. The solution in this case is not satisfactory (Case 4). The computational domain is full of reflected waves and the resulting directivity curve are erroneous, see figure 7.4(d).

To see the effect of the CFL-number on the solution the time step is increased to $\Delta t = 0.01026$ and $\Delta t = 0.01708$ equivalent of $\mathrm{CFL} = 0.3$ and $\mathrm{CFL} = 0.5$ respectively (Case 5 & 6). The resulting directivity is shown in figure 7.8(b) and 7.8(a). There is a slight increase in the deviation of the numerical result from the analytic due to damping compared to the first case. The effect is very small however. This is also supported by figures 7.9(b) and 7.10(b) showing that the amplitude errors are very small for these cases.

Finally the amount of artificial numerical dissipation is tested (Case 7 & 8). The value of the damping coefficient ϵ is increased to 0.002 and 0.003 respectively. The directivity curves for these cases are shown in figures 7.8(c) and 7.8(d). The damping is more prominent when ϵ is increased. Not only is the damping increased for high wave numbers, but the range of wave numbers for which damping is large also increases. The effect is slight for this test case but the effect is shown in figures 7.11(b) and 7.11(b).

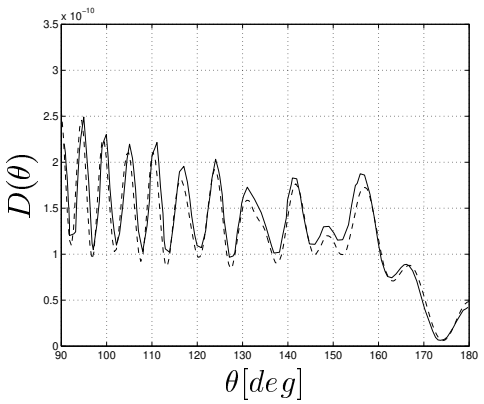

(a) Case 1, **Baseline case as in table** 7.2

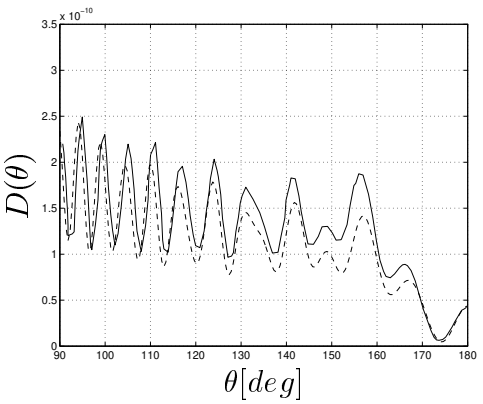

(b) Case 2, **6 points per wavelength**

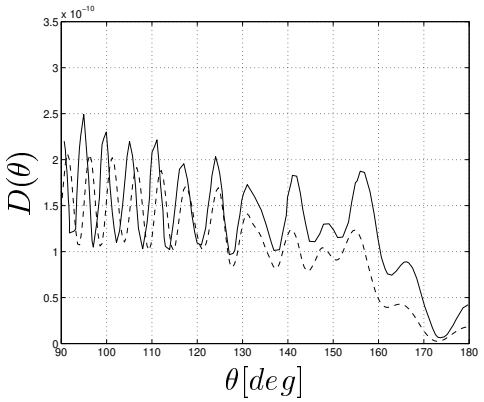

(c) Case 3, **4:th order discretization**

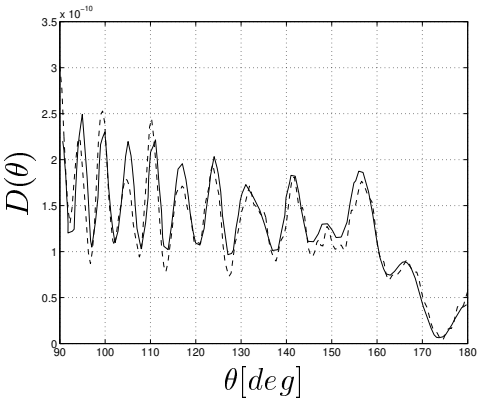

(d) Case 4, **Cvba boundary condition**

Figure 7.4: Directivity computed at radius $r = 7$. Cases 1 to 4, see table 7.3. Solid line: analytical, dashed line: numerical

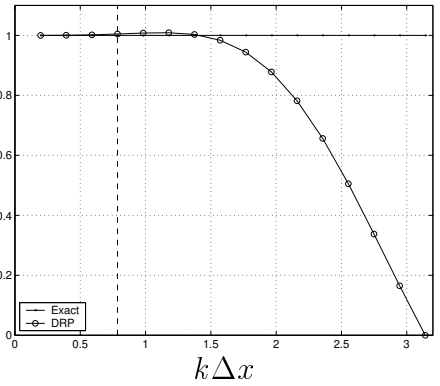

(a) **Relative phase velocity**

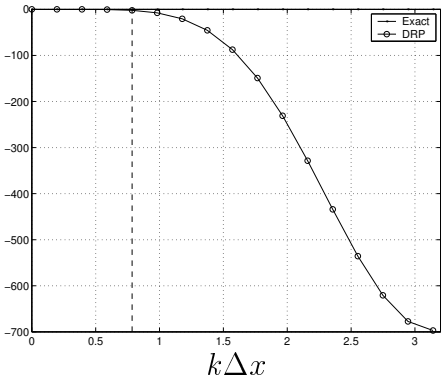

(b) **Amplitude error**

Figure 7.5: Case 1 & 4. Dashed line: $k\Delta x$ equivalent to 8 points per wavelength

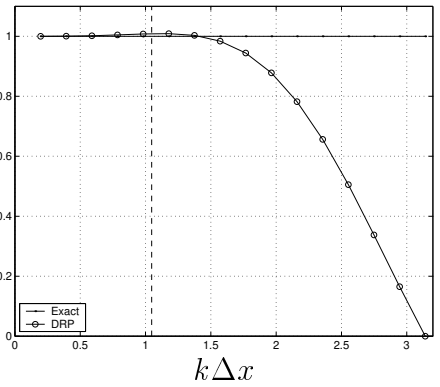

(a) **Relative phase velocity**

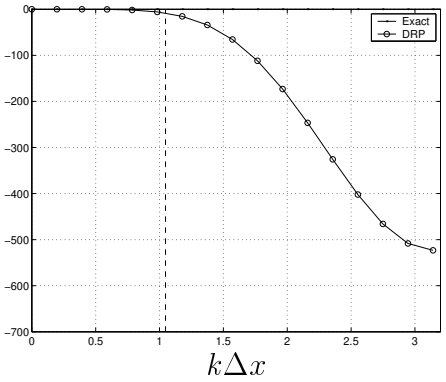

(b) **Amplitude error**

Figure 7.6: Case 2. 6 points per wavelength. Dashed line: $k\Delta x$ equivalent to 6 points per wavelength

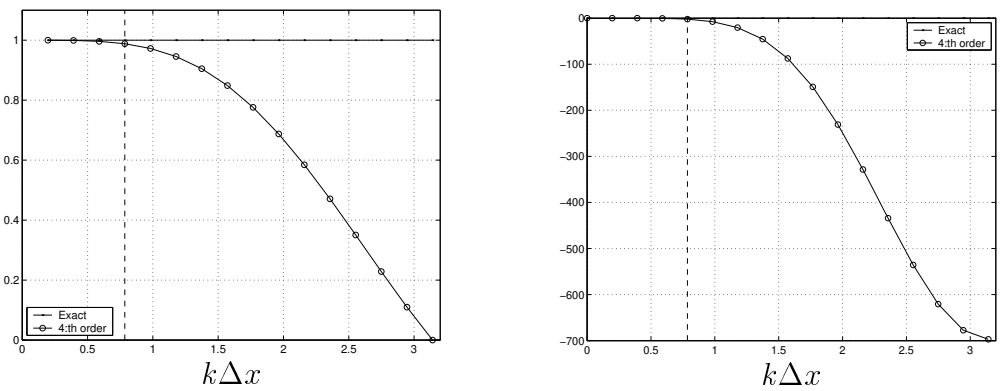

(a) **Relative phase velocity** (b) **Amplitude error**

Figure 7.7: Case 3. 4:th order discretization. Dashed line: $k\Delta x$ equivalent to 8 points per wavelength

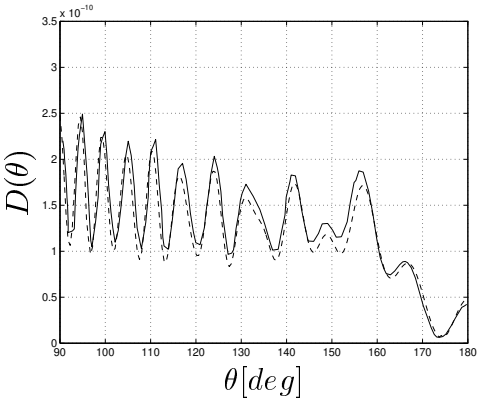

(a) Case 5, $\Delta \mathbf{t} = \mathbf{0.01026}$

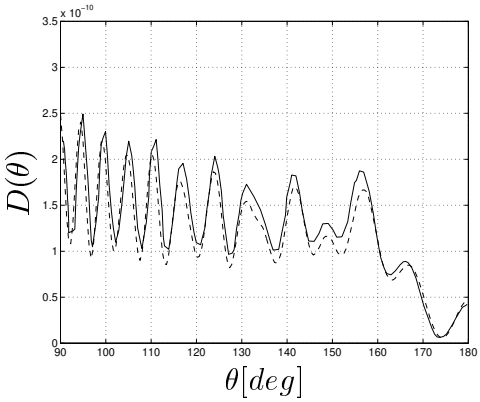

(b) Case 6, $\Delta \mathbf{t} = \mathbf{0.01708}$

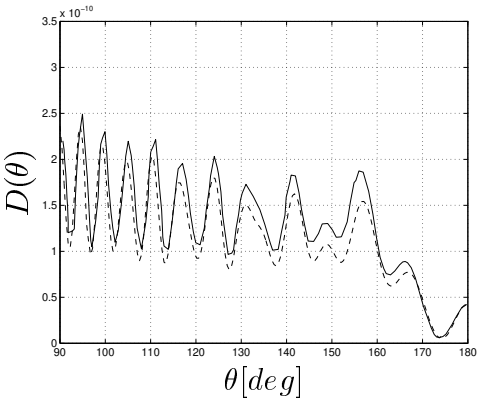

(c) Case 7, $\epsilon = \mathbf{0.002}$

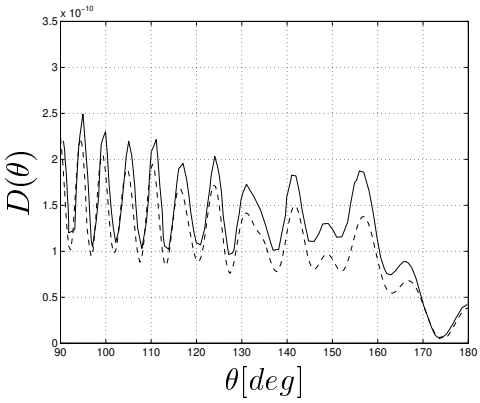

(d) Case 8, $\epsilon = \mathbf{0.003}$

Figure 7.8: Directivity computed ar radius $r = 7$. Cases 5 to 8, see table 7.3. Solid line: analytical, dashed line: numerical

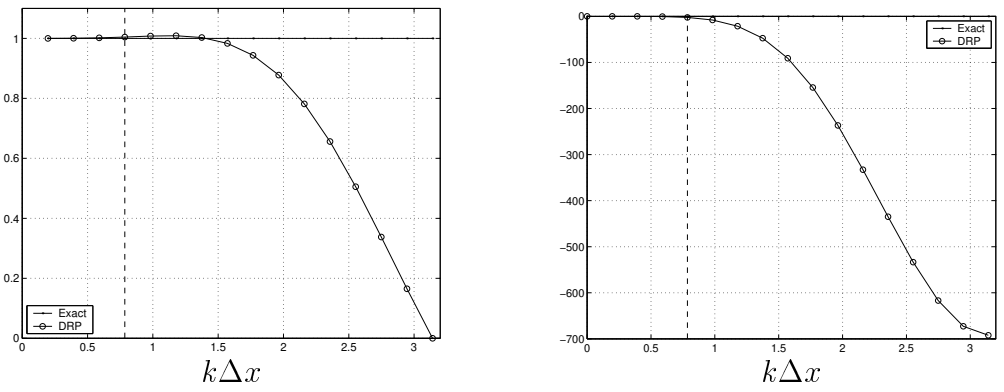

(a) **Relative phase velocity** (b) **Amplitude error**

Figure 7.9: Case 5. $\Delta t = 0.01026$. Dashed line: $k\Delta x$ equivalent to 8 points per wavelength

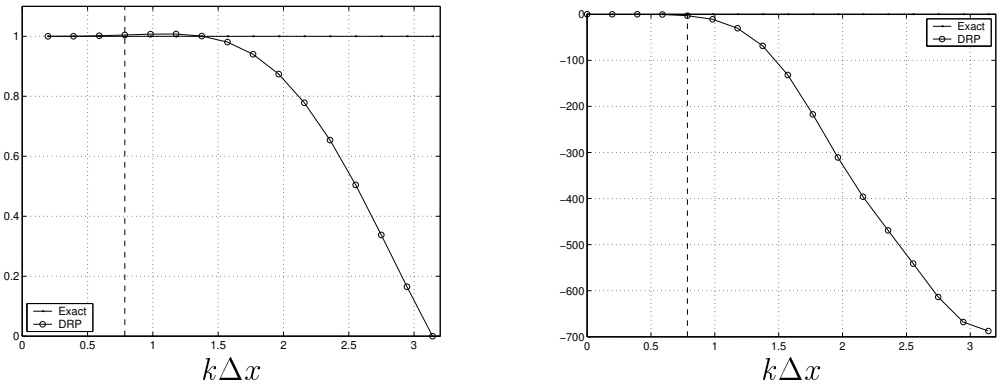

(a) **Relative phase velocity** (b) **Amplitude error**

Figure 7.10: Case 6. $\Delta t = 0.01708$. Dashed line: $k\Delta x$ equivalent to 8 points per wavelength

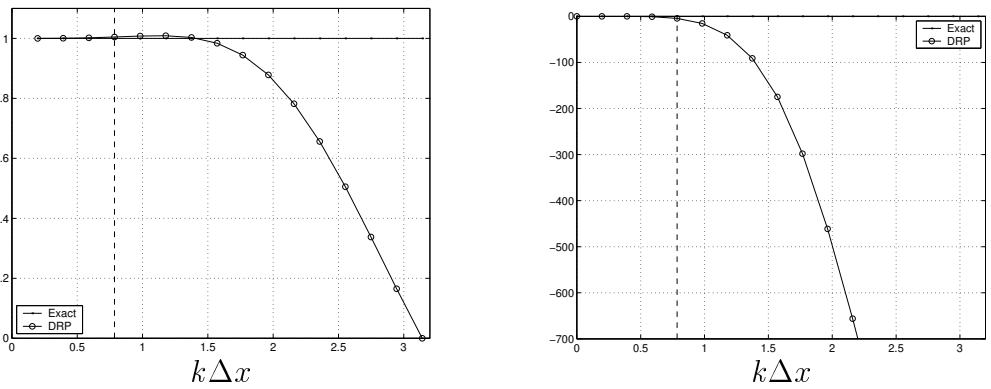

(a) **Relative phase velocity** (b) **Amplitude error**

Figure 7.11: Case 7. $\epsilon = 0.002$. Dashed line: $k\Delta x$ equivalent to 8 points per wavelength

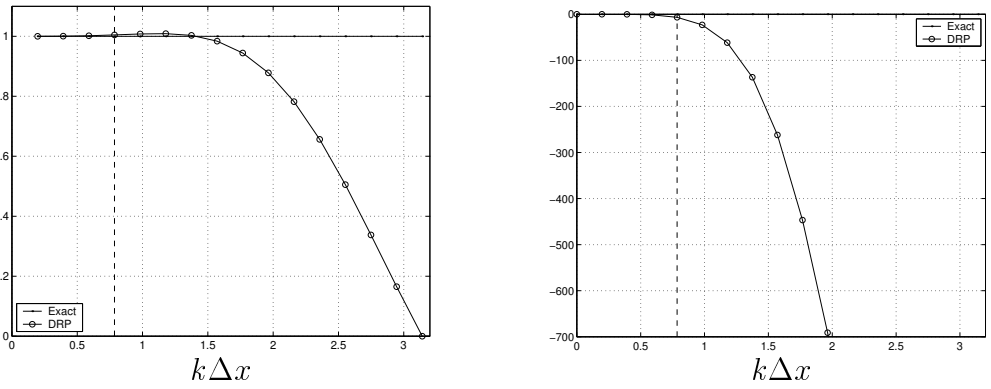

(a) **Relative phase velocity** (b) **Amplitude error**

Figure 7.12: Case 8. $\epsilon = 0.003$. Dashed line: $k\Delta x$ equivalent to 8 points per wavelength

Chapter 8

Acoustic Source Terms for The Linear Euler Equations on Conservative Form

8.1 Introduction

Using a Navier-Stokes solver for the near-field combined with an acoustic analogy for the far-field is quite common in aeroacoustics. There are a variety of analogies which could be used, Lighthill's [1] analogy for free turbulence in a homogeneous medium, Lilley's analogy [6], Curle's [3] extension to Lighthill's analogy for the presence of solid walls just to mention a few. Lighthill's analogy is most often solved as an integral solution and limited by the assumption of sound generation and radiation in a homogeneous medium and the same holds for Curle's extension to Lighthill's analogy. Although Lilley's analogy does include refractional effects it is somewhat sensitive to the way the source terms are evaluated [34]. The linear Euler equations with source terms are not limited by the homogeneous medium assumption and can handle refractional effects and reflection at solid boundaries. The scalar wave equation governs acoustic wave propagation but not entropy and vorticity waves. The linear Euler equations on the other hand govern both acoustic propagation as well as entropy and vorticity waves.

This work is a part of the evaluation and development of the SNGR (Stochastic Noise Generation and Radiation) method originally presented by Bechara *et al.* [9] and further developed by Bailly and Juvé [10]. The present work focus on the formulation of source terms for the linear Euler equations. Bailly and Juvé [10] use a formulation of

the linear Euler equations based on $(\rho', \overline{\rho}u', \overline{\rho}v', \overline{\rho}w', p')$ as solution variables. In that formulation, the source terms only enter the momentum equations. The formulation of the linear Euler equations used in the present work is entirely based on the conservative variables, $(\rho', (\rho u)', (\rho v)', (\rho w)', (\rho e_0)')$. In this formulation the source terms enter not only the momentum equations but also the energy equation. The correct formulation of the source terms for the linear Euler equations on conservative form are derived below. It is shown that the source terms not only depend on the unsteady Reynolds stresses but also on unsteady total enthalpy. This causes some problems in the SNGR method. In the present formulation of the SNGR [10], only velocity fluctuations are modeled, assuming that all other variables are constant. For this reason different simplifications of the source terms are derived.

The use of a forced 2D mixing layer as a test case for different methods of sound prediction was first presented by Colonius [34]. Colonius performed a direct numerical simulation of a free mixing layer forced at its first three harmonics. The results were used and compared with Lilley's acoustic analogy[6]. Later Bogey [35] made a sound prediction with LES and Lighthill's analogy on a free mixing layer excited by the first two harmonics. The results were in both cases in good agreement between the direct simulations and the analogies. To validate the derived source terms a forced mixing layer is computed by direct simulation using a 2D compressible Navier-Stokes solver. The solution from the direct simulation provides a reference solution (time average) and is used to evaluate the source terms for the linear Euler equations which are solved and the results are compared. Comparisons of the computational results using the different source terms with direct simulation of a forced free mixing layer are presented and discussed.

8.2 Theory

In this section a derivation of the linearized Euler equations and energy equation on conservative form with source terms is presented. The derivation starts with the Euler equations and is a rewriting of the full Euler equations in a way that the left-hand side of the equations are the linear Euler equations. The remaining non-linear terms in this derivation are put in the right-hand side and form the source terms.

Start with the compressible Euler equations on conservative form.

$$\frac{\partial \rho}{\partial t} + \frac{\partial \rho u_j}{\partial x_j} = 0 \tag{8.1}$$

$$\frac{\partial \rho u_i}{\partial t} + \frac{\partial}{\partial x_j}(\rho u_i u_j + p\delta_{ij}) = 0 \tag{8.2}$$

$$\frac{\partial \rho e_0}{\partial t} + \frac{\partial}{\partial x_j}(\rho h_0 u_j) = 0 \tag{8.3}$$

where $(\rho, \rho u, \rho v, \rho w, \rho e_0)$ are the density, the x, y and z momentum and total internal energy per unit volume; ρh_0 is the total enthalpy per unit volume. Introducing a decomposition of the variables in a time averaged part and a fluctuating part as

$$\begin{aligned} \rho &= \overline{\rho} + \rho' \\ u_i &= \widetilde{u}_i + u_i'' \\ p &= \overline{p} + p' \\ e_0 &= \widetilde{e}_0 + e_0'' \\ h_0 &= \widetilde{h}_0 + h_0'' \end{aligned} \tag{8.4}$$

where bar denotes time averaged and prime fluctuating variable. The average of for example u_i is a Favre time average defined by

$$\widetilde{u}_i = \frac{\overline{\rho u_i}}{\overline{\rho}} \tag{8.5}$$

and the double prime is the fluctuation associated with the Favre time averaged velocity.

The momentum can be decomposed in two ways

$$\begin{aligned} &\rho u_i = \overline{\rho u_i} + (\rho u_i)' = \overline{\rho}\widetilde{u}_i + (\rho u_i)' \quad \text{or} \\ &\rho u_i = \rho(\widetilde{u}_i + u_i'') = \rho\widetilde{u}_i + \rho u_i'' \end{aligned} \tag{8.6}$$

$$\Rightarrow (\rho u_i)' = \rho'\widetilde{u}_i + \rho u_i'' \tag{8.7}$$

The first decomposition in equation 8.6 is done by time averaging ρu_i and the second by Favre averaging u_i. Both are valid and will be used in the following derivation. Combined they give equation 8.7. The same holds for ρe_0 and ρh_0 which gives the following equalities

$$\begin{aligned}(\rho e_0)' &= \rho' \widetilde{e}_0 + \rho e_0'' \\ (\rho h_0)' &= \rho' \widetilde{h}_0 + \rho h_0''\end{aligned} \tag{8.8}$$

Furthermore

$$\begin{aligned}\rho h_0 u_j &= \rho(\widetilde{h}_0 + h_0'')(\widetilde{u}_j + u_j'') \\ &= \rho \widetilde{h}_0 \widetilde{u}_j + \rho \widetilde{h}_0 u_j'' + \rho h_0'' \widetilde{u}_j + \rho h_0'' u_j''\end{aligned} \tag{8.9}$$

$$\Rightarrow \overline{\rho h_0 u_j} = \overline{\rho} \widetilde{h}_0 \widetilde{u}_j + \overline{\rho h_0'' u_j''} \tag{8.10}$$

Taking the time average of the continuity equation 8.1 gives

$$\frac{\partial \overline{\rho}}{\partial t} + \frac{\partial \overline{\rho u_j}}{\partial x_j} = 0 \tag{8.11}$$

Subtraction of equation 8.11 from equation 8.1 results in the continuity equation for the fluctuations

$$\frac{\partial \rho'}{\partial t} + \frac{\partial (\rho u_j)'}{\partial x_j} = 0 \tag{8.12}$$

Averaging the inviscid momentum equation 8.2 gives

$$\frac{\partial \overline{\rho} \widetilde{u}_i}{\partial t} + \frac{\partial}{\partial x_j}(\overline{\rho} \widetilde{u}_i \widetilde{u}_j + \overline{\rho u_i'' u_j''} + \overline{p} \delta_{ij}) = 0 \tag{8.13}$$

and subtracting the resulting equation 8.13 from 8.2 gives an equation for the fluctuations

$$\begin{aligned}&\frac{\partial \rho u_i - \overline{\rho} \widetilde{u}_i}{\partial t} + \\ &\frac{\partial}{\partial x_j}(\rho u_i u_j - \overline{\rho} \widetilde{u}_i \widetilde{u}_j - \overline{\rho u_i'' u_j''} + (p - \overline{p}) \delta_{ij}) = 0\end{aligned} \tag{8.14}$$

Using equation 8.6 on the first term and expanding $\rho u_i u_j$ gives

$$\begin{aligned}&\frac{\partial(\rho u_i)'}{\partial t} + \\ &\frac{\partial}{\partial x_j}(\rho' \widetilde{u}_i \widetilde{u}_j + \rho u_i'' \widetilde{u}_j + \rho u_j'' \widetilde{u}_i + \\ &\rho u_i'' u_j'' - \overline{\rho u_i'' u_j''} + p' \delta_{ij}) = 0\end{aligned} \tag{8.15}$$

Using equation 8.7 on the second term and rewriting the resulting equation by moving all non-linear terms to the right-hand side gives

$$\begin{aligned}&\frac{\partial(\rho u_i)'}{\partial t} + \\ &\frac{\partial}{\partial x_j}(\widetilde{u}_j(\rho u_i)' + \widetilde{u}_i(\rho u_j)' - \rho' \widetilde{u}_i \widetilde{u}_j + p' \delta_{ij}) = \\ &- \frac{\partial}{\partial x_j}(\rho u_i'' u_j'' - \overline{\rho u_i'' u_j''})\end{aligned} \tag{8.16}$$

Equation 8.16 is the linearized momentum equation on the left-hand side with source terms on the right-hand side. That the left-hand side of 8.16 is the linearized momentum equation can be seen through differentiation of the term $\rho u_i u_j$ as

$$\begin{aligned}&\mathrm{d}(\rho u_i u_j) = \mathrm{d}\left(\frac{(\rho u_i)(\rho u_j)}{\rho}\right) \\ &= u_i \mathrm{d}(\rho u_j) + u_j \mathrm{d}(\rho u_i) - u_i u_j \mathrm{d}(\rho)\end{aligned} \tag{8.17}$$

Now we proceed to derive the linear equation for total energy. Averaging the inviscid energy equation (equation 8.3) gives

$$\frac{\partial \overline{\rho e_0}}{\partial t} + \frac{\partial}{\partial x_j}(\overline{\rho h_0 u_j}) = 0 \tag{8.18}$$

and subtracting equation 8.18 from equation 8.3

$$\frac{\partial(\rho e_0)'}{\partial t} + \frac{\partial}{\partial x_j}(\rho h_0 u_j - \overline{\rho h_0 u_j}) = 0 \tag{8.19}$$

Inserting the expressions 8.9 and 8.10 into equation 8.19 keeping the linear terms on the left side and moving the non-linear terms to the right-hand side gives

$$\begin{aligned}&\frac{\partial(\rho e_0)'}{\partial t}+\frac{\partial}{\partial x_j}(\rho'\widetilde{h}_0\widetilde{u}_j+\rho\widetilde{h}_0u_j''+\rho h_0''\widetilde{u}_j)=\\&-\frac{\partial}{\partial x_j}(\rho h_0''u_j''-\overline{\rho h_0''u_j''})\end{aligned}\tag{8.20}$$

Using the decomposition 8.7 and 8.8, equation 8.20 can now be rewritten on the form

$$\begin{aligned}&\frac{\partial(\rho e_0)'}{\partial t}+\frac{\partial}{\partial x_j}(\widetilde{h}_0(\rho u_j)'+\widetilde{u}_j(\rho h_0)'-\rho'\widetilde{h}_0\widetilde{u}_j)=\\&-\frac{\partial}{\partial x_j}(\rho h_0''u_j''-\overline{\rho h_0''u_j''})\end{aligned}\tag{8.21}$$

where the left side is the linear energy equation and the right-hand side contains all non-linear terms.

The resulting linear Euler equations with source terms are here summarized

$$\begin{aligned}&\frac{\partial\rho'}{\partial t}+\frac{\partial(\rho u_j)'}{\partial x_j}=0\\&\frac{\partial(\rho u_i)'}{\partial t}+\\&\frac{\partial}{\partial x_j}(\widetilde{u}_j(\rho u_i)'+\widetilde{u}_i(\rho u_j)'-\rho'\widetilde{u}_i\widetilde{u}_j+p'\delta_{ij})=\\&-\frac{\partial}{\partial x_j}(\rho u_i''u_j''-\overline{\rho u_i''u_j''})\\&\frac{\partial(\rho e_0)'}{\partial t}+\\&\frac{\partial}{\partial x_j}(\widetilde{h}_0(\rho u_j)'+\widetilde{u}_j(\rho h_0)'-\rho'\widetilde{h}_0\widetilde{u}_j)=\\&-\frac{\partial}{\partial x_j}(\rho h_0''u_j''-\overline{\rho h_0''u_j''})\end{aligned}\tag{8.22}$$

The linear Euler equations above, equations 8.22, have been derived from the Euler equations without approximations or assumptions

of the nature of the flow. The equations above are in fact still the non-linear Euler equations. But if one argue that the right-hand side of equations 8.22 is in some way known, then the equations on the left-hand side are the linear Euler equations. The right-hand side could for example be given by a large eddy simulation or DNS which also provides the reference solution for the linear Euler equations. The equations 8.22 would then be an analogy for acoustic generation and radiation.

Unlike scalar wave operators, the linear Euler equations also supports vorticity and entropy waves. This is both an advantage and a disadvantage for the linear Euler equations as an analogy. The advantage is that entropy and vorticity waves generated by the source term are indeed governed by the linear Euler equations. The disadvantage is that this may cause instabilities. Stability analysis of the linear Euler equations show that vorticity and entropy waves can in some cases grow without bound in the presence of mean shear. The near-field solution would then be dominated by this homogeneous solution instead of the forced solution which is sought for. This does not necessarily mean that the far-field solution is affected by these instabilities. The instabilities will not radiate sound and contaminate the far-field as long as the acoustic characteristic variables are not too strongly coupled with the vorticity and entropy characteristic variables. There were no problems with instabilities in the simulations presented in the present work but it is important to know that control of entropy and vorticity waves may be necessary in some flows to avoid potential problems.

8.3 Approximations of Source Terms

One of the purposes of this work is to evaluate the effect of simplifications of the source terms in the linear Euler equations. In the SNGR only the velocities are modeled. This means that fluctuations of total enthalpy and density are not known. The first step in simplifying the source terms is to rewrite and approximate the heat source term in the energy equation. Begin by identifying

$$\rho h_0'' = \left(\frac{p}{\rho} - \widetilde{\left(\frac{p}{\rho}\right)}\right)\frac{\gamma}{(\gamma-1)} + \frac{1}{2}\rho\left(u_k u_k - \widetilde{u_k u_k}\right) \tag{8.23}$$

The first term can be written in terms of temperature. The first Reynolds term can be decomposed in Favre averages of velocities and

the associated fluctuations. The last term can also be decomposed and rewritten in the same manner. After some algebra the following expression is obtained

$$\rho h_0'' = \rho C_p T'' + \rho \widetilde{u}_k u_k'' + \frac{1}{2}\rho \left(u_k'' u_k'' - \widetilde{u_k'' u_k''} \right) \tag{8.24}$$

which leads to

$$\begin{aligned} &\rho h_0'' u_j'' = \\ &\rho C_p T'' u_j'' + \rho \widetilde{u}_k u_k'' u_j'' + \frac{1}{2}\rho \left(u_k'' u_k'' - \widetilde{u_k'' u_k''} \right) u_j'' \end{aligned} \tag{8.25}$$

If we neglect trippel correlations of velocities we obtain

$$\rho h_0'' u_j'' = \rho C_p T'' u_j'' + \rho \widetilde{u}_k u_k'' u_j'' \tag{8.26}$$

and thus

$$\begin{aligned} &\rho h_0'' u_j'' - \overline{\rho h_0'' u_j''} = \\ &C_p \left(\rho T'' u_j'' - \overline{\rho T'' u_j''} \right) + \widetilde{u}_k \left(\rho u_k'' u_j'' - \overline{\rho u_k'' u_j''} \right) \end{aligned} \tag{8.27}$$

The following notation is introduced

$$\begin{aligned} \mathcal{T}_{ij} &= \rho u_i'' u_j'' - \overline{\rho u_i'' u_j''} \\ \mathcal{Q}_j &= C_p \left(\rho T'' u_j'' - \overline{\rho T'' u_j''} \right) \end{aligned} \tag{8.28}$$

Then the simplified source terms for the linear Euler equations can be written as

$$\begin{aligned} \text{Continuity} &= 0 \\ \text{Momentum} &= -\frac{\partial}{\partial x_j} \left(\mathcal{T}_{ij} \right) \\ \text{Energy} &= -\frac{\partial}{\partial x_j} \left(\mathcal{Q}_j + \widetilde{u}_i \mathcal{T}_{ij} \right) \end{aligned} \tag{8.29}$$

The next step in the simplification of the source terms is to neglect temperature fluctuations. The source terms are then

$$\begin{aligned} \text{Continuity} &= 0 \\ \text{Momentum} &= -\frac{\partial}{\partial x_j}\left(\mathcal{T}_{ij}\right) \\ \text{Energy} &= -\frac{\partial}{\partial x_j}\left(\widetilde{u}_i \mathcal{T}_{ij}\right) \end{aligned} \tag{8.30}$$

In the last step of simplifications of the source terms fluctuations of density are neglected, i.e.

$$\begin{aligned} \text{Continuity} &= 0 \\ \text{Momentum} &= -\frac{\partial}{\partial x_j}\overline{\rho}\left(u_i' u_j' - \overline{u_i' u_j'}\right) \\ \text{Energy} &= -\frac{\partial}{\partial x_j}\overline{u}_i\overline{\rho}\left(u_i' u_j' - \overline{u_i' u_j'}\right) \end{aligned} \tag{8.31}$$

where the primed velocities now are fluctuations associated with the ordinary time averaged velocities.

8.4 Numerical Simulation and Validation of Theory

8.4.1 Numerical Scheme

The code for direct simulation and the linear Euler code are based on the same numerical scheme. The convective terms are discretized with a six point stencil. The coefficients of Tam's [15] fourth-order dispersion relation preserving finite difference scheme is converted to the equivalent finite volume coefficients. The diffusive terms in the direct simulation code are discretized using a compact second-order scheme. A fourth-order four step Runge-Kutta time marching technique is used for the time stepping. Artificial selective damping is used to prevent spurious waves from the boundaries and regions with stretching to contaminate the solution. The manner in which the artificial selective damping is introduced is described in Eriksson [14].

8.4.2 Boundary Conditions

The mixing layer consists of an upper stream with a Mach number of $M_1 = 0.5$ and a lower stream with Mach number $M_2 = 0.25$. At the

interface between the two streams a hyperbolic-tangent profile is used as inflow boundary profile. The inlet streamwise profile is

$$u_{in} = \frac{U_1 + U_2}{2} + \frac{U_1 - U_2}{2} \tanh\left(\frac{2y}{\delta_\omega(0)}\right) \tag{8.32}$$

where U_1 and U_2 are the upper and lower velocities respectively. The initial vorticity thickness $\delta_\omega(0)$ defines the thickness of the incoming velocity profile, see figure 8.1. The velocity at the inflection point is defined by $U_0 = (U_1 + U_2)/2$. The spanwise velocity v_0 is set to zero at the inlet. The pressure and density are constant over the inlet and are set to normal atmospheric conditions. The Reynolds number for this flow based on the initial vorticity thickness $\delta_\omega(0)$ is $Re_\omega = \delta_\omega(0)U_0/\nu = 1.58 \times 10^5$.

The absorbing boundary conditions used are based on local analysis of characteristic variables, Engquist and Majda [36, 37]. The boundary conditions handle radiation boundaries quite well as long as the outgoing waves to be absorbed are not at too high incidence angle and they are exact and non-reflecting for waves normal to the boundary. The amount of reflection from the radiation boundary is very small for these boundary conditions. The same holds for the inlet boundary. The reason for this is that the only disturbances reaching these boundaries are acoustic waves with comparably small amplitudes. At the outflow boundary, however, there are vorticity and entropy waves as well as acoustic waves convected through the boundary. The large difference in energy of the vorticity and entropy waves leaving the computational domain at the outflow compared to the acoustic waves cause a major problem. Although most of the energy in the outgoing vorticity and entropy waves is absorbed and only a small portion of the energy is reflected back into the computational domain, the reflected part comes back as acoustic waves contaminating the solution.

To aid the absorbing boundary conditions at the outflow region a buffer region is applied at the last section of the computational domain. The mesh is also stretched in the flow direction in this region to help attenuate disturbances through the artificial dissipation in the numerical scheme. This method of taking care of outgoing disturbances was successfully used by Colonius [34] and Bogey *et al.* [35]. The term added to the governing equations is

$$\frac{\partial Q}{\partial t} = \cdots - \frac{c\sigma(x,y)}{\Delta x}(Q') \tag{8.33}$$

where

$$\sigma(x,y) = \sigma_{max}\left(\frac{x - x_0}{x_{max} - x_0}\right)^2 \tag{8.34}$$

Q denotes the solution vector and $\sigma_{max} = 0.1$; x_0 and x_{max} are the beginning and end of the buffer region. The disturbance Q' is in the direct simulation computed as $Q - \overline{Q}^*$. The term $\overline{Q}^*$ is a time average calculated using a low pass filter where the average from time step n is calculated from the average at time step $n-1$ and the solution at time step n as

$$\overline{Q}^*_{(n)} = \alpha\overline{Q}^*_{(n-1)} + (1-\alpha)Q_{(n)} \tag{8.35}$$

where α is a number close to one (further details below).

The parabolic shape of $\sigma(x,y)$ ensures that the damping term will not cause reflections into the computational domain. The stretching of the mesh in the buffer region is also done gradually with very small amount of stretching at the beginning and more aggressive once the damping term in the buffer region is larger.

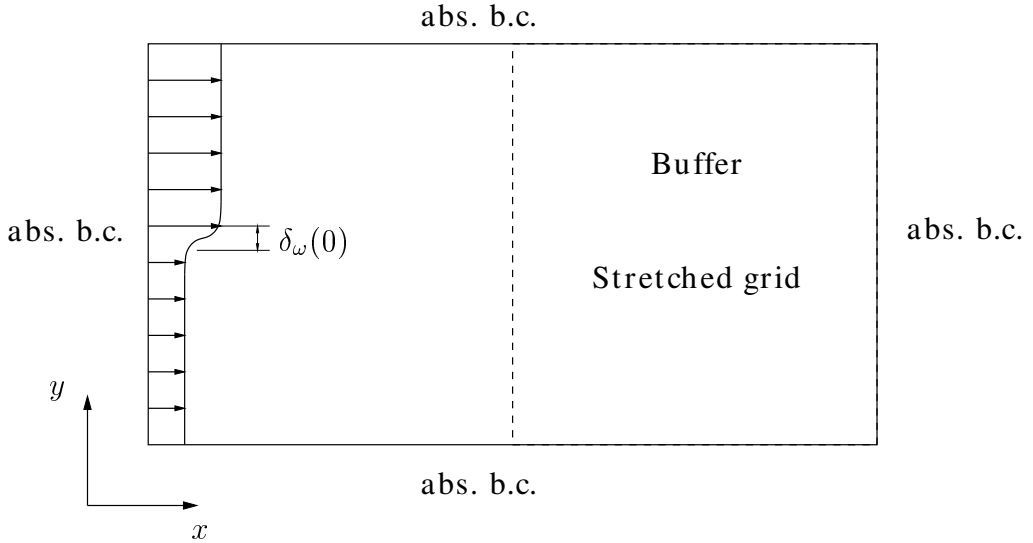

Figure 8.1: Computational domain

8.4.3 Forcing

A two-dimensional laminar shear layer is unstable by nature and will start to break up if the computational domain is long enough. This process might take some time though and the laminar part of the shear layer can be quite long in the streamwise direction. The acoustic field produced in this process will also be more or less stochastic with peaks in the spectra for the frequencies corresponding to the natural instability frequencies of the shear layer. To get better control of the shear layer and to make it break up faster, forcing is applied at the inflow boundary. This forcing is done using the inflow absorbing boundary conditions. The incoming vorticity characteristic variable is modulated at the fundamental frequency of the incoming profile. The resulting forcing enters the spanwise inflow velocity component as

$$v_{in} = v_0 + A\sin(\omega_0 t) \tag{8.36}$$

where A is the amplitude of the forcing. The forcing is only applied in the region of the hyperbolic-tangent profile. Since the forcing is included as a part of the absorbing boundary conditions, the forcing does not interfere with the absorbing property of the boundary condition and the amount of spurious waves created by the forcing is kept to a minimum. An important detail is that the forcing added in the direct simulation is also added in the linear Euler simulation. The reasoning behind this is that unless this is done, the boundary condition for the linear Euler simulation is not consistent with the sources evaluated from the direct simulation. The result from not using forcing in the linear Euler simulation is growing instabilities.

Bogey [35] computed the fundamental frequency based on the instability theory of Michalke [38] as

$$f_0 = 0.132\left[\frac{U_0}{\delta_\omega(0)}\right] \tag{8.37}$$

The shear layer is forced at two frequencies. The fundamental frequency f_0 and half the fundamental frequency $f_0/2$. In this way the forcing at the fundamental frequency will induce the creation of vortices at a frequency of f_0 which are convected downstream by the convection velocity. The second forcing at half the fundamental frequency will in turn induce a process where two successive vortices start to roll up around each other. This pair of vortices will after a short period of time

start to merge and form a larger vortex. The frequency of this pairing will be denoted $f_p = f_0/2$ and the pairing time $T_p = 2T_0$. In this work, $A = 0.2$ for the forcing at the fundamental frequency f_0 and $A = 0.1$ for $f_0/2$.

8.4.4 Computational Setup

The computational mesh consists of 551×261 (x, y) mesh points. The physical size of the mesh is $0 \leq x \leq 6$ and $-3 \leq y \leq 3$, equivalent of $0 \leq x \leq 300\delta_\omega(0)$ and $-150\delta_\omega(0) \leq y \leq 150\delta_\omega(0)$ for $\delta_\omega(0) = 0.02[m]$. The mesh is uniform in the streamwise direction for the first 451 points with a cell length of $\Delta x = 0.375\delta_\omega(0)$. The last hundred points are used to build the buffer region in which the mesh is stretched and damping terms are added to the equations. The last cell at the outflow boundary has a cell length of $\Delta x = 4.1\delta_\omega(0)$. In the spanwise direction the mesh points are concentrated to the mixing region and stretched towards the outer boundary. The minimum cell height in the mixing region is $\Delta y = 0.164\delta_\omega(0)$ and increases slowly to $\Delta y = 0.3\delta_\omega(0)$ at $|y| \approx 5\delta_\omega(0)$. The stretching continues all the way to the boundary where the cell height is $\Delta y = 3.0\delta_\omega(0)$. With a fundamental frequency f_0 of 789Hz the emitted sound waves have a wavelength of $\lambda = 0.87[m]$ which correspond to $14\Delta y$ in the outer region so the propagating sound is well resolved in the entire domain. How the wavelength is related to the fundamental frequency will be discussed when presenting the results below.

8.4.5 Direct Simulation

The direct simulation started with the hyperbolic-tangent profile as initial solution. To achieve a periodic solution the simulation was run for 30 000 time steps at $\mathrm{CFL} = 0.5$ which is equivalent to 40 pairing periods T_p. During this time the low-pass filter average (equation 8.35) was sampled with increasing value of the factor α. For the last 20 periods $\alpha = 0.9999$ was used before α was finally set to 1.0. This to ensure that the reference solution for the buffer layer would be representative of the true time average of the flow in the buffer layer. The sampling of the solution was then performed during 18432 time steps. With a fixed time step at $\mathrm{CFL} \approx 0.5$ this is equivalent to 24 periods with 768 time steps per period. In each time step a limited part of the solution called the source region was saved. The source region was defined as $-20\delta_\omega(0) \leq y \leq 20\delta_\omega(0)$ and $0 \leq x \leq 300\delta_\omega(0)$. The total amount of

disk space required for this simulation was about 30 Gigabytes and the sampling took about 20 hours on an alpha XP-900 466 MHz processor.

8.4.6 Linear Euler Simulation

The linear Euler simulation used the solution from the direct simulation as initial solution and was performed during 18432 time steps. The time averaged solution from the direct simulation was used as reference solution. At each time step the solution from the direct simulation was used to evaluate the source terms. After the initial disturbances had left the computational domain the solutions could be compared. This procedure was repeated with all four sets of source terms; the full source terms (equation 8.22), the temperature based (equation 8.29), constant temperature (equation 8.30) and constant density source terms (equation 8.31).

8.5 Acoustic Solution

The far-field acoustic solution is displayed by the dilatation $\partial u_i/\partial x_i$. It is favorable to use dilatation as acoustic variable instead of pressure. The pressure in the direct simulation has a tendency to fluctuate in the computation at a very low frequency. The reason for this is probably associated with the absorbing boundary conditions. This makes it hard to compare the direct simulation with the linear Euler solutions. The dilatation is in the far-field related to pressure as

$$\Theta = \frac{\partial u_i}{\partial x_i} = -\frac{1}{c_0^2 \rho_0}\left(\frac{\partial p}{\partial t} + u_i \frac{\partial p}{\partial x_i}\right) \tag{8.38}$$

Given that the drift in pressure is linear in time the dilatation will show a non-zero but constant time average. This seems to be confirmed with the results of the dilatation of the time averaged solution which show a nearly constant and non-zero dilatation in the whole domain. The dilatation of the direct simulation is thus instead compared to the dilatation of the fluctuations of the linear Euler solutions. Vorticity is used to display the near-field of the mixing layer.

8.6 Results

Figure 8.2 shows a snapshot of the vorticity in the near-field and the dilatation in the far-field for the direct simulation and the linear Euler simulation with full source terms (equation 8.22). The solutions seem to be very similar. The phase and amplitude also seem to be correct. Some wiggles that are visible in the direct simulation are absent in the linear solution. The reason for this is probably non-linearities in the direct simulation. The solutions from the linear Euler simulations using the simplified sources (equations 8.29-8.31) are not shown due to the fact that it is hard see any difference in the solutions compared to the full source term simulation

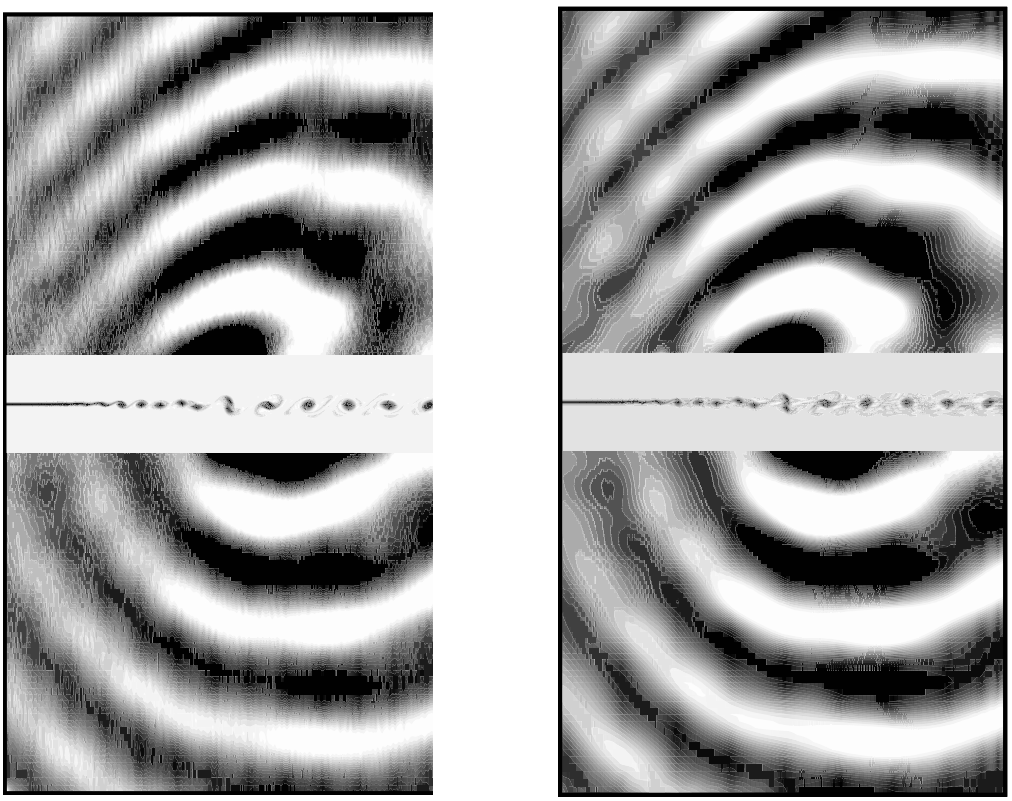

(a) Direct simulation

(b) Linear Euler simulation with full source terms

Figure 8.2: Vorticity and dilatation for direct simulation and linear Euler equations using the full source terms, equation 8.22.

Figure 8.3 shows the instant pressure fluctuation at a line at $x = 2.0[m]$ and $0.5 \leq y \leq 3.0[m]$ for the direct simulation and the different linear Euler solutions. The average pressure has been corrected for the solution to the direct simulation to avoid the problem with the drift in the average pressure. The phase and amplitude of the linear Euler solutions are in good agreement with the direct simulation except very near the mixing layer. The deviation in this region is probably a result of the error in the time averaged pressure. The solutions for the different source terms are clearly very similar.

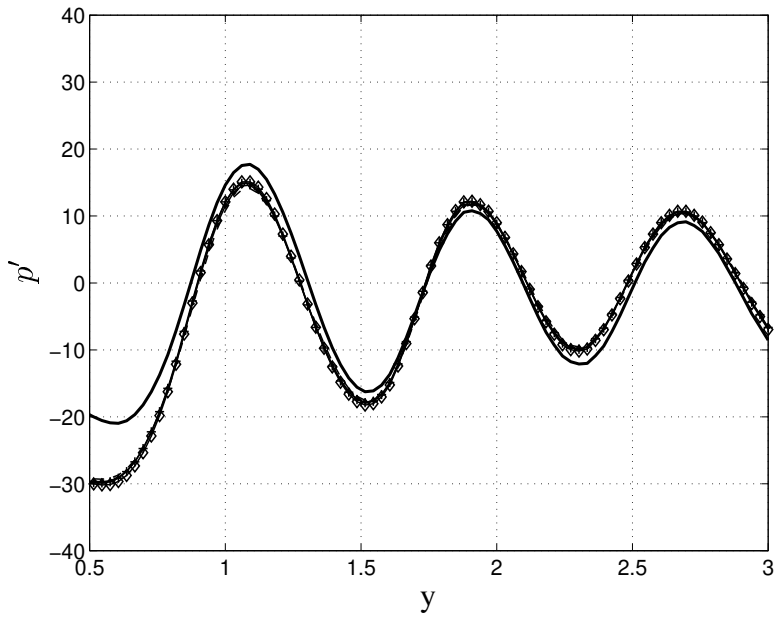

Figure 8.3: Pressure disturbance at $x = 2.0[m]$, $0.5 \leq y \leq 3[m]$. Solid line: direct simulation; others: different source terms

Figure 8.4 shows a pairing of two vortices at four different stages. The time difference between two subsequent figures from (a) to (d) is equivalent to one fourth of a pairing period. The pairing takes place at half the fundamental frequency so the pairing period time is $T_p = 2T_0$. During this time the merging vortices complete one half rotation around each other. The vortex pair is a rotating quadrupole and has as such four lobes. Thus, the merging process results in one full period of sound emitted at a period time of T_p, i.e. at the pairing frequency f_p of the mixing layer. The resulting wavelength of the emitted sound is $\lambda = c_0/f_p = 341.56/394.5 = 0.86[\mathrm{m}]$. It is during this time that most of the sound is generated and emitted.

So far the results are similar to the ones achieved by Bogey [35]. But because the physical region in this simulation is relatively a little longer than the one in Bogey [35], there is room for merged vortices to continue emitting sound as they are convected downstream. This is evident from figure 8.4 where one can see that there are two regions where more sound is produced than elsewhere. This gives a slightly biased directivity with two lobes in the lower and upper regions and it is especially clear in the upper half of the computational domain.

Figure 8.5 shows the directivity of the time average of the square of the dilatation. Two lobes of directivity for the lower and upper regions are clearly marked at $\varphi \approx \{-95°, -54°, 39°, 76°\}$. This asymmetry in the directivity is a result of the different velocities in the upper and lower halves of the computational domain. One can again see that there are very small differences in the solutions for the different source terms.

8.7 Conclusions

The exact source terms for the linear Euler equations and the inviscid linear energy equation has been derived from the non-linear Euler equations and inviscid energy equation. Simplifications of the source terms have also been presented. These source terms have been validated through numerical simulations. The solutions from the direct simulations and the solutions from the proposed equations are in good agreement. Some differences are present but the cause is believed to be due to effects of the boundary conditions. The differences are very small between the solutions from the different source terms. Even when the source terms are based only on velocity fluctuations and all other instationary effects are neglected, the solution was nearly exactly the same as for the full source terms. This implies that the major source of sound in this flow is fluctuations of vorticity. Whether this is true at higher Mach numbers or with larger differences in temperature remains to be seen.

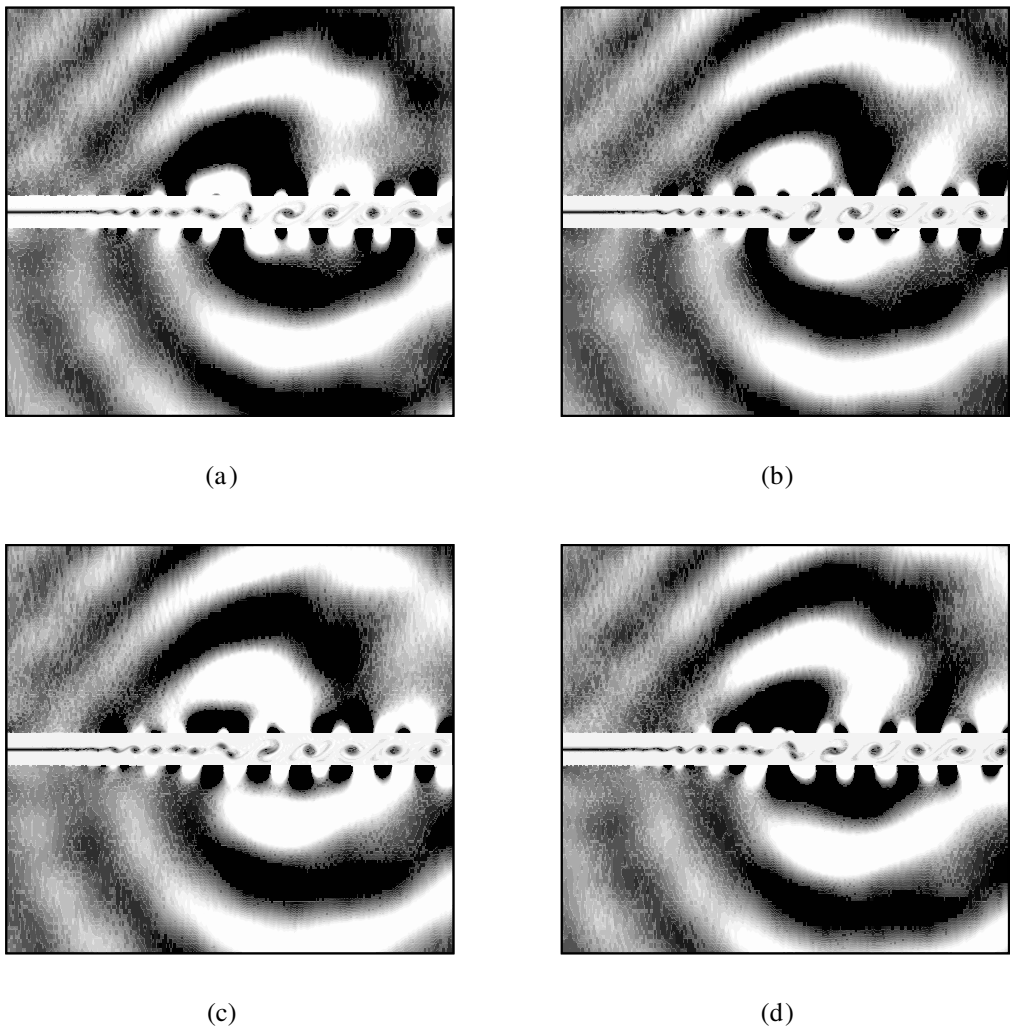

(a) (b)

(c) (d)

Figure 8.4: Vorticity and dilatation for direct simulation. $0 \leq x \leq 3.26$, $-1.5 \leq y \leq 1.5$

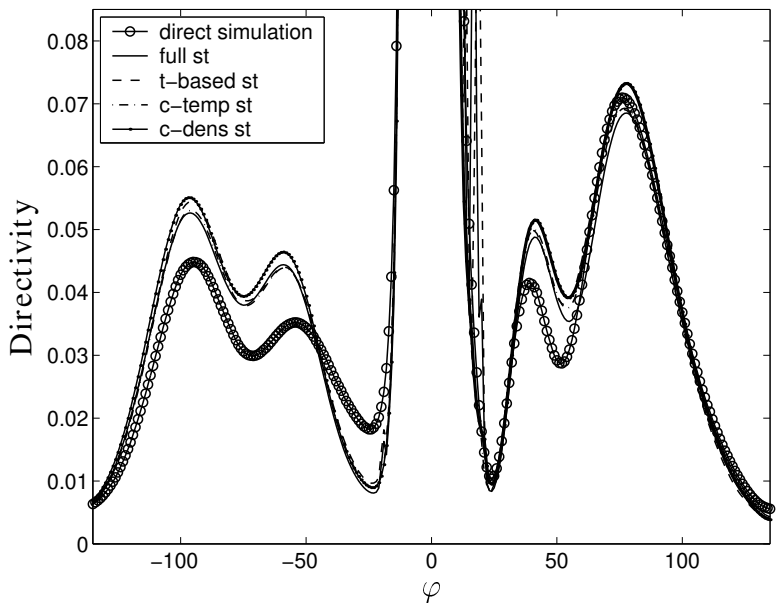

Figure 8.5: Directivity displayed as time average of square of dilatation at an arc around $x_0 = 2.0$, $y_0 = 0$ with radius $r = 1.0$ at angles $-135 \leq \varphi \leq 0$ degrees from the x-axis and $x_0 = 1.6$, $y_0 = 0$ with radius $r = 1.0$ at angles $0 \leq \varphi \leq 135$ degrees. Direct simulation, full source terms (full st); temperature based (t-based st); constant temperature (c-temp st); constant density (c-dens st).

Chapter 9

3D Jet case - Stromberg Jet

The jet chosen for the validation of the SNGR method is a Mach 0.9 axisymmetric jet without co-flow. The original experiments were done by Stromberg *et al.* [39]. The Reynolds number based on jet exit diameter and velocity is $\mathrm{Re} = 3600$ with a nozzle diameter of $D_j = 7.9 \times 10^{-3}[\mathrm{m}]$. This combination of Mach number and Reynolds number was in the experiments achieved by performing the experiments in a low-pressure chamber. The following parameters define the flow field

Exit Mach number	M	0.9
Nozzle diameter	D_j	$7.9 \times 10^{-3}[\mathrm{m}]$
Jet exit velocity	U_j	$284[\mathrm{m/s}]$
Jet Reynolds number	Re	3600
Jet stagnation pressure	p_0	$3040[\mathrm{Pa}]$
Chamber pressure	p_c	$1765[\mathrm{Pa}]$
Jet stagnation temperature	T_0	$297[\mathrm{K}]$

The data from the experiments include half-velocity radius, centerline velocity and Mach number, radial profiles of Mach number as well as spectral information for several locations. The sound data available are sound pressure level directivity and far-field pressure spectra. In addition to the data from the experiments, a Direct Numerical Simulation (DNS) of the same jet was presented by Freund [40, 41]. The same profiles and point data are available from the DNS as well as radial profiles of turbulent quantities for various downstream locations. The results from the DNS are in excellent agreement with the experiments and both sources of data are used to validate the present methodology.

9.1 Jet Characteristics

Due to the low Reynolds number it would be expected that the flow field would be different from that of a typical high Reynolds jet. Jets at low Reynolds numbers have a tendency to be more tonal than at high Reynolds numbers as a result of large dominating instability modes emitting sound. The experiments show however that the far-field sound spectra is rather broad band [39] indicating that the major source of sound is turbulence mixing.

9.2 Comparison of RANS to DNS and Experiments

The Reynolds-Average Navier-Stokes solution (RANS) of the flow field is computed using a standard $k-\varepsilon$ turbulence model. The RANS solution is computed in axisymmetric coordinates. The reason for this is that the computational domain then can be extended to a very large distance from the nozzle exit and still using quite few computational cells. The computational domain for the axisymmetric RANS computation include a thin nozzle and is extended to a radius of $R = 400r_0$ from the nozzle exit. The nozzle has a area ratio of $A_j/A_{max} = 1/4$ with a smooth transition from the large to the small area.

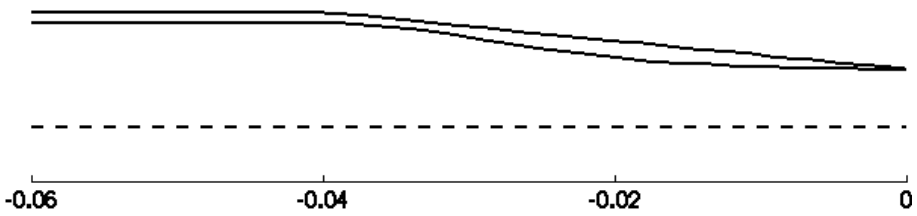

Figure 9.1: Nozzle in axisymmetric configuration. Solid line: nozzle; Dashed line: axis of symmetry (x-axis)

To force the jet to be laminar inside the nozzle a limiter was used to limit the turbulence length scale. By forcing the length scale to be less than $L_s = 10^{-5}[\mathrm{m}]$ for $x < 0.006$ the solution could be tuned to give as good matching as possible with the maximum turbulence kinetic energy of the DNS in the shear layer at $x/r_0 \approx 12$. It is easy to argue that the requirement to tune the RANS solution is a major flaw in this methodology. The purpose of this test case is however not to develop

a perfect RANS solver for low Reynolds number jets. The RANS solution is first of all used as a reference solution for the linearized Euler computations and as input to the stochastic modeling. Some tuning is therefore motivated at this stage in the development of the SNGR model.

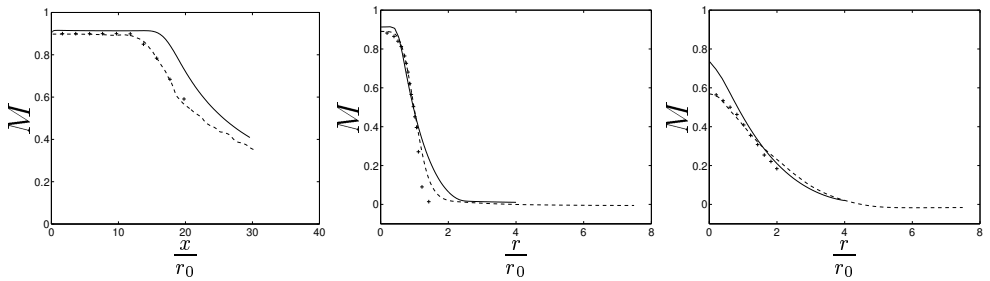

(a) Centerline Mach number profile

(b) Radial Mach number profile $x = 10r_0$

(c) Radial Mach number profile $x = 20r_0$

Figure 9.2: +++: Stromberg experiments; - - -: Freund DNS; ——: RANS in present study.

The centerline profile and two radial profiles of the Mach number are shown in figure 9.2. Data from the experiments and the DNS are also shown. The data from the RANS differ from the reference data in that the potential core length is longer in the RANS than in the experiments and in the DNS. Also the spreading characteristics of the RANS jet differ somewhat as can be seen in figures 9.2(b) and 9.2(c).

The turbulence kinetic energy and two components of the Reynolds stresses are shown in figure 9.3. The figure shows radial profiles of the DNS data and the RANS solution at six different downstream locations. The DNS data show a laminar flow exiting the nozzle and a rapid growth of turbulence quantities near the end of the potential core. The turbulence kinetic energy has its peak value close to $x/r_0 = 12.5$ and shows a decay further downstream. The Reynolds stresses show a similar development. The RANS solution shows a similar but yet slightly different picture. The peak value of the turbulence kinetic energy is about the same and located in the same region as in the DNS. This was the main tuning parameter in the RANS computation since a large part of the noise is expected to be generated in this region. The agreement with the DNS in other regions is slightly worse.

For use as reference solution in the linearized Euler computation the RANS solution is mapped from the axisymmetric mesh onto a fully

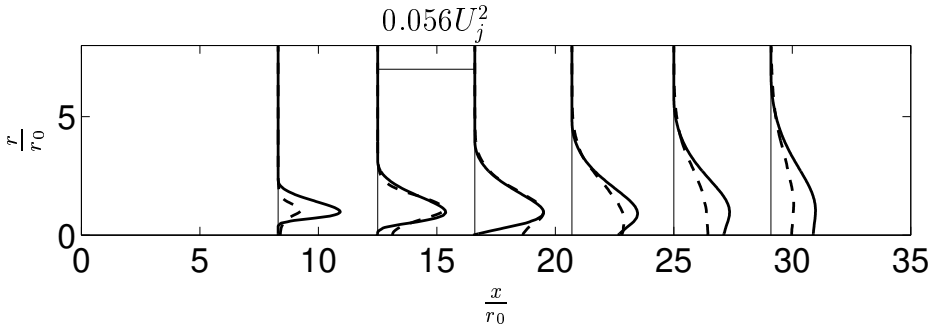

(a) $\overline{u^2} + \overline{v^2} + \overline{w^2}$ normalized by square of jet exit velocity

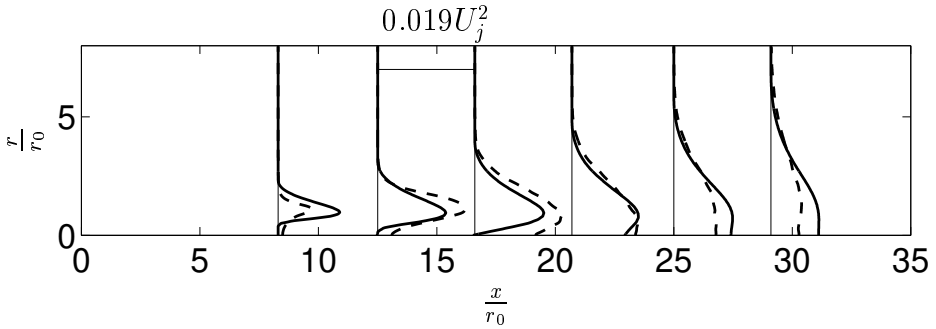

(b) Reynolds stress $\overline{uu}$ normalized by square of jet exit velocity

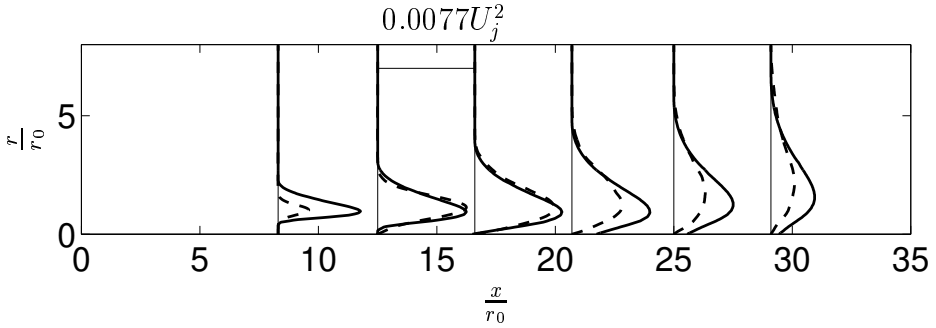

(c) Reynolds stress $\overline{uv}$ normalized by square of jet exit velocity

Figure 9.3: Profiles of turbulence quantities. Dashed lines: DNS by Freund [40, 41]; solid lines: present RANS prediction.

3D mesh suitable for linearized Euler computations. This is done by splitting all cells in the axisymmetric mesh into a uniform sub-mesh of 10×10 cells and performing a linear reconstruction of the sub-cell variation of the solution using information from the surrounding cells.

The reconstructed solution in each sub-cell is then mapped in a volume averaged way onto the 3D mesh to give the volume averaged solution.

9.3 SNGR Generation

The stochastic source term modeling is performed as described in Chapter 2 with the parameters set as given here. The distribution of wave numbers for which the SNGR model is applied is the same for the whole source volume. The lowest wave number k_1 is chosen so that $k_1 = k_{emin}/5$ where k_{emin} is the smallest value of k_e in the source volume. The highest generated wave number k_N was chosen so that the corresponding wave length is resolved with eight points per wave length, i.e. $k_N = 2\pi/(7\Delta_x)$. The number of wave numbers in the SNGR generation are $N = 30$ and have a logarithmic distribution given by equation 2.6. To change the spectral content in the far-field acoustic signals the integral time scale and length scale have been modified. Each have been multiplied by a factor to change the properties of the generated turbulence. The length scale in the computations is computed as $\Lambda = f_\Lambda c_\mu^{0.75} \overline{k}^{3/2}/\varepsilon$ and the time scale as $\tau = f_\tau \overline{k}/\varepsilon$ where $f_\Lambda = 2$ and $f_\tau = 5$.

The stochastic modeling is performed in the set of points within a cylinder extending from the nozzle exit down to $x/r_0 = 36$ where $\nu_t/\nu \geq 0.7$. The reasoning behind this is explained in Chapter 2.

The simplified source terms which include neglection of density fluctuations in the source terms, see equation 8.31, are used in the computations and the time averaged part of the source terms is computed as the computation develops.

9.4 Linearized Euler Computation

The computational domain for the linearized Euler computation is axisymmetric and extends from $-15r_0$ to $63r_0$ in the axial direction. The radial extent is $10r_0$ at the nozzle exit and $18r_0$ at the outflow with a smooth transition in between. The computational mesh is a curvelinear boundary-fitted multi-block mesh with 34 blocks. Slices of the block structure is shown in figure 9.4. The same nozzle geometry is used as in the RANS computation.

The resolution in the axial direction is $\Delta x = \Delta_x = 0.21r_0$ from $x = 0$ from the nozzle exit to the end of the physical part of the domain that

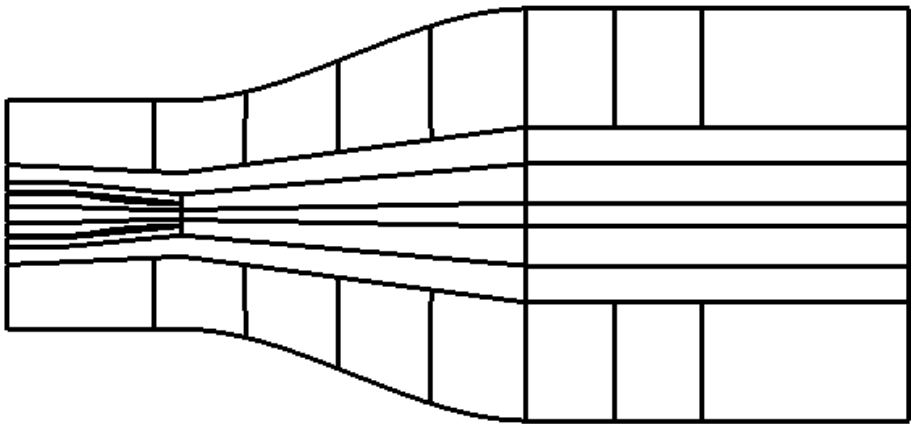

(a) z-plane through centerline.

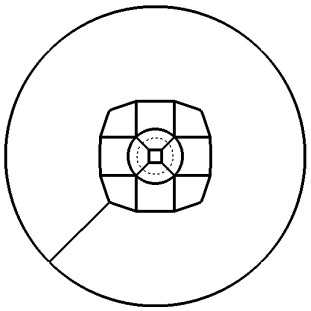

(b) x-plane at nozzle exit. Dashed line indicates nozzle exit diameter.

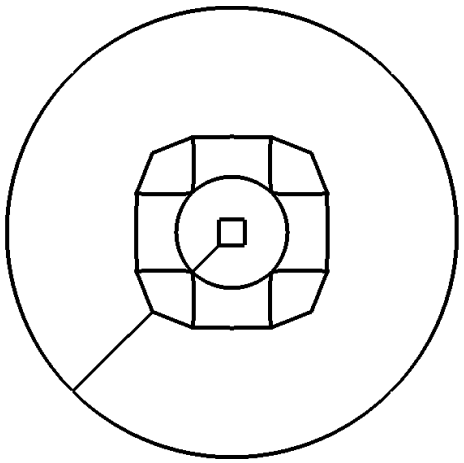

(c) x-plane at end of computational domain.

Figure 9.4: Slices of the block structure of the linearized Euler mesh.

ends at $x = 45r_0$. The resolution in the axial direction inside the nozzle and upstream of the nozzle is stretched about 5% to save nodes.

The cell size in the radial direction is about $\Delta r = 0.062r_0$ inside the nozzle and in the region of the nozzle exit. The mesh is stretched about $5-10\%$ in the radial direction until the cell size is $\Delta r \approx 0.23r_0$. Then the radial resolution is held constant all the way to the radial boundary. At

the outflow boundary ($x \approx 60r_0$) the radial cell size is more smoothed with a $\Delta r \approx 0.14r_0$ at the centerline and $\Delta r \approx 0.27r_0$ at the radial outer boundary.

The number of cells in the azimuthal direction varies in the radial direction. This is made possible by successively changing from polar to Cartesian blocks, see figure 9.4. The cell size in the azimuthal direction is about the same as for the radial direction near the center line and about twice as large at the radial boundary. This mesh supports acoustic waves propagating in the radial and axial direction with a Strouhal-number of $St = fD_j/U_j \leq 1.5$ without significant dissipation errors or dispersion errors.

Boundary conditions based on characteristic variables, see Chapter 4 are used on all free boundaries. A buffer layer is applied for $45r_0 < x < 63r_0$, see Chapter 4. The cell size in the buffer layer is stretched to increase the artificial numerical dissipation. The size of the first 10 cells in the buffer layer is $\Delta x = \Delta_x$ and for the remaining 40 cells the stretching is 3% per cell.

The time step in the computation is $\Delta t = 1.44 \times 10^{-7}$[s] equivalent to a maximum CFL-number ≤ 0.5. The total number of time steps in the computation is 33000.

9.5 Near-Field Data

The pressure is recorded in a point located at $(x, y, z) = (18r_0, r_0, 0)$ and the signal is shown in figure 9.5(a). The same data is available from the DNS computations by Freund [40]. The frequencies are similar but the amplitude of the present results is about one tenth of that in the DNS. The low amplitude in the present simulation is due to the relatively high factor f_τ on the time scale compared to the factor for the length scale f_Λ. Also shown in figure 9.5(b) is the spectrum of the same signal. To reduce the effects of a truncated time-series when the spectrum is computed, the pressure signal is windowed by a function $w(t)$ defined by [40]

$$w(t) = \frac{1}{2}\left[\tanh\left(5\frac{t-t_1}{t_1-t_0}\right) + \tanh\left(5\frac{t-t_2}{t_2-t_f}\right)\right] \tag{9.1}$$

where t_0, t and t_f are the start time, actual time and end time in the recording and $t_1 = 0.05(t_f - t_0)$ and $t_2 = 0.95(t_f - t_0)$. The window function $w(t)$ scaled to fit in the figure is shown in figure 9.5(a). The

spectrum has a peak at $St = 0.1$ with a decay for higher frequencies. The spectrum is not available from the DNS so a comparison can not be made.

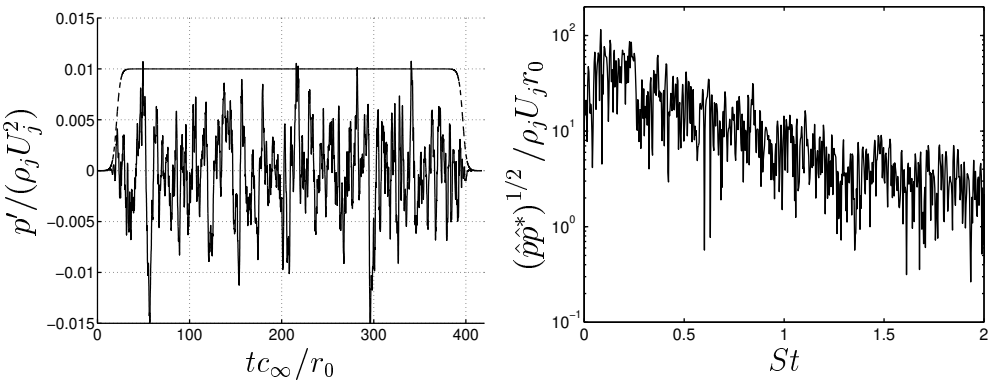

(a) Pressure history and window function ($0.01 \times w(t)$)

(b) Pressure spectrum

Figure 9.5: Near-field pressure data at $x = 18r_0$ and $r = r_0$.

9.6 Far-field Data

Directivity of scaled sound pressure level, SPL is shown in figure 9.6(a). The observation points for the SPL estimates are located on an arc at angles θ from 5 to 120 degrees from the jet axis at a radius of 30 jet diameters from the nozzle exit.

The scaling of the SPL is performed to compensate for the low ambient chamber pressure compared to normal atmospheric conditions. The SPL is computed as $\mathrm{SPL} = 20\log_{10}(p'_{rms}/p_{ref})$ where $p_{ref} = 2 \times 10^{-5}(p_c/p_a)$, where p_c is the ambient chamber pressure and p_a is normal atmospheric pressure. The SPL in the present simulation is within 1dB to that of the DNS for large angles but with a less pronounced directivity the difference is about 6dB at $\theta = 30$ degrees.

The spectrum of the pressure at a point located at $(r, \theta) = (60r_0, 30)$ is shown in figure 9.6(b). The spectrum clearly shows that the spectral content in the far-field is erroneous. The peak in the spectra is located at a frequency of $St = 1.5$. This is about seven times too high compared to the DNS data by Freund [40, 41] in which the peak is located at

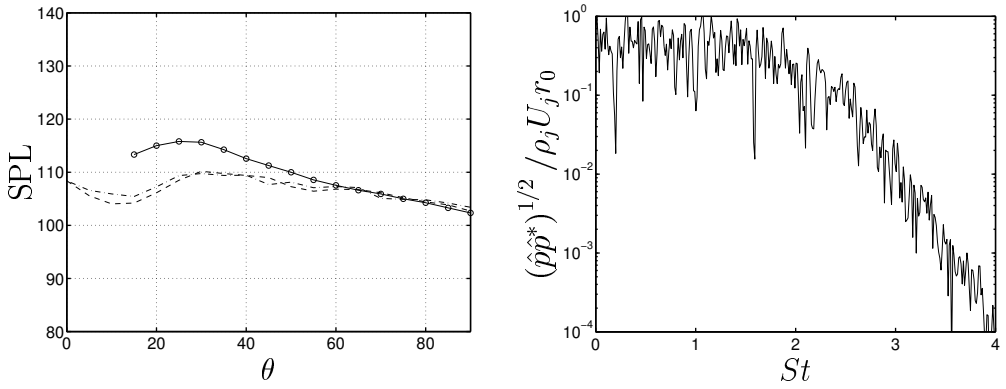

(a) Sound pressure level, SPL.

(b) Pressure spectrum at $R = 30D_j$ and $\theta = 30$ degrees

Figure 9.6: Far-field pressure data.

$St = 0.2$. The DNS data are in agreement with the measurements in the experiments by Stromberg *et al.* [39].

The errors in the spectral content in the far-field is not attributed to the choice of the factors f_Λ and f_τ. These have been modified several times with the same result in the far-field spectra. The SPL in the far-field is receptive to changes in f_Λ and f_τ but the spectral content is not. An increase in length scale by a $f_\Lambda > 1$ lowers the compactness of the turbulence as a source of sound and results in a higher SPL in the far-field. The same holds for a decrease in the integral time scale using a $f_\tau < 1$. The opposite relations holds of course. The length scale does however not affect the frequencies of the far-field sound but the time scale does so a change in time scale using a $f_\tau > 1$ should change the spectral distribution of the far-field sound.

The overestimation of high frequencies in the far-field sound, see figure 9.6(b), and the error in the directivity in figure 9.6(a) are in agreement though. It is well known that high frequencies refract to higher angles from the jet axis than lower frequencies. The underestimation of the SPL at small angles compared to the SPL at large angles confirm the errors in the frequency-distribution of the computed sound.

The errors in the frequencies must be attributed to some modeling effect. Probable reasons are low spectral resolution ar high wave numbers in combination with non-linearities of the source term.

Chapter 10

Conclusions

- The linearized Euler equations are an excellent wave operator for acoustic waves. The source terms derived in the present thesis give the correct driving force for the equations and result in an accurate prediction of the acoustic far-field.

- The original boundary conditions based on characteristic variables are not really sufficient for an aeroacoustic application. The reflection from an acoustic pulse is not too bad but there is certainly room for improvement by using the modified boundary conditions based on characteristic variables or boundary conditions based on asymptotic analysis of the linearized Euler equations. The results from a convected axisymmetric vortex show that a buffer layer is absolutely necessary to prevent reflection at outflow boundaries.

- The numerical accuracy and stability is up-to-date with what is considered to be necessary for an aeroacoustic application. The six cell fourth order spatial numerical scheme by Tam and Webb together with a four stage fourth order Runge-Kutta time marching technique ensures high accuracy in terms of dispersion relation and dissipation relation. Artificial numerical dissipation through the numerical scheme provides a controllable dissipation relation to ensure stability.

- The generation of turbulence through the SNGR method provides the specified time and space correlations.

- The simulations of a full three-dimensional jet are encouraging. There are however unresolved problems. The acoustic results so

far show unphysically high frequencies of which the cause is not known at present time. A probable reason is a combination of non-linear effects in the source terms and poor spectral resolution at high wave numbers. An other concern is the stability of the linearized Euler equations in highly sheared flows. A simple modification of the equations by neglecting gradients of the reference solution is probably too a drastic simplification even if it solves the stability issues.

Further investigations

- The non-linear effects in the source terms in combination with the spectral resolution of the SNGR generation needs to be investigated.

- The differences in the full linearized Euler equations and the modified Euler equations need to be investigated.

- Boundary conditions based on asymptotic analysis of the linearized Euler equations will be implemented. Their ability to absorb disturbances is superior to the boundary conditions based on characteristic variables. Tests of the modified boundary conditions based on characteristic variables and the boundary conditions based on asymptotic analysis of the linearized Euler equations will be conducted.

Chapter 11

Appendix

11.1 The Linearized Euler Equations

This section treats the linearization of the Euler equations on conservative form and the transformation of the conservative formulation to a primitive formulation.

The Euler equations can be written in a compact conservative form as

$$\frac{\partial Q}{\partial t} + \frac{\partial E}{\partial x} + \frac{\partial F}{\partial y} + \frac{\partial G}{\partial z} = 0 \tag{11.1}$$

where

$$Q = \begin{pmatrix} \rho \\ \rho u \\ \rho v \\ \rho w \\ \rho e_0 \end{pmatrix} \quad E = \begin{pmatrix} \rho u \\ \rho uu + p \\ \rho uv \\ \rho uw \\ \rho h_0 u \end{pmatrix} \quad F = \begin{pmatrix} \rho v \\ \rho uv \\ \rho vv + p \\ \rho vw \\ \rho h_0 v \end{pmatrix} \quad G = \begin{pmatrix} \rho w \\ \rho uw \\ \rho vw \\ \rho ww + p \\ \rho h_0 w \end{pmatrix} \tag{11.2}$$

The solution vector can be decomposed into a reference solution and a disturbance.

$$Q = Q_0 + Q' \tag{11.3}$$

The reference solution does not need to be homogeneous in space or constant in time but it is assumed to be given and not part of the new

solution vector Q'. A linearization of the equations is given by

$$\begin{aligned} E(Q) &= E(Q)_0 + \left(\frac{\partial E}{\partial Q}\right)_0 Q' + \text{HOT} \\ F(Q) &= F(Q)_0 + \left(\frac{\partial F}{\partial Q}\right)_0 Q' + \text{HOT} \\ G(Q) &= G(Q)_0 + \left(\frac{\partial G}{\partial Q}\right)_0 Q' + \text{HOT} \end{aligned} \tag{11.4}$$

where subscript *zero* indicates evaluation at reference solution. Using the relations above in equation 11.1 gives

$$\begin{aligned} &\frac{\partial Q_0 + Q'}{\partial t} + \\ &\frac{\partial}{\partial x}\left(E(Q)_0 + \left(\frac{\partial E}{\partial Q}\right)_0 Q'\right) + \\ &\frac{\partial}{\partial y}\left(F(Q)_0 + \left(\frac{\partial F}{\partial Q}\right)_0 Q'\right) + \\ &\frac{\partial}{\partial z}\left(G(Q)_0 + \left(\frac{\partial G}{\partial Q}\right)_0 Q'\right) = \text{HOT} \end{aligned} \tag{11.5}$$

The reference solution satisfies the Euler equations. Subtracting the reference solutions and neglecting the higher order terms gives

$$\frac{\partial Q'}{\partial t} + \frac{\partial}{\partial x}\left(A_0 Q'\right) + \frac{\partial}{\partial y}\left(B_0 Q'\right) + \frac{\partial}{\partial z}\left(C_0 Q'\right) = 0 \tag{11.6}$$

where $A_0 = (\partial E/\partial Q)_0$, $B_0 = (\partial F/\partial Q)_0$, $C_0 = (\partial G/\partial Q)_0$. Equations 11.6 are the Linearized Euler Equations (LEE) on compact conservative form. In tensor notation the equations are

$$\begin{aligned} \frac{\partial \rho'}{\partial t} + \frac{\partial (\rho u_j)'}{\partial x_j} &= 0 \\ \frac{\partial (\rho u_i)'}{\partial t} + \frac{\partial}{\partial x_j}(\widetilde{u}_j(\rho u_i)' + \widetilde{u}_i(\rho u_j)' - \rho'\widetilde{u}_i\widetilde{u}_j + p'\delta_{ij}) &= 0 \\ \frac{\partial (\rho e_0)'}{\partial t} + \frac{\partial}{\partial x_j}(\widetilde{h}_0(\rho u_j)' + \widetilde{u}_j(\rho h_0)' - \rho'\widetilde{h}_0\widetilde{u}_j) &= 0 \end{aligned} \tag{11.7}$$

The $(\cdot)'$ is a fluctuation associated with an ordinary time average $\overline{(\cdot)}$ and $(\cdot)''$ is is a fluctuation associated with a Favre time average $\widetilde{(\cdot)} = \overline{\rho(\cdot)}/\overline{\rho}$.

The linearized Euler equations can also be written in primitive form with solution vector $q' = [\rho', u'', v'', w'', p']$. The transformation of equations 11.6 to primitive form starts with the Taylor expansion

$$Q = Q(q_0 + q') = Q_0 + \left(\frac{\partial Q}{\partial q}\right)_0 q' + \text{HOT} \tag{11.8}$$

which in linear theory is the same as

$$Q' = Q - Q_0 = \left(\frac{\partial Q}{\partial q}\right)_0 q' \tag{11.9}$$

Using the definitions

$$M_0 = \left(\frac{\partial Q}{\partial q}\right)_0 \quad \text{and} \quad M_0^{-1} = \left(\frac{\partial q}{\partial Q}\right)_0 \tag{11.10}$$

we can rewrite equations 11.6 as

$$\frac{\partial q'}{\partial t} + \frac{\partial}{\partial x}\left(\widetilde{A}_0 q'\right) + \frac{\partial}{\partial y}\left(\widetilde{B}_0 q'\right) + \frac{\partial}{\partial z}\left(\widetilde{C}_0 q'\right) = 0 \tag{11.11}$$

where $\widetilde{A}_0 = M_0^{-1} A_0 M_0$, $\widetilde{B}_0 = M_0^{-1} B_0 M_0$, $\widetilde{C}_0 = M_0^{-1} C_0 M_0$. Equations 11.11 are the linearized Euler equations on compact primitive form. In tensor notation the same equations read

$$\begin{aligned}
&\frac{\partial \rho'}{\partial t} + \frac{\partial}{\partial x_j}\left(\overline{\rho} u_j'' + \rho' \widetilde{u}_j\right) = 0 \\
&\frac{\partial u_i''}{\partial t} + \frac{\partial}{\partial x_j}\left(u_i'' \widetilde{u}_j + \frac{\overline{p}}{\overline{\rho}}\right) = 0 \\
&\frac{\partial p'}{\partial t} + \frac{\partial}{\partial x_j}\left(p' \widetilde{u}_j + \gamma \overline{p} u_j''\right) = 0
\end{aligned} \tag{11.12}$$

11.2 Stability Analysis of Hyperbolic Equations

In this section Fourier analysis is used for a semi-discrete stability analysis of a one-dimensional convection equation. Relations for the dispersion relation and the dissipation relation for an even-order space

discretization is derived. Artificial dissipation through upwinding is also taken into account in the analysis. Also a fully-discrete stability analysis is performed for a four stage Runge-Kutta time discretization. Last, the correct way to introduce source terms in a 4:th order Runge-Kutta time marching technique is presented.

11.2.1 Semi-Discretization

Start with the model equation (one-dimensional convection equation with constant coefficient, c).

$$\frac{\partial u}{\partial t} + c\frac{\partial u}{\partial x} = 0 \tag{11.13}$$

Assuming that the spatial solution to equation 11.13 is known, the exact solution to this equation can be written as

$$u(x,t) = u_0 \exp(st) \exp(-ikx) \tag{11.14}$$

where u_0 is a constant amplitude and k is the wavenumber. The solution is decomposed into a time-dependent part and a space-dependent part as shown in equation 11.14. Since the spatial dependence is known, $\exp(-ikx)$, the time-dependence is to be determined, i.e. s in the time dependent part of the solution. Inserting the equation 11.14 into equation 11.13 results in

$$su_0 \exp(st) \exp(-ikx) - ikcu_0 \exp(st) \exp(-ikx) = 0 \tag{11.15}$$

which in turn gives a relation for s as

$$s = ikc \qquad \text{or} \qquad s = i\omega \qquad \text{where} \qquad \omega \equiv kc \tag{11.16}$$

where ω is the angular velocity by which the solution varies in a given point in space.

Reinserting this into the time dependent part of the solution, equation 11.14 gives that

$$z \equiv \exp(st) = \exp(ikct) \tag{11.17}$$

which has a purely imaginary exponent. The result is that the exact solution to equation 11.13 will have a periodic behavior in time without damping or amplification. Furthermore, ω is in direct proportion to the wavenumber k, because the phase velocity, i.e. the velocity of propagation defined by $c = \omega/k$, is the same for all wave numbers.

Now, an expression for s will be derived in the case of a semi-discretization of the one dimensional convection equation 11.13. The equation is discretized in space using a finite difference approximation. Discretized, equation 11.13 becomes.

$$\frac{\partial u_j}{\partial t} + c\frac{\partial u_j}{\partial x_j} = 0 \tag{11.18}$$

where j is the number of the cell over which the equation is to be analyzed, see figure 11.1. Now we introduce a finite difference approximation of the space derivative on a equidistant mesh.

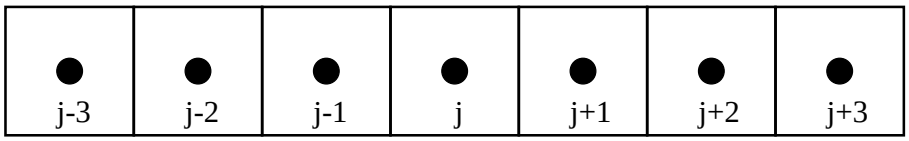

Figure 11.1:

$$\frac{\partial u_j}{\partial x_j} = \frac{1}{\Delta x}\sum_{l=-N}^{M} a_l u_{j+l} \tag{11.19}$$

and limit this analysis to $N = M$ and let $a_l = -a_{-l}$ with $a_0 = 0$. We can then construct a central difference scheme, i.e. an even-order approximation of the spatial derivative. Equation 11.18 then becomes

$$\frac{\partial u_j}{\partial t} + \frac{c}{\Delta x}\sum_{l=-M}^{M} a_l u_{j+l} = 0 \tag{11.20}$$

We can write the solution to equation 11.18 on the form

$$u_j = u_0 \exp(st)\exp(-ik\Delta x j) \tag{11.21}$$

Insert this into equation 11.20 above. The space-dependent part has been modified according to the space discretization. Observe that the time dependent part of the solution is still continuous, i.e. not discretized. This gives

$$su_0 \exp(st)\exp(-ik\Delta xj) + u_0 \exp(st)\frac{c}{\Delta x}\sum_{l=-M}^{M} a_l \exp(-ik\Delta x(j+l)) = 0 \tag{11.22}$$

which can be rewritten as

$$s = -\frac{c}{\Delta x}\sum_{l=-N}^{M} a_l \exp(-ik\Delta xl) \tag{11.23}$$

Using the fact that $a_l = -a_{-l}$ allows us to rewrite the above expression for s to

$$s = -\frac{c}{\Delta x}\sum_{l=1}^{M} a_l(\exp(-ik\Delta xl) - \exp(ik\Delta xl)) \tag{11.24}$$

With the identity

$$\sin(\Theta) = \frac{\exp(i\Theta) - \exp(-i\Theta)}{2i} \tag{11.25}$$

we get

$$s = \frac{2ic}{\Delta x}\sum_{l=1}^{M} a_l \sin(k\Delta xl) \tag{11.26}$$

The approximation of $z = \exp(st)$ (equation 11.17)in the semi-discretized case is then

$$z(k,t) = \exp\left(\frac{2ict}{\Delta x}\sum_{l=1}^{M} a_l \sin(k\Delta xl)\right) \tag{11.27}$$

In this case with an even-order discretization, the expression in the exponent of equation 11.27 is also purely imaginary giving a numerical scheme with zero numerical dissipation. Semi-discretized ω is however not directly proportional to k any more (cf. equation 11.16). The relation between ω and k is called the phase velocity or dispersion relation and is defined by

$$c^* = \frac{\mathrm{Im}(s)}{k} = \frac{\omega}{k} \tag{11.28}$$

where ω and c^* are dependent on k. The discretization of the spatial derivative in equation 11.13 results in an incorrect dispersion relation, and the phase velocity will be dependent on the wavenumber. Higher-order schemes generally result in more accurate dispersion relation for a larger range of wave-numbers than lower-order methods.

As an example, the resulting dispersion relation for a 4:th order space discretization is plotted in figure 11.2. The figure shows the phase velocity as a function of wave number. The wave number is scaled with $\frac{1}{\Delta x}$ to give the quantity $\theta = k\Delta x$. The phase velocity is scaled with $\frac{c}{k\Delta x}$. This gives a periodic function $\frac{\Delta x}{c}\mathrm{Im}(s)$ with period π. This can be seen by using the definition of wavenumber $k = \frac{2\pi}{\lambda}$ where λ is a wavelength. By writing the wavelength as a factor ξ times Δx, $\lambda = \xi\Delta x$, we can write

$$\xi = \frac{2\pi}{\theta} \qquad \text{where} \qquad 0 \leq \theta \leq \pi \tag{11.29}$$

The ξ represents the number of grid points per wavelength that correspond to a certain $k\Delta x$. For example, a value of $k\Delta x = \theta = \pi$ corresponds to a spatial resolution of 2 points per wavelength, $k\Delta x = \theta = \pi/2$ corresponds to a spatial resolution of 4 points per wavelength and so on. The exact solution is linear in k (see equation 11.16) and is shown as the dashed line in figure 11.2. The phase velocity of the 4:th order semi-discretization is shown as the solid line in figure 11.2. For low values of $k\Delta x$ corresponding to a high resolution (many points per wavelength) the approximation follows the analytical solution but at $k\Delta x \approx \pi/4$ the phase velocity of the semi-discretized solution starts to deviate from the analytical. To achieve a good numerical solution in this case the required resolution according to this semi-discrete analysis should be at least 8 points per wavelength ($k\Delta x \leq \pi/4$).

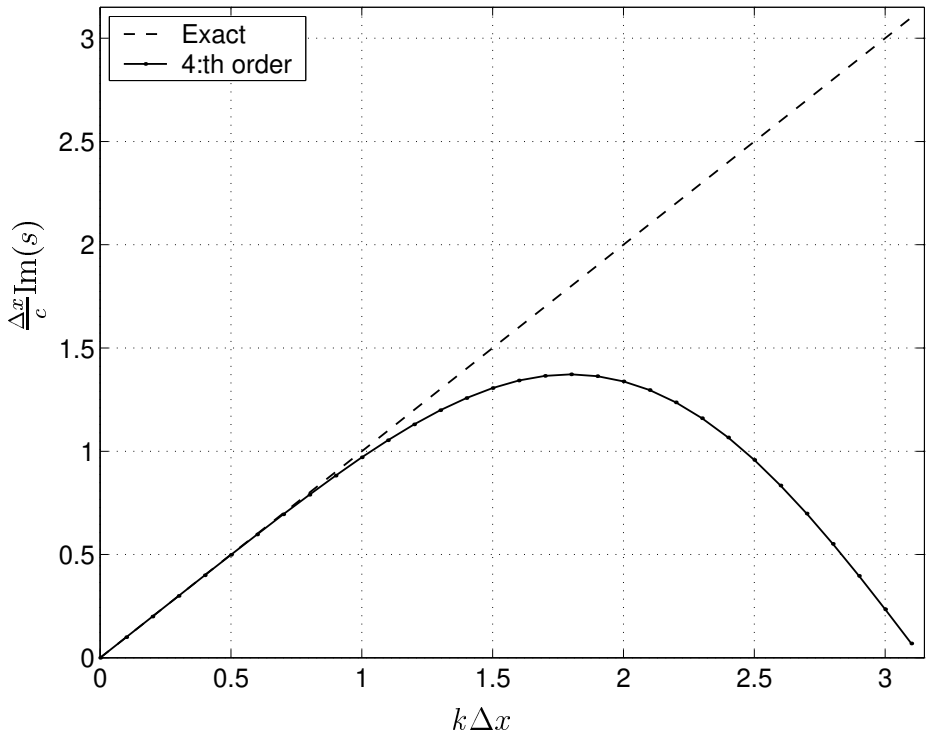

Figure 11.2: Dispersion relation for semi-discretization, 4:th order scheme

11.2.2 Artificial Numerical Dissipation

High even-order central numerical approximations to first-order derivatives have no inherent numerical dissipation. This is the reason why they are used in numerical solvers instead of odd-order approximations. But to ensure that numerical stability is retained, some kind of numerical dissipation has to be added to the solution. This is done by to the model equation (equation11.13) adding an even-order derivative times a small coefficient ε. The model equation becomes

$$\frac{\partial u}{\partial t} + c\frac{\partial u}{\partial x} = (-1)^{n+1}\varepsilon\frac{\partial^{2n} u}{\partial x^{2n}} \tag{11.30}$$

where the sign of the term is given by $(-1)^{n+1}$. To be dissipative, a second-order derivative, $n = 1$, is added with a positive sign and a fourth-order derivative $n = 2$ is added with a negative sign, and so on. The semi-discretized model equation is then written as

$$\frac{\partial u_j}{\partial t} + \frac{1}{\Delta x}\left(\sum_{l=-N}^{M} a_l u_{j+l} + \varepsilon \sum_{l=-N}^{M} d_l u_{j+l}\right) = 0 \tag{11.31}$$

The coefficients d_l in equation 11.31 determine the order of the approximated term. The coefficients for a central difference approximation of a sixth-order derivative are given in Section 11.4. The amount of dissipation added is controlled by the factor ε. The expression for s in this case becomes

$$s = \frac{c}{\Delta x}\left[2i\sum_{l=1}^{M} a_l \sin(k\Delta x l) - \varepsilon\left(d_0 + 2\sum_{l=1}^{M} d_l \cos(k\Delta x l)\right)\right] \tag{11.32}$$

and

$$z(k,t) = \exp(st) = \exp\left(\frac{ct}{\Delta x}\left[2i\sum_{l=1}^{M} a_l \sin(k\Delta x l) - \varepsilon\left(d_0 + 2\sum_{l=1}^{M} d_l \cos(k\Delta x l)\right)\right]\right) \tag{11.33}$$

When adding a dissipative term in this way, the exponent in the expression for z is no longer purely imaginary but also includes a real part. The effect of this can be seen if we rewrite equation 11.33 as

$$z(k,t) = \exp\left(\frac{2ict}{\Delta x}\sum_{l=1}^{M} a_l \sin(k\Delta x l)\right)\exp\left(-\frac{c\varepsilon t}{\Delta x}\left(d_0 + 2\sum_{l=1}^{M} d_l \cos(k\Delta x l)\right)\right) \tag{11.34}$$

If the exponent in the real part of equation 11.34 is positive for a certain k then the corresponding wave will be amplified in time and if the exponent is negative for a certain k the corresponding wave will decrease in time. Observe that including dissipation with this technique does not affect the dispersion, only the dissipation. As an example the dispersion relation and dissipation relation of the standard 4:th order scheme and the "Dispersion Relation Preserving" scheme (DRP) by Tam [15] are shown in figure 11.3. A 4:th order derivative is used to add dissipation to the 4:th order scheme and a 6:th order derivative for

the DRP. Figure 11.3(a) shows a clear difference between the standard 4:th order scheme and the DRP. The DRP scheme shows a negligible error in the dispersion relation up to $k\Delta x \approx \pi/2$ while the standard scheme gives the same amount of error at $k\Delta x \approx \pi/4$. Figure 11.3(b) shows the real part of s as a function of $k\Delta x$. Negative values of $\mathrm{Re}(s)$ for a certain $k\Delta x$ correspond to dissipation of waves with wavenumber k. The ideal form of the curves in figure 11.3(b) would be a zero value for all wavenumber $k\Delta x$ up to $k\Delta x \approx \pi$ and then a very large negative value of $\mathrm{Re}(s)$ at $k\Delta x \approx \pi$. With this in mind one can see that the sixth-order derivative added in the DRP scheme gives slightly better distribution of the dissipation over different wavenumber k than the fourth-order derivative added in the 4:th order scheme.

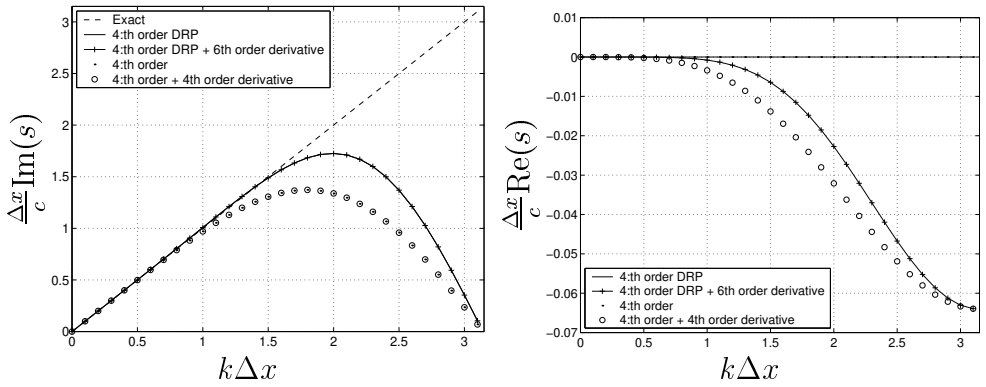

(a) Dispersion relation

(b) Dissipation relation

Figure 11.3: Dispersion relation and dissipation relation for semi-discretization

11.2.3 Full Discretization

When stability analysis is based on the semi-discretized equations the time variable is assumed to be continuous and the time derivative is assumed to be evaluated exactly. In a numerical solver, however, the time marching is not exact. When using a Runge-Kutta time marching technique the time dependent part of equation 11.21 is approximated by a Taylor expansion of $z = \exp(st)$. Begin by rewriting the model equation, equation 11.18 on the form

$$\frac{\partial u_j}{\partial t} = Au_j \tag{11.35}$$

where Au_j is an approximation of the spatial derivative $-c\frac{\partial u}{\partial x}$ at location j. For a linear operator A, a four stage 4:th order Runge-Kutta applied on the model equation can be written as

$$\begin{aligned} u_j^* &= u_j^n + \frac{1}{4}\Delta t A u_j^n \\ u_j^{**} &= u_j^n + \frac{1}{3}\Delta t A u_j^* \\ u_j^{***} &= u_j^n + \frac{1}{2}\Delta t A u_j^{**} \\ u_j^{n+1} &= u_j^n + \Delta t A u_j^{***} \end{aligned} \tag{11.36}$$

where u_j^n is the solution at time step n and u_j^{n+1} is the solution at time step $n+1$ and j is the the current space location. This gives a 4:th order time stepping in terms of the Taylor expansion

$$u_j^{n+1} = [1 + At + \frac{1}{2}A^2t^2 + \frac{1}{6}A^3t^3 + \frac{1}{24}A^4t^4]u_j^n + \mathrm{HOT} \tag{11.37}$$

or equivalently

$$z = \exp(st) \approx 1 + st + \frac{1}{2}s^2t^2 + \frac{1}{6}s^3t^3 + \frac{1}{24}s^4t^4 + \mathrm{HOT} \tag{11.38}$$

By inserting the resulting expression for s from the semi-discrete analysis into equation 11.38 an expression is given for how the solution develops in time when the time marching is done through a 4:th order time marching technique. Two quantities will now be defined. The amplitude error and the relative phase velocity. The amplitude error of the approximation of z is defined by

$$\varepsilon_A = \frac{|z| - 1}{\Delta t} \tag{11.39}$$

and the relative phase velocity is defined by

$$\frac{c*}{c} = \frac{-\angle z}{kc\Delta t} \tag{11.40}$$

where $\angle z$ is the phase of z and $|z|$ is the amplitude. Although not obvious here, c^* is now not only a function of $k\Delta x$, but also of the CFL number and hence has a dependence on Δt. This was not the case in the semi-discrete analysis and this is the main difference between the semi-discrete and the fully discrete analysis. The amplitude error and relative phase velocity for a 4:th order space discretization and the 4:th order DRP scheme combined with a 4:th order Runge-Kutta are shown in figure 11.4. The amount of dissipation added is the same as in the semi-discrete case above.

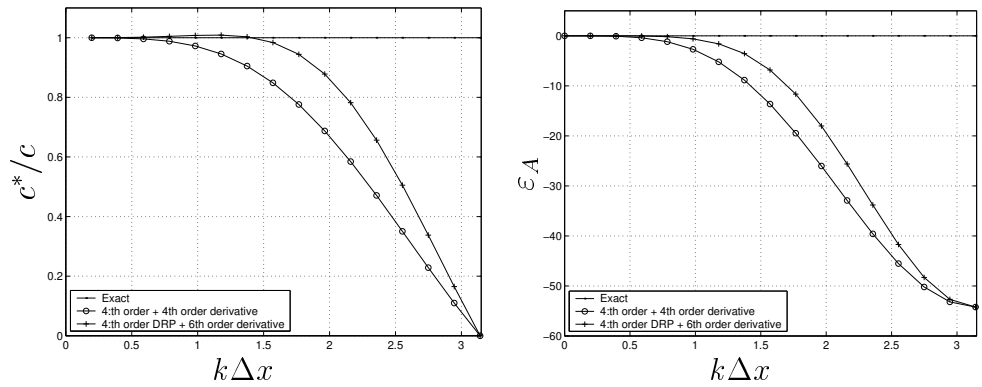

(a) Relative phase velocity

(b) Amplitude error

Figure 11.4: Relative phase velocity and amplitude error for full discretizations

The dependence of the amplitude error and the relative phase velocity on CFL-number is shown in figure 11.5. As can be seen in figures 11.5(a) and 11.5(b) the difference is small for all CFL-numbers in terms of relative phase velocity and also for CFL-number up to 0.5 in terms of amplitude error. For $\mathrm{CFL} = 0.6$ there is a clear increase in amplitude error. Based on this the conclusion is that the solution is more or less independent of CFL-number up to approximately $\mathrm{CFL} = 0.5$ with an increase of numerical dissipation for higher values of the CFL-number.

11.2.4 Introducing Source Terms

Introducing source terms into the fully discretized equation 11.35 gives an equation as

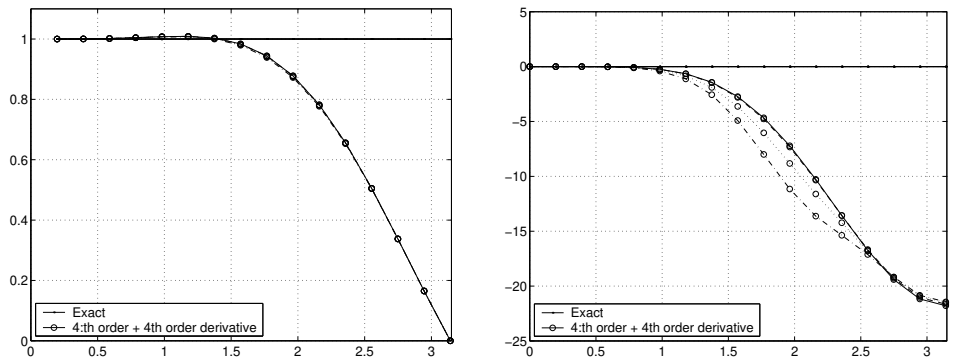

(a) Relative phase velocity (b) Amplitude error

Figure 11.5: Relative phase velocity and amplitude error for full discretizations, for CFL= solid: 0.1, dashed: 0.3, dotted: 0.5, dash-dotted: 0.6

$$\frac{\partial u_j}{\partial t} = Au_j + \sigma \tag{11.41}$$

where σ is an arbitrary source. A four stage 4:th order Runge-Kutta applied to this equation will be on the form

$$\begin{aligned} u_j^* &= u_j^n + \frac{1}{4}\Delta t A u_j^n + \Delta t f_1(\sigma) \\ u_j^{**} &= u_j^n + \frac{1}{3}\Delta t A u_j^* + \Delta t f_2(\sigma) \\ u_j^{***} &= u_j^n + \frac{1}{2}\Delta t A u_j^{**} + \Delta t f_3(\sigma) \\ u_j^{n+1} &= u_j^n + \Delta t A u_j^{***} + \Delta t f_4(\sigma) \end{aligned} \tag{11.42}$$

where $f(\sigma)$ is some linear combination of σ evaluated at different times. Expanding the expression 11.42 and identifying the linear combinations to restore a 4:th order time marching scheme gives

$$
\begin{aligned}
u_j^{n+1} = & \left[1 + At + \frac{1}{2}A^2t^2 + \frac{1}{6}A^3t^3 + \frac{1}{24}A^4t^4\right] u_j^n \\
& + \left[\frac{1}{6}\Delta t + \frac{1}{6}A(\Delta t)^2 + \frac{1}{12}A^2(\Delta t)^3 + \frac{1}{24}A^3(\Delta t)^4\right] \sigma^n \\
& + \left[\frac{2}{3}\Delta t + \frac{1}{3}A(\Delta t)^2 + \frac{1}{12}A^2(\Delta t)^3\right] \sigma^{n+\frac{1}{2}} \\
& + \frac{1}{6}\Delta t \sigma^{n+1} + \mathrm{HOT}
\end{aligned}
\tag{11.43}
$$

or in terms of Runge-Kutta time marching

$$
\begin{aligned}
u_j^* &= u_j^n + \frac{1}{4}\Delta t A u_j^n + \frac{1}{4}\Delta t \sigma^n \\
u_j^{**} &= u_j^n + \frac{1}{3}\Delta t A u_j^* + \frac{1}{3}\Delta t \left(\frac{1}{2}\sigma^n + \frac{1}{2}\sigma^{n+\frac{1}{2}}\right) \\
u_j^{***} &= u_j^n + \frac{1}{2}\Delta t A u_j^{**} + \frac{1}{2}\Delta t \left(\frac{1}{3}\sigma^n + \frac{2}{3}\sigma^{n+\frac{1}{2}}\right) \\
u_j^{n+1} &= u_j^n + \Delta t A u_j^{***} + \frac{1}{6}\Delta t \left(\sigma^n + 4\sigma^{n+\frac{1}{2}} + \sigma^{n+1}\right)
\end{aligned}
\tag{11.44}
$$

By evaluating the source terms in the manner as in expression 11.44 the numerical accuracy of the time marching technique is restored to 4:th order. σ, $\sigma^{n+\frac{1}{2}}$ and σ^{n+1} is the source evaluated at times n, $n+\frac{1}{2}$ and $n+1$, respectively.

11.3 Transformation of Solution to Characteristic Variables

For a locally homogeneous flow the linearized Euler equations can be written on the following quasi-linear form

$$\frac{\partial Q'}{\partial t} + \left(\frac{\partial E}{\partial Q}\right)_0 \frac{\partial Q'}{\partial x} + \left(\frac{\partial F}{\partial Q}\right)_0 \frac{\partial Q'}{\partial y} + \left(\frac{\partial G}{\partial Q}\right)_0 \frac{\partial Q'}{\partial z} = 0 \tag{11.45}$$

where the derivatives of E, F and G with respect to Q are the flux Jacobian matrices evaluated at the reference solution Q_0. Consider a linear combination of the flux Jacobians in some direction $\mathbf{n} = (\alpha, \beta, \gamma)$.

$$\tilde{A}_0 = \alpha \left(\frac{\partial E}{\partial Q}\right)_0 + \beta \left(\frac{\partial F}{\partial Q}\right)_0 + \gamma \left(\frac{\partial G}{\partial Q}\right)_0 \tag{11.46}$$

Assuming that fluctuations are planar waves aligned with the vector $\mathbf{n}$ they are governed by a one dimensional equation in the $\mathbf{n}$-direction.

$$\frac{\partial Q'}{\partial t} + \tilde{A}_0 \frac{\partial Q'}{\partial \xi} = 0 \tag{11.47}$$

where $\tilde{A}_0$ is defined as above and ξ is the the spatial variable in the $\mathbf{n}$-direction. Equations 11.47 consists of five coupled equations. These cannot be solved independently without decoupling. This is done by introducing characteristic variables, W. Let

$$Q' = TW \qquad \text{where} \qquad W = \begin{bmatrix} W^{(1)} \\ W^{(2)} \\ W^{(3)} \\ W^{(4)} \\ W^{(5)} \end{bmatrix} \tag{11.48}$$

where T and T^{-1} are chosen to diagonalize $\tilde{A}_0$ according to

$$T^{-1}\tilde{A}_0 T = \Lambda = \text{diag}\left[\lambda^1, \lambda^2, \lambda^3, \lambda^4, \lambda^5\right] \tag{11.49}$$

Inserting the above relation into equation 11.47 gives

$$\frac{\partial W}{\partial t} + \Lambda \frac{\partial W}{\partial \xi} = 0 \tag{11.50}$$

Equations 11.50 are now decoupled and govern propagation of waves in the ξ-direction. The columns of the matrix T are the eigenvectors to the matrix $\tilde{A}$ and λ^i are the corresponding eigenvalues. The eigenvalues are also called characteristic speeds. The characteristic speeds can be computed analytically and are given by

$$\begin{aligned} \lambda^1 = \lambda^2 = \lambda^3 &= \alpha\overline{u} + \beta\overline{v} + \gamma\overline{w} \\ \lambda^4 &= \alpha\overline{u} + \beta\overline{v} + \gamma\overline{w} + c\sqrt{\alpha^2 + \beta^2 + \gamma^2} \\ \lambda^5 &= \alpha\overline{u} + \beta\overline{v} + \gamma\overline{w} - c\sqrt{\alpha^2 + \beta^2 + \gamma^2} \end{aligned} \tag{11.51}$$

where $(\overline{u}, \overline{v}, \overline{w})$ is the local reference velocity vector. The sign of the characteristic speeds λ^i gives information about the direction the characteristic variable $W^{(i)}$ is traveling. A characteristic variable $W^{(i)}$ with characteristic speed $\lambda^i > 0$ is traveling in positive $\mathbf{n}$-direction and vice versa.

The physical interpretation of the characteristic variables is

$$\begin{aligned} W^{(1)} &= \text{entropy wave} \\ W^{(2)}, W^{(3)} &= \text{vorticity waves} \\ W^{(4)}, W^{(5)} &= \text{acoustic waves} \end{aligned} \tag{11.52}$$

The solution can be transformed back to physical variables Q' using equation 11.48.

11.4 Numerical Coefficients for FVM vs FDM

A centered finite difference approximation of a volume-averaged first-order derivative can be written as

$$\left.\frac{\partial \overline{\phi}}{\partial x}\right|_i = \frac{1}{\Delta x} \sum_{l=-N}^{N} c_l \overline{\phi}_{i+l} \tag{11.53}$$

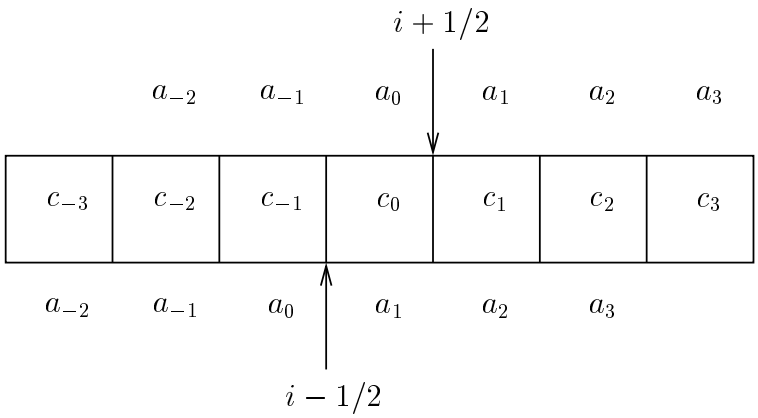

Figure 11.6: Definitions of coefficients.

where the coefficients are defined as in figure 11.6. The finite volume approximation of the same volume-averaged first-order derivative is

$$\left.\frac{\partial\overline{\phi}}{\partial x}\right|_i = \frac{1}{\Delta x}\int_{x_{i-1/2}}^{x_{i+1/2}} \frac{\partial\phi}{\partial x}\mathrm{dx} = \frac{1}{\Delta x}\left(\phi_{i+1/2} - \phi_{i-1/2}\right) \tag{11.54}$$

$\phi_{i+1/2}$ and $\phi_{i-1/2}$ are point values (or face averaged) of ϕ and the known degrees of freedom are the volume-averaged $\overline{\phi}$ in the cells. The estimation of a face value must be given by the volume-averages and is given by

$$\phi_{i+1/2} = \sum_{l=-(N-1)}^{N} a_l \frac{1}{\Delta x}\int_{x_{i+l-1/2}}^{x_{i+l+1/2}} \phi\mathrm{dx} = \sum_{l=-(N-1)}^{N} a_l\overline{\phi}_{i+l} \tag{11.55}$$

Inserting equation 11.55 into equation 11.54 gives

$$\begin{aligned}\left.\frac{\partial\overline{\phi}}{\partial x}\right|_i &= \frac{1}{\Delta\mathrm{x}}\left(\sum_{l=-(N-1)}^{N} a_l\overline{\phi}_{i+l} - \sum_{l=-(N-1)}^{N} a_l\overline{\phi}_{i+l-1}\right) = \\ &\frac{1}{\Delta\mathrm{x}}\left(a_N\overline{\phi}_{i+N} + \sum_{l=-(N-1)}^{N-1}(a_l - a_{l+1})\overline{\phi}_{i+l} - a_{-(N-1)}\overline{\phi}_{i-N+2}\right)\end{aligned} \tag{11.56}$$

By comparing equations 11.53 and 11.56 the following relation can be found between the finite difference and finite volume coefficients.

$$
\begin{aligned}
c_{-N} &= -a_{-(N-1)} \\
c_l &= a_l - a_{l+1} \qquad -(N-1) \leq l \leq (N-1) \\
c_N &= a_N
\end{aligned}
\tag{11.57}
$$

Using the relations 11.57 the coefficients of a centered finite volume approximation can be transformed to coefficients of the corresponding finite difference approximation.

The coefficients for a standard 4:th order approximation of a first-order derivative are

$$
\begin{aligned}
c_2 = -c_{-2} &= -\tfrac{1}{12} & \qquad a_2 = a_{-1} &= -\tfrac{1}{12} \\
c_1 = -c_{-1} &= \tfrac{8}{12} & a_1 = a_0 &= \tfrac{7}{12} \\
c_0 &= 0
\end{aligned}
$$

The coefficients for a 4:th order DRP scheme [15] are

$$
\begin{aligned}
c_3 = -c_{-3} &= 0.02651995 & \qquad a_3 = a_{-2} &= 0.02651995 \\
c_2 = -c_{-2} &= -0.18941314 & a_2 = a_{-1} &= -0.16289319 \\
c_1 = -c_{-1} &= 0.79926643 & a_1 = a_0 &= 0.63637324 \\
c_0 &= 0
\end{aligned}
$$

The coefficients below relate to the addition of artificial numerical dissipation by the addition of a dissipative, see Section 11.2.2. The coefficients for a central difference approximation of a 4:th order derivative are

$$
\begin{aligned}
d_2 = d_{-2} &= 1 \\
d_1 = d_{-1} &= -4 \\
d_0 &= 6
\end{aligned}
$$

The coefficients for a central difference approximation of a 6:th order derivative are

$$
\begin{aligned}
d_3 = d_{-3} &= -1 \\
d_2 = d_{-2} &= 6 \\
d_1 = d_{-1} &= -15 \\
d_0 &= 20
\end{aligned}
$$

11.5 Definitions of Correlations

For isotropic homogeneous turbulence the longitudinal and transverse correlation coefficients $f(r)$ and $g(r)$ are defined by

$$\begin{aligned} f(r) &= \frac{\overline{u_r(\mathbf{x})u_r(\mathbf{y})}}{u'^2} \\ g(r) &= \frac{\overline{u_n(\mathbf{x})u_n(\mathbf{y})}}{u'^2} \end{aligned} \tag{11.58}$$

where u_r is the velocity component aligned with the vector $\mathbf{r} = \mathbf{y} - \mathbf{x}$, u_n is normal to $\mathbf{r}$ and u' is the RMS of the velocity.

If the three-dimensional energy spectrum of isotropic homogeneous turbulence is known then the correlation functions are given by [13]

$$\begin{aligned} f(r) &= \frac{2}{u'^2}\int_0^\infty E(k)\left(\frac{\sin kr}{k^3r^3} - \frac{\cos kr}{k^2r^2}\right)\mathrm{d}k \\ g(r) &= \frac{1}{u'^2}\int_0^\infty E(k)\left(\frac{\sin kr}{kr} - \frac{\sin kr}{k^3r^3} + \frac{\cos kr}{k^2r^2}\right)\mathrm{d}k \end{aligned} \tag{11.59}$$

11.6 Time Filtering

To generate a random signal with a specified autocorrelation one starts with white noise. The white noise signal x^n should have the following characteristics.

$$\begin{aligned} \overline{x^n} &= \lim_{N\to\infty}\frac{1}{N}\sum_{n=1}^{N} x^n = 0 \\ &\lim_{N\to\infty}\frac{1}{N}\sum_{n=1}^{N} x^{n^2} = \text{variance of sequence} \\ \overline{x^n x^{n-p}} &= \lim_{N\to\infty}\frac{1}{N}\sum_{n=1}^{N} x^n x^{n-p} = 0 \quad \text{for all} \quad p \geq 1 \end{aligned} \tag{11.60}$$

where the superscript $(\cdot)^n$ denotes the n:th sample.

A first-order asymmetric filter is defined by the formula

$$y^n = ay^{n-1} + bx^n \tag{11.61}$$

where a and b are real constants that can be related to a time scale and relation of the RMS of the input signal x^n and the output signal y^n. The average of y^n is

$$\overline{y^n} = a\overline{y^{n-1}} + b\overline{x^n} \tag{11.62}$$

Since $\overline{x^n} = 0$ this gives that if $a \neq 1$ then $\overline{y^n} = 0$. Further more we have that

$$\overline{y^n y^n} = a\overline{y^{n-1}y^{n-1}} + b\overline{x^n x^n} + ab\overline{y^{n-1}x^n} \tag{11.63}$$

So that since y^{n-1} and x^n are totally uncorrelated ($\overline{y^{n-1}x^n} = 0$) and also $\overline{y^{n-1}y^{n-1}} = \overline{y^n y^n}$ the mean square of y^n can be computed as

$$\overline{y^n y^n} = \frac{b^2}{1-a^2}\overline{x^n x^n} \tag{11.64}$$

The autocorrelation of y^n is defined through

$$\begin{array}{lll} \overline{y^n y^{n-1}} & = a\overline{y^{n-1}y^{n-1}} + b\overline{x^n y^{n-1}} & = a\overline{y^n y^n} \\ \overline{y^n y^{n-2}} & = a\overline{y^{n-1}y^{n-2}} + b\overline{x^n y^{n-2}} & = a^2\overline{y^n y^n} \\ \vdots & \vdots & \vdots \\ \overline{y^n y^{n-p}} & = a\overline{y^{n-1}y^{n-p}} + b\overline{x^n y^{n-p}} & = a^p\overline{y^n y^n} \end{array} \tag{11.65}$$

The autocorrelation function thus becomes

$$\varrho_p = \frac{\overline{y^n y^{n-p}}}{\overline{y^n y^n}} = a^p \tag{11.66}$$

Since the index n refers to the time levels t^n of a time series, with constant time intervals Δt, we obtain the following relationship between the constant a and the time scale defined as the time separation τ for which the autocorrelation function is reduced to $\exp(-1)$

$$\tau = -\frac{\Delta t}{\ln(a)} \quad \text{or} \quad a = \exp\left(-\frac{\Delta t}{\tau}\right) \tag{11.67}$$

It is thus possible to generate a new random sequence y^n with a specified RMS and time scale by using a white noise sequence x^n and a first-order asymmetric filter.

Bibliography

[1] M.J. Lighthill. On sound generated aerodynamically, i. general theory. *Proc. Roy. Soc.*, A 211:564–587, 1952.

[2] M.J. Lighthill. On sound generated aerodynamically, ii. turbulence as a source of sound. *Proc. Roy. Soc.*, A 222:1–32, 1954.

[3] J. Curle. The influence of solid boundaries upon aerodynamic sound. *Proc. Roy. Soc.*, A 231:505–514, 1955.

[4] J.E. Ffowcs Williams and D.L. Hawkins. Sound generation by turbulence and surfaces in arbitrary motion. *Philos. Trans. Roy. Soc.*, A 264, No. 1151:321–342, 1969.

[5] J.E. Ffowcs Williams. The noise from turbulence convected at high speed. *Philos. Trans. Roy. Soc.*, A 255 No. 1061:496–503, 1963.

[6] G.M. Lilley. On the noise from jets. *AGARD CP-131*, 1974.

[7] S.C. Crow and F.H. Champagne. Sound generation in a mixing layer. *Journal of Fluid Mechanics*, 48:547 – 591, 1971.

[8] C.K.W Tam. Supersonic jet noise. *Annu. Rew. Fluid Mech.*, 27:17–43, 1995.

[9] W. Bechara, C. Bailly, and P. Lafon. Stochastic approach to noise modeling for free turbulent flows. *AIAA Journal*, 32 , No. 3:455–463, 1994.

[10] C. Bailly and D. Juvé. A stochastic approach to compute subsonic noise using linearized euler's equations. *AIAA Journal*, 99-1872, 1999.

[11] R.H. Kraichnan. Diffusion by a random velocity field. *J. Comp. Physics*, 13(1):22–31, 1970.

[12] M. Karweit, P. Blanc-Benon, D. Juvé, and G. Comte-Bellot. Simulation of the propagation of an acoustic wave through a turbulent velocity field: A study of phase variance. *J. Acoust. Soc. Am.*, 89(1):52–62, 1991.

[13] J.O. Hinze. *Turbulence, Second edition*. McGraw Hill, 1975.

[14] L.-E. Eriksson. Development and validation of highly modular flow solver versions in g2dflow and g3dflow. Internal report 9970-1162, Volvo Aero Corporation, Sweden, 1995.

[15] C.K.W Tam and J.C. Webb. Dispersion-relation-preserving finite difference schemes for computational acoustics. *J. Comp. Physics*, 107:262–281, 1993.

[16] L.-E. Eriksson. *Transfinite Mesh Generation and Computer-Aided Analysis of Mesh Effects*. PhD thesis, Department of Computer Sciences, Uppsala University, Sweden, 1984.

[17] K.W. Thompson. Time dependent boundary conditions for hyperbolic systems. *J. Comp. Physics*, 68:1–24, 1987.

[18] K.W. Thompson. Time dependent boundary conditions for hyperbolic systems, *ii*. *J. Comp. Physics*, 89:439–461, 1990.

[19] T.J. Poinsot and S.K. Lele. Boundary conditions for direct simulations of compressible viscous flows. *J. Comp. Physics*, 101:104–129, 1992.

[20] A. Bayliss and E. Turkel. Far-field boundary conditions for compressible flows. *J. Comp. Physics*, 48:182–199, 1982.

[21] C.K.W Tam and Z. Dong. Radiation and outflow boundary conditions for direct computation of acoustic and flow disturbances in a nonuniform mean flow. *J. Comput. Acoust*, 4:175–201, 1996.

[22] C. Bogey and C. Bailly. Three-dimensional non-reflective boundary conditions for acoustic simulations: far field formulation and validation test cases. *Accepted in Acta Acoustica*, xx:xx – xx, 2002.

[23] R. Hixon, S.-H. Shih, and R.R. Mankbadi. Evaluation of boundary conditions for computational aeroacoustics. *AIAA Journal*, 33 No. 11, 1995.

[24] L.-E. Eriksson.

[25] T. Colonius, S.K. Lele, and P. Moin. Boundary conditions for direct computation of aerodynamic sound generation. *AIAA Journal*, 31 No. 9:1574 – 1582, 1993.

[26] R. Hixon, S.-H. Shih, and R.R. Mankbadi. Evaluation of boundary conditions for the gust-cascade problem. *J. Propulsion and Power*, 16 No. 1, 2000.

[27] A. S. Lyrintzis. Review: The use of kirchhoff's method in computational aeroacoustics. *ASME: Journal of Fluids Engineering*, 116:665 – 676, 1994.

[28] J. B. Freund, S. K. Lele, and P. Moin. Calculation of the radiated sound field using an open kirchhoff surface. *AIAA Journal*, 34 No. 5:909 – 916, 1996.

[29] A.D. Pierce. *Acoustics. An Introduction to Its Physical Principles and Applications*. Acoustical Society of America, Woodbury, New York, 1991.

[30] M. Billson. Jet noise prediction based on large eddy simulation. Thesis for the degree Master of Science, 1999.

[31] C.K.W. Tam and J.C. Hardin, editors. *Second Computational Aeroacoustic (CAA) Workshop on Benchmark Problems*, Tallahasse. Florida, 1996. NASA Conference Publication 3352.

[32] M.E. Hayder, F.Q. Hu, and M.Y. Hussaini. Toward perfectly absorbing boundary conditions for euler equations. *AIAA Journal*, 37 , No. 8:912–918, 1999.

[33] F.Q. Hu. On absorbing boundary conditions for linearized euler equations by a perfectly matched layer. *J. Comp. Physics*, 129:201–219, 1996.

[34] T. Colonius, S.K. Lele, and P. Moin. Sound generation in a mixing layer. *Journal of Fluid Mechanics*, 330:375 – 409, 1997.

[35] C. Bogey, C. Bailly, and D. Juvé. Numerical simulation of sound generated by vortex pairing in a mixing layer. *AIAA Journal*, 38 No. 12, 2000.

[36] B. Engquist and A. Majda. Absorbing boundary conditions for the numerical simulation of waves. *Mathematics of Computation*, 31:629–651, 1977.

[37] B. Engquist and A. Majda. Radiation boundary conditions for acoustic and elastic wave calculations. *Communications on Pure and Applied Mathematics*, 32:313–357, 1979.

[38] A. Michalke. On the inviscid instability of the hyperbolic-tangent velocity profile. *Journal of Fluid Mechanics*, vol 19, 1964.

[39] J.L. Stromberg, D.K. McLaughlin, and T.R Troutt. Flow field and acoustic properties of a mach number 0.9 jet at a low reynolds number. *J. Sound Vib.*, 72 No. 2:159–176, 1980.

[40] J. B. Freund. Noise sources in a low-reynolds-number turrbulent jet at mach 0.9. *Journal of Fluid Mechanics*, 438:277 – 305, 2001.

[41] J. B. Freund. Acoustic sources in a turbulent jet: A direct numerical simulation study. *AIAA Journal*, xxx:xxx – xxx, 1999.